



AUBURN UNIVERSITY ENGINEERING EXPERIMENT STATION

FINAL REPORT
NSG-3233

DEVELOPMENT OF BASIC THEORIES AND
TECHNIQUES FOR DETERMINING STRESSES
IN ROTATING TURBIN OR COMPRESSOR BLADES

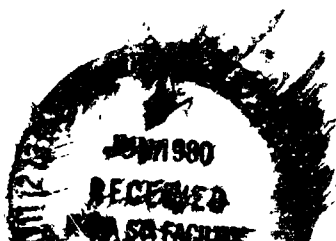
by

C. H. Chien
W. F. Swinson
J. L. Turner
F. A. Moslehy
W. F. Ranson

Technical Report to

NASA
Lewis Research Center
Cleveland, Ohio

May 1980



(NASA-CR-163190) DEVELOPMENT OF BASIC
THEORIES AND TECHNIQUES FOR DETERMINING
STRESSES IN ROTATING TURBINE OR COMPRESSOR
BLADES Final Report (Alabama Univ.,
University.) 158 p HC A08/MP A01 CSCL 21E 33/07 21030

N30-24317

Unclass
21030

FINAL REPORT
NSG-3233

DEVELOPMENT OF BASIC THEORIES AND
TECHNIQUES FOR DETERMINING STRESSES
IN ROTATING TURBIN OR COMPRESSOR BLADES

by

C. H. Chien
W. F. Swinson
J. L. Turner
F. A. Moslehy
W. F. Ranson

Technical Report to

NASA
Lewis Research Center
Cleveland, Ohio

Auburn University
Engineering Experiment Station
Auburn University, Alabama 36849

May 1980

FINAL REPORT
(PART I)

A TECHNIQUE TO DETERMINE THE STRESS
DISTRIBUTION IN ROTATING ELEMENTS

by

C. H. Chien
W. F. Swinson
J. L. Turner

Submitted to

NASA
Lewis Research Center
Cleveland, Ohio

through

Engineering Experiment Station
Auburn University, Alabama 36849

May 1980

A TECHNIQUE TO DETERMINE THE STRESS DISTRIBUTION IN ROTATING ELEMENTS

ABSTRACT

A method for measuring in-plane displacement of a rotating structure by using two laser speckle photographs is described. From the displacement measurements one can calculate strains and stresses due to a centrifugal load.

This technique involves making separate speckle photographs of a test model. One photograph is made with the model loaded (model is rotating); the second photograph is made with no load on the model (model is stationary). A sandwich is constructed from the two speckle photographs and data are recovered in a manner similar to that used with conventional speckle photography. The basic theory, experimental procedures of this method and data analysis of a simple rotating specimen are described in the text.

PRECEDING PAGE BLANK NOT FILMED

TABLE OF CONTENTS

| | |
|---|------|
| LIST OF TABLES. | viii |
| LIST OF FIGURES. | ix |
| I. INTRODUCTION | 1 |
| II. BASIC THEORY AND MATHEMATICAL MODEL OF SANDWICH SPECKELGRAM. | 4 |
| III. EXPERIMENTAL SETUP AND PROCEDURE. | 16 |
| IV. EXPERIMENTAL RESULTS. | 36 |
| V. CONCLUSION. | 41 |
| REFERENCES. | 43 |
| APPENDICES. | 44 |

PRECEDING PAGE BLANK NOT FILMED

LIST OF TABLES

1. The Theoretical and Experimental Displacement
and Strain Data. 39

PRÉCEDING PAGE BLANK NOT FILMED

LIST OF FIGURES

| | |
|---|----|
| 1. Diffraction by Two Points. | 7 |
| 2. Two Theoretical Fringe Patterns | 14 |
| 3A. Model and Motor and Supporting Frames (Front View). . | 18 |
| 3B. Model and Motor and Supporting Frames (Back View). . . | 19 |
| 4. Schematic of the Equipment Layout for Taking Dynamic Picture. | 20 |
| 5. He-Ne Laser Setup. | 22 |
| 6A. Film Holder (Front View). | 27 |
| 6B. Film Holder (Back View). | 28 |
| 7. Positioner. | 31 |
| 8. Main Frame of the Positioner. | 32 |
| 9A. Translation Stage of the Positioner (Top View). . . . | 33 |
| 9B. Translation Stage of the Positioner (Bottom View). . . | 34 |
| 10. Laser and Positioner Setup for Data Recovery. | 35 |
| 11. The Typical Fringe Patterns | 37 |

~~PRECEDING PAGE BLANK NOT FILMED~~

I. INTRODUCTION

Analysis of the stress and vibration characteristics of rotating turbine engine components under operating conditions is a continuing problem in the testing and development of today's airplane power plants. J. M. Allen and L. B. Erickson [1] have analyzed a free standing gas turbine blade by using the NASTRAN finite element code. Correct modeling of the service loads on the structure is a major difficulty in such analyses. Other investigators have used conventional strain gages to experimentally analyze such structures. Strain gage data is usually delivered through slip rings, or via radio telemetry, to recording equipment. Problems associated with getting these signals to the recorder often plague such tests [2].

J. P. Sikora and F. T. Mendenhall, Jr. observed and analyzed vibration-mode patterns of a rotating propeller by means of an axially symmetric spinning-hologram technique in 1974 [3]. K. A. Stetson also investigated the vibration problem of rotating objects by using an image derotator with a hologram interferometry technique in 1977 [2], [4]. Although holographic interferometry is well suited to measurement of normal to the surface movement, the separation of the in-plane displacements (from the out-of-plane) is more complex. Since the measurement of in-plane displacements is usually necessary for strain computation, a simple coherent method,

possessing the advantages of holographic interferometry (high sensitivity and large field converge of complex shapes) but suitable for direct in-plane displacement measurement would be desirable.

Laser speckle photography has emerged in recent years as a proficient technique for measuring small in-plane displacements [5], [6]. This article develops a so called "Sandwich Speckle Photography" technique for determining the stress of rotating elements. The approach is to take a speckle picture of the rotating element with a Q-switched, ruby laser. Next the element is stopped in approximately the same position as when the dynamic speckle picture was taken and with a new film plate a second speckle picture is taken. The photographs are then mechanically superimposed, emulsion against emulsion, and carefully aligned to produce Young's fringes. This approach supposes that the speckle surface will produce the same speckle pattern when illuminated with a pulse laser at different times except for the displaced position due to the element rotation. The incentive to develop this technique was motivated by the work of Nils Abramson, who developed a "Sandwich Holography" technique in 1974 [7]. B. E. Maddux and F. D. Adams developed a Dual-plate technique for static speckle photography in 1976 [8].

In Chapter II, the basic theory of sandwich speckle photography is introduced and a mathematical model is developed to explain the fringe pattern one observes in the diffraction halo of a sandwich

specklegram. The experimental setup and procedures are described in Chapter III. Stress analysis of a simple rotating model by using this method is presented as an example.

II. BASIC THEORY AND MATHEMATICAL MODEL OF SANDWICH SPECKLEGRAM

When an object is illuminated with a laser a speckle pattern is produced. If the speckle is photographed and then the model loaded and the resulting speckle pattern superimposed on the first photograph, the double exposed photograph contains information about the displacement of the model under load. This information can be seen by shining a laser beam through a small area of the negative and observing an interference pattern on a screen. The above statements are the description of a conventional double exposure specklegram [9]. In most of the applications of double exposure speckle photography, the specimen will undergo rigid body movement in addition to deformation between exposures. In order to cancel the effect of rigid body in-plane movement of the specimen, the film holder must be translated and/or rotated between exposures by a corresponding amount. In most instances the rigid body movement is not known in advance of the loading.

A sandwich specklegram offers the user a method of canceling rigid body movement without a prior knowledge of it. Instead of employing a double exposure technique, two separate speckle photographs are made. The film plates are then sandwiched together and data recovery is accomplished as with a conventional specklegram.

In-plane rigid body translations or rotations are canceled by moving one film plate with respect to the other.

The following procedure is employed to record a sandwich specklegram. A glass film plate (typically NAH Agfa 10E75) is sandwiched with a clear plate of glass (same size and same thickness as the film plate) placing the emulsion side towards the center of the sandwich. A speckle photograph is made of the undisplaced object with the emulsion side of the film plate faced away from the surface of the object (the film plate is on the lens side of the sandwich). Then, a second speckle photograph is made of the displaced object using a new film plate, with an identical sandwich procedure except that the sandwich is turned around so that the emulsion side of the film plate is towards the surface of the object (a clear glass plate is on the lens side of the sandwich). Both film plates are then chemically processed and thoroughly dried. A sandwich specklegram is constructed by placing the two speckle photographs emulsion to emulsion such that the images are geometrically matched. A description of the mechanical positioner to accomplish this task is provided in Chapter III.

With a conventional double exposure specklegram, in-plane displacements result in speckle pairs contained in a plane perpendicular to the optical axis of the camera. This geometry is not completely simulated by the sandwich specklegram technique. Film emulsions are not infinitely thin and glass film plates vary in thickness. As a result, each speckle of a pair will be recorded either forward or behind its partner. This is true even when the

recordings are made such that the sandwiches are put together emulsion to emulsion. Therefore, data recovery from a sandwich specklegram is complicated by the longitudinal displacement of paired speckles due to separate emulsions. A modification of the Young's equation derived for conventional double exposure specklegrams [9] is required in order to explain the fringe pattern of a sandwich specklegram and acquire displacement data.

Consider a point, P_1 , contained in an aperture and illuminated by light source S as shown in Figure 1. The light wave scattered by P_1 to a point O on a distant screen may be represented by the real part of

$$\bar{E}_1 = \bar{A} \text{Exp} [i\phi_1] \quad (1)$$

where A is the amplitude and ϕ_1 is a phase angle.

Let a coordinate system XYZ originate at this point. Consider a second nearby point P_2 located by separation vector \bar{B} and of coordinates x, y, z . In Figure 1, the optical path length of the light from S to P_1 to O is denoted by L_1 and is the distance

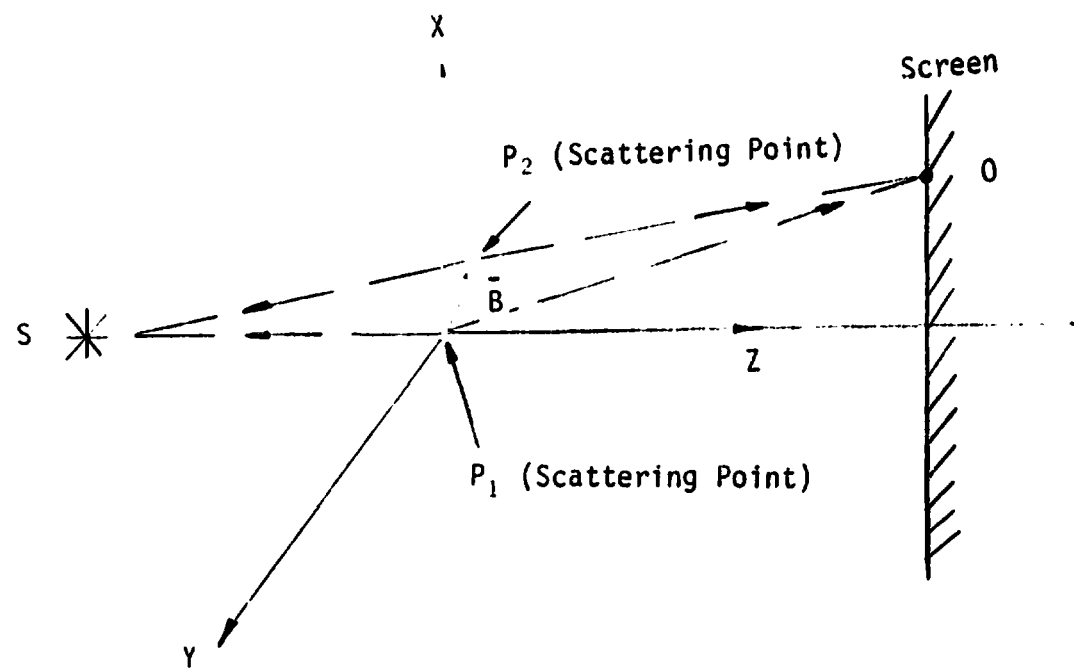
$$L_1 = |\bar{P}_1 S| + |\bar{P}_1 O| \quad (2)$$

Equation (2) can be written in the following form

$$L_1 = (\bar{P}_1 S \cdot \bar{P}_1 S)^{1/2} + (\bar{P}_1 O \cdot \bar{P}_1 O)^{1/2} \quad (3)$$

The optical path length of the light from S to P_2 to O is denoted by L_2 and is the distance

$$L_2 = |\bar{P}_2 S| + |\bar{P}_2 O| \quad (4)$$



7

Figure 1
Diffraction by Two Points

This equation can be written as

$$L_2 = (\overline{P_2S} \cdot \overline{P_2S})^{\frac{1}{2}} + (\overline{P_2O} \cdot \overline{P_2O})^{\frac{1}{2}} \quad (5)$$

The change of phase is

$$\Delta\phi = \frac{2\pi}{\lambda} (L_2 - L_1) \quad (6)$$

where λ is the wave length of the light source.

Note that

$$\overline{P_2S} = \overline{P_1S} - \overline{B} \quad (7)$$

and

$$\overline{P_2O} = \overline{P_1O} - \overline{B} \quad (8)$$

Equations (4) through (8) when combined, yield

$$\begin{aligned} \Delta\phi = \frac{2\pi}{\lambda} [& (\overline{P_2S} \cdot \overline{P_2S})^{\frac{1}{2}} + (\overline{P_2O} \cdot \overline{P_2O})^{\frac{1}{2}} - (\overline{P_1S} \cdot \overline{P_1S})^{\frac{1}{2}} \\ & - (\overline{P_1O} \cdot \overline{P_1O})^{\frac{1}{2}}] \end{aligned} \quad (9)$$

$$\begin{aligned} \Delta\phi = \frac{2\pi}{\lambda} [& (\overline{P_1S} \cdot \overline{P_1S} - 2 \overline{P_1S} \cdot \overline{B} + \overline{B} \cdot \overline{B})^{\frac{1}{2}} \\ & + (\overline{P_1O} \cdot \overline{P_1O} - 2 \overline{P_1O} \cdot \overline{B} + \overline{B} \cdot \overline{B})^{\frac{1}{2}} \\ & - (\overline{P_1S} \cdot \overline{P_1S})^{\frac{1}{2}} - (\overline{P_1O} \cdot \overline{P_1O})^{\frac{1}{2}}] \end{aligned} \quad (10)$$

Because the displacement vector \overline{B} is very small, relative to \overline{PO} and \overline{PS} the terms $\overline{B} \cdot \overline{B}$ in equation (10) are neglected as higher order terms. Then from applying the binomial expansion

$$(\overline{P_1S} \cdot \overline{P_1S} - 2 \overline{P_1S} \cdot \overline{B})^{\frac{1}{2}} = (\overline{P_1S} \cdot \overline{P_1S})^{\frac{1}{2}} - \frac{(\overline{P_1S} \cdot \overline{B})}{(\overline{P_1S} \cdot \overline{P_1S})^{\frac{1}{2}}} \quad (11)$$

$$(\overline{P_1O} \cdot \overline{P_1O} - 2 \overline{P_1O} \cdot \overline{B})^{\frac{1}{2}} \approx (\overline{P_1O} \cdot \overline{P_1O})^{\frac{1}{2}} - \frac{(\overline{P_1O} \cdot \overline{B})}{(\overline{P_1O} \cdot \overline{P_1O})^{\frac{1}{2}}} \quad (12)$$

Therefore equation (10) becomes

$$\Delta\phi = \frac{-2\pi}{\lambda} \left[\frac{\overline{P_1S}}{(\overline{P_1S} \cdot \overline{P_1S})^{\frac{1}{2}}} + \frac{\overline{P_1O}}{(\overline{P_1O} \cdot \overline{P_1O})^{\frac{1}{2}}} \right] \cdot \overline{B} \quad (13)$$

The terms in brackets in equation (13) are unit vectors in the directions $\overline{P_1S}$ and $\overline{P_1O}$; therefore, the following change in notation is employed

$$\overline{n}_s = \frac{\overline{P_1S}}{(\overline{P_1S} \cdot \overline{P_1S})^{\frac{1}{2}}} \quad (14)$$

$$\overline{n}_o = \frac{\overline{P_1O}}{(\overline{P_1O} \cdot \overline{P_1O})^{\frac{1}{2}}} \quad (15)$$

So the phase difference in optical path length traveled from S to the scattering points and then to O is given by

$$\Delta\phi = \frac{-2\pi}{\lambda} \overline{B} \cdot (\overline{n}_s + \overline{n}_o) \quad (16)$$

Let the direction cosines of \overline{n}_o be l, m, n, then

$$\overline{n}_s = -\overline{k} \quad (17)$$

$$\overline{n}_o = l\overline{i} + m\overline{j} + n\overline{k} \quad (18)$$

The light wave at O from the second point, P_2 , will then be

$$\overline{E}_2 = \overline{A} \text{Exp} [i (\phi_1 + \Delta\phi)] \quad (19)$$

Consider a small aperture centered in the X - Y plane. For each scattering point in the aperture $\overline{B} = x\overline{i} + y\overline{j}$ light reaching point

0 from each point in the aperture will be represented by

$$\bar{E} = \bar{A} \text{Exp} [i(\phi_1 + \Delta\phi_1)] \quad (20)$$

where from equation (16)

$$\Delta\phi_1 = \frac{-2\pi}{\lambda} (lx + my) \quad (21)$$

The total contribution at 0 from all points in the aperture is obtained by integrating over the aperture

$$\bar{U}_1 = \bar{A} \text{Exp} [i\phi_1] \iint_{\text{area}} \text{Exp} [i\Delta\phi_1] dx dy \quad (22)$$

Consider a second aperture identical to the first but uniformly displaced along X, Y and Z by Δx , Δy and Δz respectively. Δx , Δy and Δz are assumed sufficiently small so that equation (16) is valid.

For each scattering point in the first aperture (at coordinates x, y), there corresponds an identical point in the second aperture at coordinates $x+\Delta x, y+\Delta y$ and Δz) emitting a light wave to point 0.

Each of these waves at 0 may be represented by

$$\bar{E} = \bar{A} \text{Exp} [i(\phi_1 + \Delta\phi_2)] \quad (23)$$

where with equation (16)

$$\bar{B} = (x+\Delta x) \bar{i} + (y+\Delta y) \bar{j} + \Delta z \bar{k} \quad (24)$$

thus

$$\Delta\phi_2 = \frac{-2\pi}{\lambda} [l(x+\Delta x) + m(y+\Delta y) + (n-1)\Delta z] \quad (25)$$

The total light distribution at 0 from points in the second aperture is

$$\bar{U}_2 = \bar{A} \text{Exp} [i\phi_1] \iint_{\text{area}} \text{Exp} [i\Delta\phi_2] dx dy \quad (26)$$

Comparing \bar{U}_1 with \bar{U}_2 we find that (Note: Δx , Δy and Δz are constants)

$$\bar{U}_2 = \bar{U}_1 \text{ Exp } [-i \frac{2\pi}{\lambda} (l\Delta x + m\Delta y + (n-1)\Delta z)] \quad (27)$$

The total wave distribution at 0 from both apertures is

$$\bar{U}_T = \bar{U}_1 + \bar{U}_2 = \bar{U}_1 \left\{ 1 + \text{Exp} \left[-i \frac{2\pi}{\lambda} (l\Delta x + m\Delta y + (n-1)\Delta z) \right] \right\} \quad (28)$$

The intensity observed at point 0 is then

$$I_0 = C_1 \bar{U}_T \cdot \bar{U}_T^* \quad (29)$$

where \bar{U}_T^* is the complex conjugate of \bar{U}_T and

C_1 = a proportionality constant.

If

$$\bar{U}_T = \bar{U}_1 [1 + \text{Exp} (-i\theta)]$$

Then

$$\bar{U}_T^* = \bar{U}_1^* [1 + \text{Exp} (i\theta)]$$

$$\begin{aligned} \bar{U}_T \cdot \bar{U}_T^* &= \bar{U}_1 \cdot \bar{U}_1^* [1 + \text{Exp} (-i\theta) + \text{Exp} (i\theta) + 1] \\ &= \frac{I_1}{C_1} [2 + 2 \cos \theta] \\ &= \frac{2I_1}{C_1} [1 + \cos \theta] \end{aligned} \quad (30)$$

where

$$I_1 = C_1 \bar{U}_1 \cdot \bar{U}_1^*$$

So from equation (28), (29) and (30) we obtain

$$I_0 = I_1 [1 + \cos \frac{2\pi}{\lambda} (l\Delta x + m\Delta y + (n-1)\Delta z)] \quad (31)$$

I_1 is the intensity due to a single aperture. This intensity is modulated by the bracketed term. I_1 typically represents a halo and the bracketed term represents "Young's fringes" across the halo.

Let the X-axis be along the in-plane separation direction of the two apertures (then $\Delta y=0$). Δz represents the "gap" between film plates when using the sandwich method. Within the halo the observed intensity is then

$$I_0 \propto [1 + \cos \frac{2\pi}{\lambda} (\Delta x + (n-1)\Delta z)] \quad (32)$$

Fringes occur when

$$\Delta x + (n-1)\Delta z = \frac{N\lambda}{2} \quad N = \pm 1, 3, 5, \dots \quad (33)$$

Three conditions resulting from equation (33) are considered. First, if $\Delta z=0$ or $\Delta x \gg \Delta z$, then equation (33) reduces to

$$\Delta x = \frac{N\lambda}{2} \quad N = \pm 1, 3, 5, \dots \quad (34)$$

which represents the conventional double exposure specklegram equation. l is usually approximated as $\frac{X}{R}$ where X is the axis perpendicular to Young's fringes in the diffraction halo, R is the distance from the specklegram to the screen. Second, if $\Delta x=0$ then equation (33) becomes

$$(n-1)\Delta z = \frac{N\lambda}{2} \quad N = \pm 1, 3, 5, \dots \quad (35)$$

One can see from equation (35) that the fringe pattern of the second condition is a set of concentric circles. The spacing between these circles is inversely proportional to Δz . Third, if Δx and Δz are of nearly equal magnitude, the fringe pattern for this condition is curved. The curvature of the fringe pattern is caused by the $[(n-1)\Delta z]$ term.

Data recovery of a sandwich specklegram can be discussed. If the curvature of the fringe pattern is very small, then one can get the in-plane displacement, Δx , from equation (34). If the

curvature of the fringe pattern is large, Δx can be evaluated by the following procedure. Translate or rotate one speckle photograph with respect to the other until the fringe pattern becomes a set of concentric circles, the longitudinal displacement Δz can be acquired from equation (35). Then from equation (33) one can calculate Δx as

$$\Delta x = \frac{1}{l} \left[\frac{N\lambda}{2} - (n-1) \Delta z \right] \quad N = \pm 1, 3, 5, \dots \quad (36)$$

where

$$n = \frac{R}{\sqrt{R^2 + X^2}}$$

The direction cosine of the vector from P_1 to any observation point on the screen in the X -direction is l . The sign of l can be determined from the diffraction halo fringe pattern. If the observation points are on the upper half part of the screen, the relative values of l are positive; if the observation points are on the lower half part of the screen, the relative values of l are negative. If $\Delta z = 0$, the fringe pattern is a set of straight lines. From equation (34), one knows that for positive values of Δx , the fringe numbers of the fringes on the upper half of the screen are positive values; and the fringe numbers of the fringes on the lower half of the screen are negative values. If $\Delta x = 0$, the fringe pattern is a set of concentric circles. From equation (35), one knows that for positive value of Δz , the values of the N 's are negative; therefore, if Δx and Δz are positive values, the fringe pattern of the sum of the above two fringe patterns is similar to those illustrated in Figure 2A. Similarly, if Δx is a negative value and Δz is a positive value,

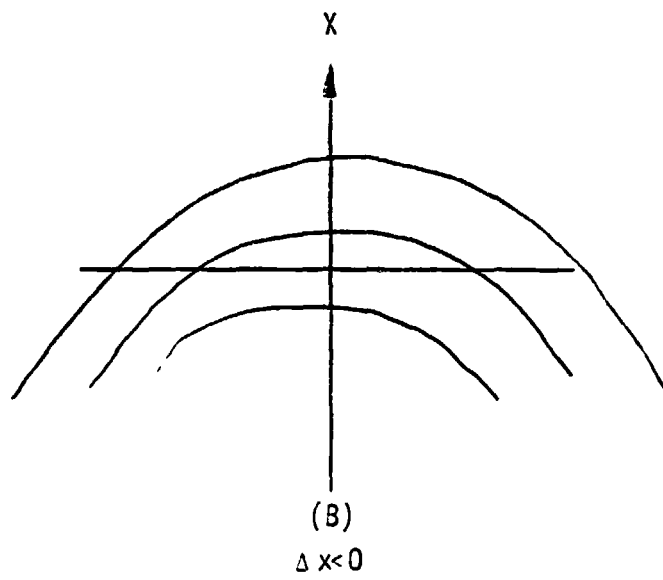
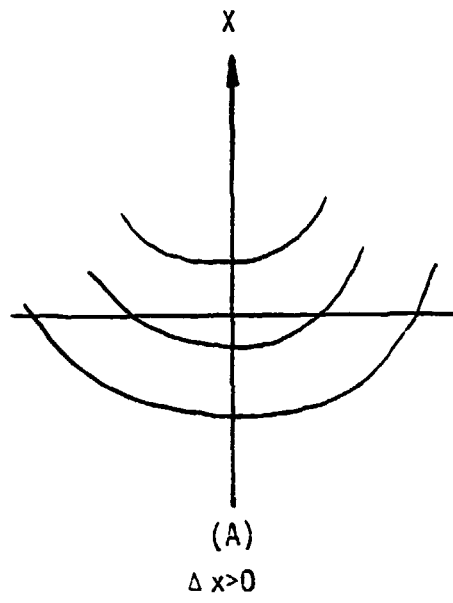


Figure 2
Two Theoretical Fringe Patterns

Figure 2B represents the fringe pattern on the screen. If the front plate in the sandwich specklegram is a recording of the undisplaced object Δz will be positive and the relative displacements caused by the image recorded on the screen are in a direction pointing toward the center of curvature.

III. EXPERIMENTAL SETUP AND PROCEDURE

Introduction

A moving blade was driven by a motor with a rotational speed over 3000 rpm. This model was comprised of a thick disk with two bars attached on the periphery of the disk. The experiment has three main steps. First, a speckle photograph was taken and developed of one of the bars of the model while the motor was rotating. Let this picture be called the "dynamic picture." Second, with the motor stopped, another speckle photograph of the same bar was taken, at the same position as that taken in the dynamic picture. This picture is called the "static picture." Third, these two film plates were sandwiched by a positioner and illuminated with a laser; then information pertaining to displacements and strains in the bar due to acceleration load was obtained.

Model

The model, a thick disk with two bars threaded into its periphery, was made of steel. The diameter of the disk was 3.50 inches, and the thickness of the disk was 1 inch. The central part of each bar was 3.25 inches long by .50 inches wide by .125 inches thick. Both ends of each bar were cylindrical in shape and threaded with a .50 inch thick diameter and 1.25 inches in length.

The end of each bar was threaded into the periphery of the disk with a 3.25-inch by .50 inch plane parallel to the surface of the disk. The two bars were 180 degrees apart on the disk. A threaded weight (87.52 grams) was attached to the free end of each bar to increase the dynamic load and to balance the assembly. This model assembly was axially attached to a .75-horsepower, 3540 rpm motor. Figures 3A and 3B show the supporting frame, motor and model. The rubber pads under the supporting frame, motor and model were to absorb vibrations.

Dynamics

The basic equipment for taking pictures (reference Figure 4) consisted of a Q-switched pulsed ruby laser [10], one Spectra-Physics, Inc. model 164 Argon Ion Laser with model 265 Exciter, two Textronix 549 storage oscilloscopes, one 0-7500 volts DC power supply. One pockel cell power supply, one Spectra-Physics 5 milliwatts Helium-Neon laser, and two photodiode detectors.

With the motor rotating, one of the bars would intersect the argon laser light path, so that oscilloscope I was triggered by photodetector I. After oscilloscope I was triggered, t_1 msec later it triggered oscilloscope II. After oscilloscope II was triggered, t_2 msec later it triggered the pulse generator; then the ruby laser fired. The angle between the position of the bar intersecting the argon laser light path and the position of the bar illuminated by the ruby laser light was about 180 degrees.

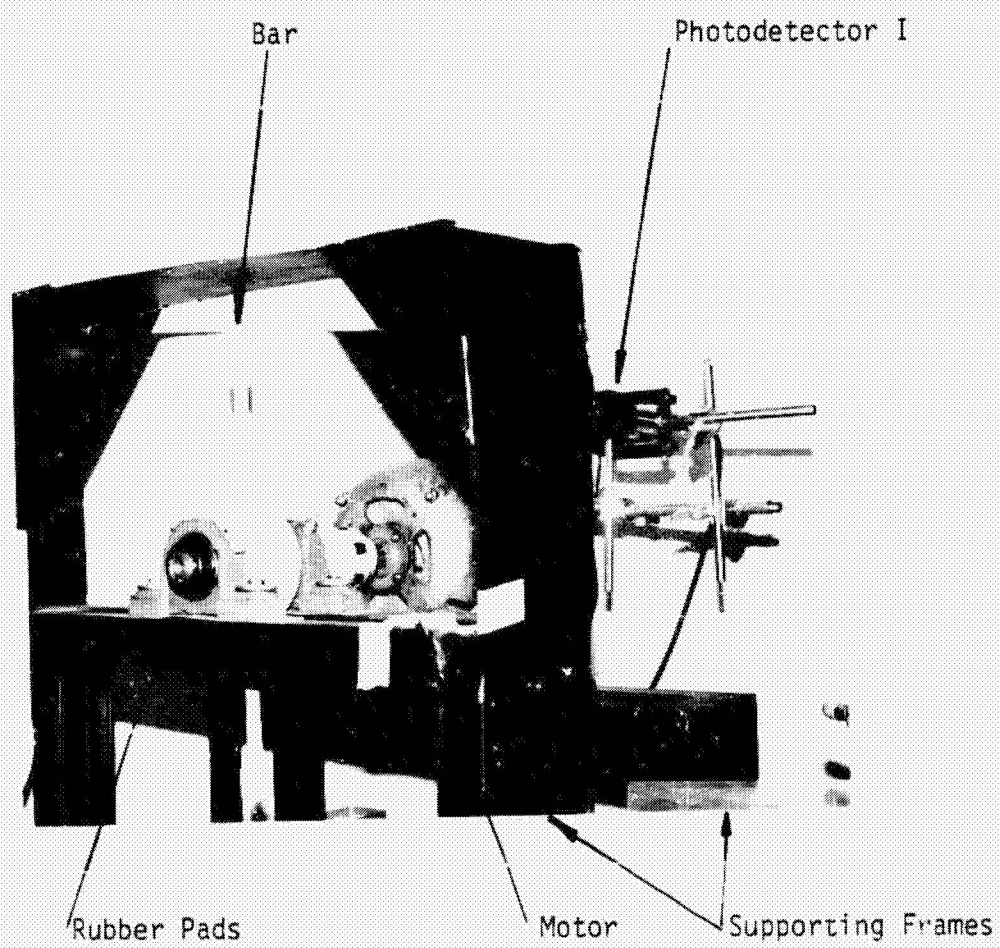


Figure 3A

Model and Motor and Supporting Frames
Front View

ORIGINAL PAGE IS
OF POOR QUALITY

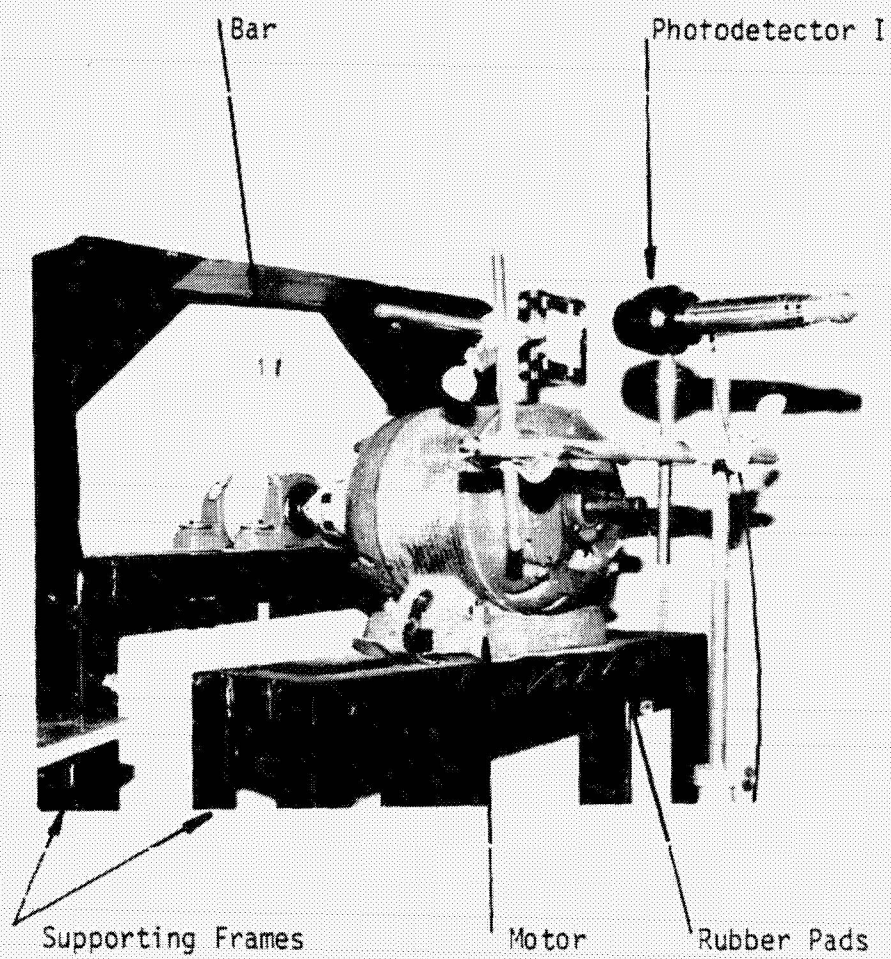


Figure 3B

Model and Motor and Supporting Frames
Back View

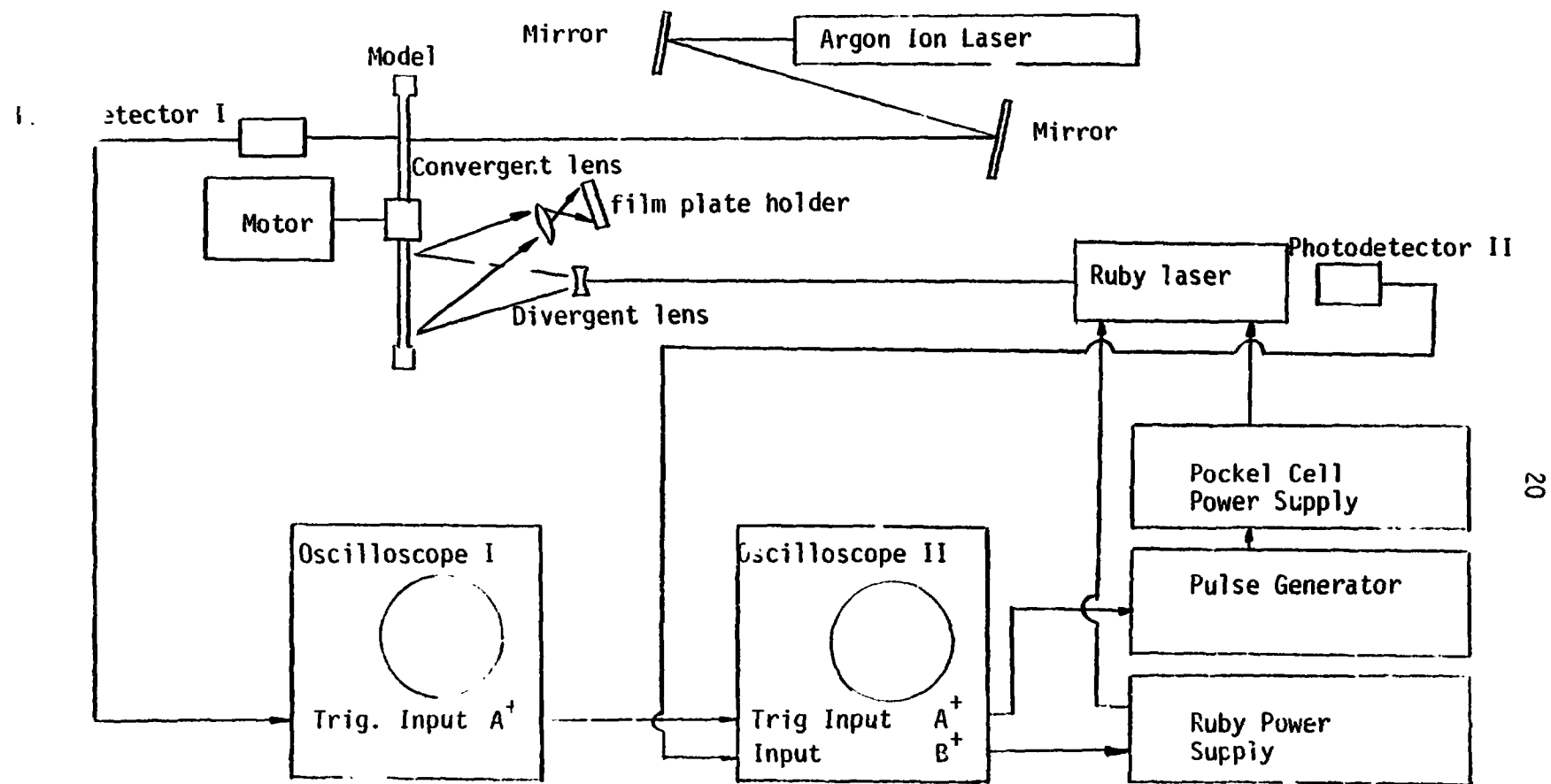


Figure 4

Schematic of the Equipment Layout
for Taking Dynamic Picture

So if the sum of t_1 and t_2 was very close to the value of the half period of the motor, one could get a dynamic speckle photograph with the bar in the proper position.

The following were the procedures for setting up the equipment:

1. The ruby laser was aligned [10].
2. A black paper target was put about 2 feet in front of the ruby laser, and the laser fired in its random mode [10]; the laser left a white spot on the black paper.
3. A five milliwatts He-Ne laser and two mirrors were placed on the top of the ruby laser as shown in Figure 5. The light beam which came from the He-Ne laser was parallel to the light beam which came from the ruby laser. The two mirrors were adjusted so that the He-Ne laser beam hit the white spot on the black paper. This aligned the path of the He-Ne laser with the ruby laser. The ruby laser is a pulse laser, so it was very difficult to use the ruby laser to help one set up the other equipment. But the He-Ne laser beam is a continuous beam, therefore one could use the He-Ne laser to help set up the other equipment.
4. The black paper was removed. The motor, model, rubber pads, and supporting frames were mounted in front of the ruby laser on the floating table. One of the model's bars was rotated to the position so that the He-Ne laser beam hit the central part of the bar.

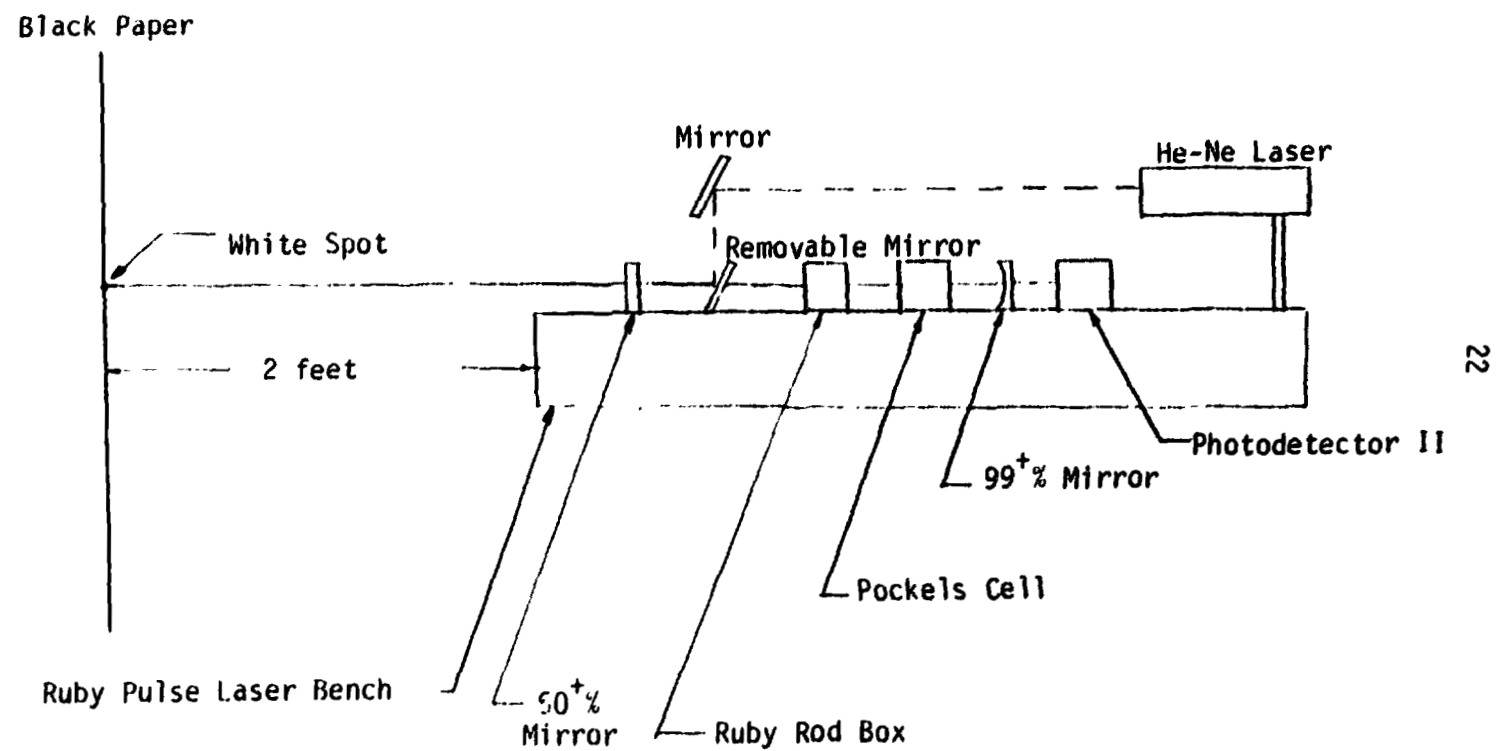


Figure 5
He-Ne Laser Setup

5. A ground glass was loaded in the film plate holder with the ground side of the glass away from the model. A flashlight was used to illuminate the model bar for positioning the convergent lens and film holder.

6. A divergent lens was positioned so that the He-Ne laser light illuminated the whole bar or the part of the bar that was to be photographed.

7. With the He-Ne laser off, the ruby laser was fired. The divergent light that came from the ruby laser was compared with the divergent light that came from the He-Ne laser. When the same area of the model bar was illuminated, the divergent lens was correctly aligned.

8. The He-Ne laser was turned on again. The image of the bar was observed by looking through the back of the ground glass toward the convergent lens. A piece of tape was placed on each side of the bar image as seen on the ground glass so that the image was exactly between these two pieces of tape. This helps one decide the delay times of the oscilloscopes for taking a dynamic picture.

9. The mirrors were adjusted so that the argon laser light (green continuous light) hit on the central part of the other bar of the model. The He-Ne laser was turned off.

10. Photodetector 1 was in the position where the argon laser light could hit directly after the model bar was rotated away.

The trigger input gate of oscilloscope I was connected to the photodetector I. A^+ gate of oscilloscope I was connected to the trigger input gate of oscilloscope II. B^+ gate of oscilloscope II was connected to the ruby laser power supply. A^+ gate of oscilloscope II was connected to a pulse generator. Further information regarding equipment settings is shown in the Appendix A. Photodetector I sent a pulse to trigger oscilloscope I, after t_1 msec delay. A^+ gate of oscilloscope I triggered oscilloscope II; after a t_2 msec delay, oscilloscope II sent a pulse from A^+ gate to trigger the pulse generator and caused the ruby laser to lase. The ruby laser included the flash lamp power supply, pockel cell power supply, and photodetector II. The pockel cell was used to inhibit lasing until the laser pulse was desired. Photodetector II was connected to the input gate of oscilloscope II, so the output of the ruby laser could be monitored.

11. The only remaining problem was how to determine the values of time periods t_1 and t_2 . The speed of the motor was 3540 rpm. so the half period of the motor was 8.47 msec. If one random lases the ruby laser, from the output mode shown on the screen of oscilloscope II, one knows that lasing took place only between .8 msec and 1.6 msec after the ruby laser's flash lamp initiation. Therefore, t_1 was set to equal 7.47 msec and t_2 was set to equal 1.0 msec as a first attempt. The steps used in taking

a dynamic picture (the steps are discussed later) were then followed using a ground glass instead of the regular film plate. When lasing took place, looking through the back of the ground glass toward the convergent lens, if the bar image was observed between the two pieces of tape on the ground glass, the oscilloscopes' time delays were correct. If the image didn't come exactly between the tapes, the time delay of oscilloscope I was adjusted and the above procedures were repeated again, until the image was exactly between the tapes.

12. The ground glass was removed from the film plate holder.

The following were the procedures for taking the dynamic picture:

1. All equipment was checked.

2. The motor was turned on and 3 minutes allowed for the motor to reach a steady state.

3. The argon laser was turned on; a black target card was put in front of the argon laser so that the black card covered the argon laser light.

4. The oscilloscope II was reset.

5. The light in the room was turned off.

6. The film plate was loaded on the film holder with the emulsion side of the plate away from the convergent lens. The name and number of the film plate used was Agfa 10E 75 NAH.

7. The pulse generator and pockel cell power supply were turned on.

8. The ruby laser power supply was turned on and the power control switch was adjusted so that the output power reached 1.5 kw.

9. The black card was removed.
10. Reset oscilloscope I and the ruby laser should lase.
11. The argon laser beam was covered again. The pockel cell power supply, pulse generator, ruby laser power supply and motor were turned off.
12. The film plate was unloaded from the film holder and it was protected from the light.
13. The light in the room was turned on.
14. One went to the dark room and the film plate was developed.

Static Picture

The film holder is shown in Figure 6A and 6B. There were two small pins fixed on the lower edge of the "window" and one small pin fixed on the left-hand side of the "window." There were three small screws that protruded from the back of the film holder. The lengths of these screws were all the same. When the film plate was loaded into the film holder, the face of the film plate should tightly rest against the three tips of the small screws and the two sides of the film plate should tightly rest against the three small pins on the edges of the "window." This procedure insured that the film could be loaded in the same position each time.

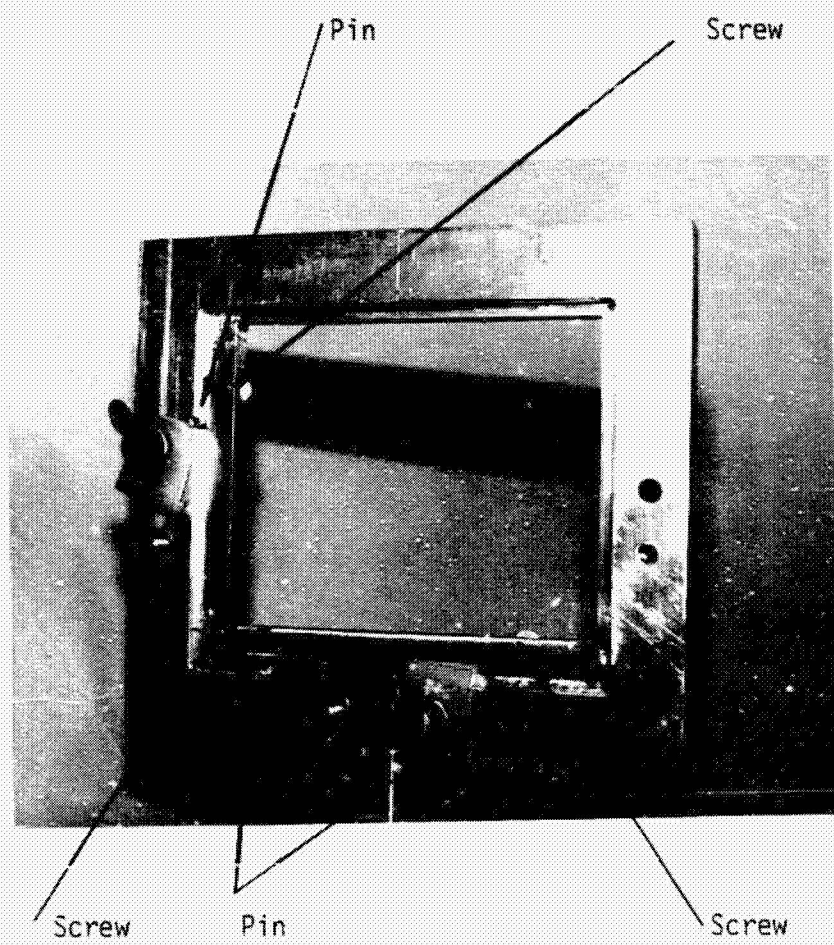


Figure 6A
Film Holder (Front View)

ORIGINAL PHOTO OF
FILM HOLDER

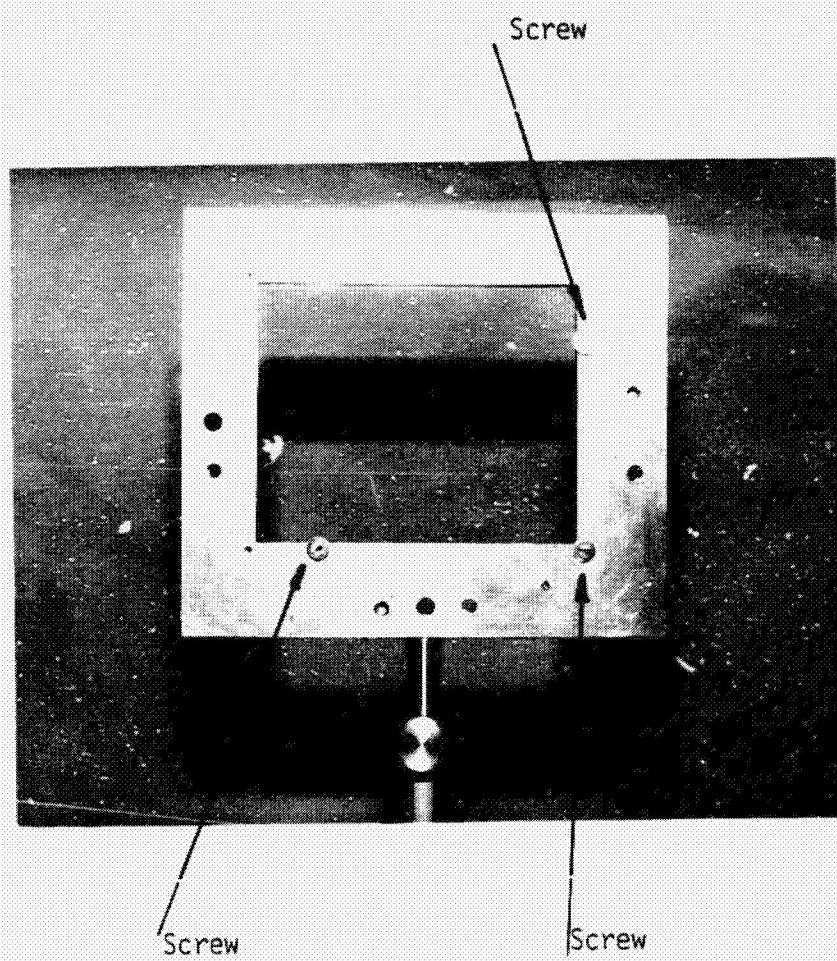


Figure 6B
Film Holder (Back View)

After the negative of the dynamic picture was developed, the negative was loaded back into the film holder as noted above. A light (flashlight) was used to illuminate the model bar and its image was viewed through the negative. The bar was slightly rotated until the projected image and the negative image coincided. The negative was removed, and a clean glass plate with the same thickness as that of the negative was loaded into the film holder. With the room light off, a new film plate was loaded into the film holder with the emulsion side resting against the clean glass plate, (the clean glass plate was between the convergent lens and the film plate). The ruby laser was fired. The film plate was removed and developed. The two speckle photographs (dynamic and static), were placed emulsion to emulsion in the positioner (the positioner will be discussed in the next section) and illuminated by the argon laser light. If a set of fringes was readily observed on the screen, then the data collection was successful. If the data was not observed, the model bar was not at the correct position. By trial and error, one rotated the model bar to the right or to the left .004 or .005 inch, and took another static speckle photograph and again observed the resulting data, until a set of fringes was observed.

Positioner

The positioner was a device for sandwiching the dynamic and static speckle photographs. A photograph of the positioner is shown in Figure 7. This device had two main parts: a main frame and a translation stage. Figure 8 is a photograph of the main frame, and Figures 9A and 9B are the photographs of the translation stage. The three screws on the main frame could fix the position of the translation stage so that the translation stage rotates without translation along the screws. Two small spring clips control the vertical and horizontal movements of the four by five-inch box inside the translation stage. The static and the dynamic speckle photographs were sandwiched together, emulsion to emulsion, such that the images were almost geometrically matched. This sandwich of negatives was then placed in the positioner such that one negative was on the window of the main frame and the other was below the box window of the translation stage. The positioner was made of steel. The weight of the translation stage made the two negatives press each other tightly. The three screws were set at the correct positions so that the translation stage was fixed. The translation stage was rotated by moving the handle and translated by turning the spring clips until the two images were precisely matched. Displacement data was observed by passing a narrow laser beam through the photographic images. The laser and positioner setup for data recovery is shown in Figure 10.

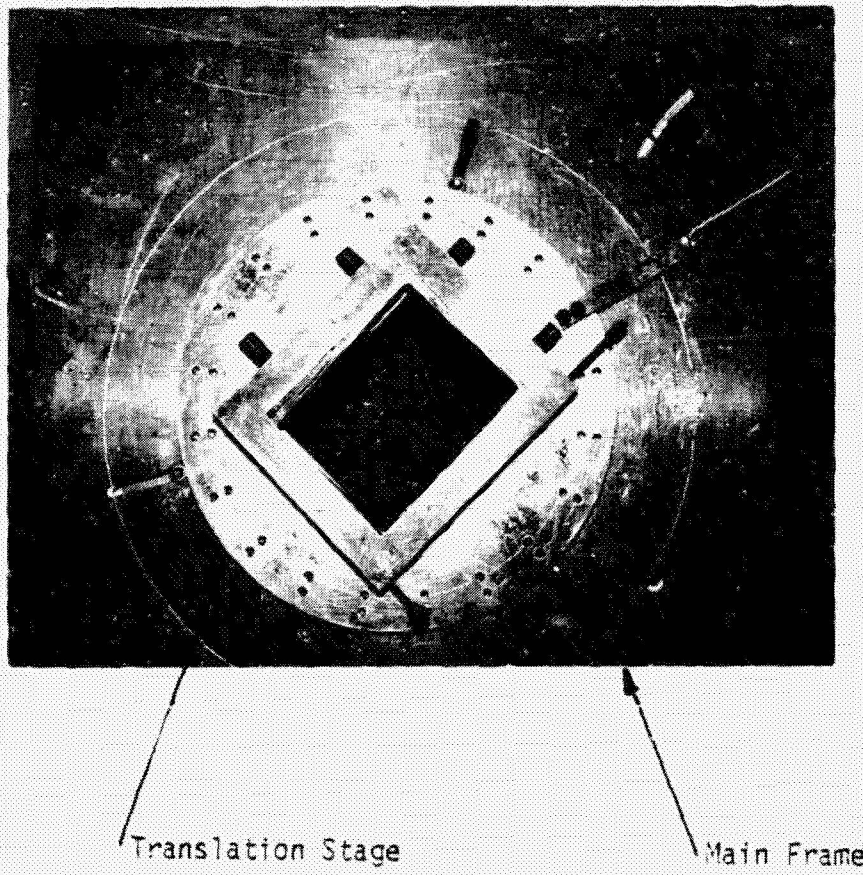


Figure 7
Positioner

ORIGINAL PHOTO IS
OF MUCH QUALITY

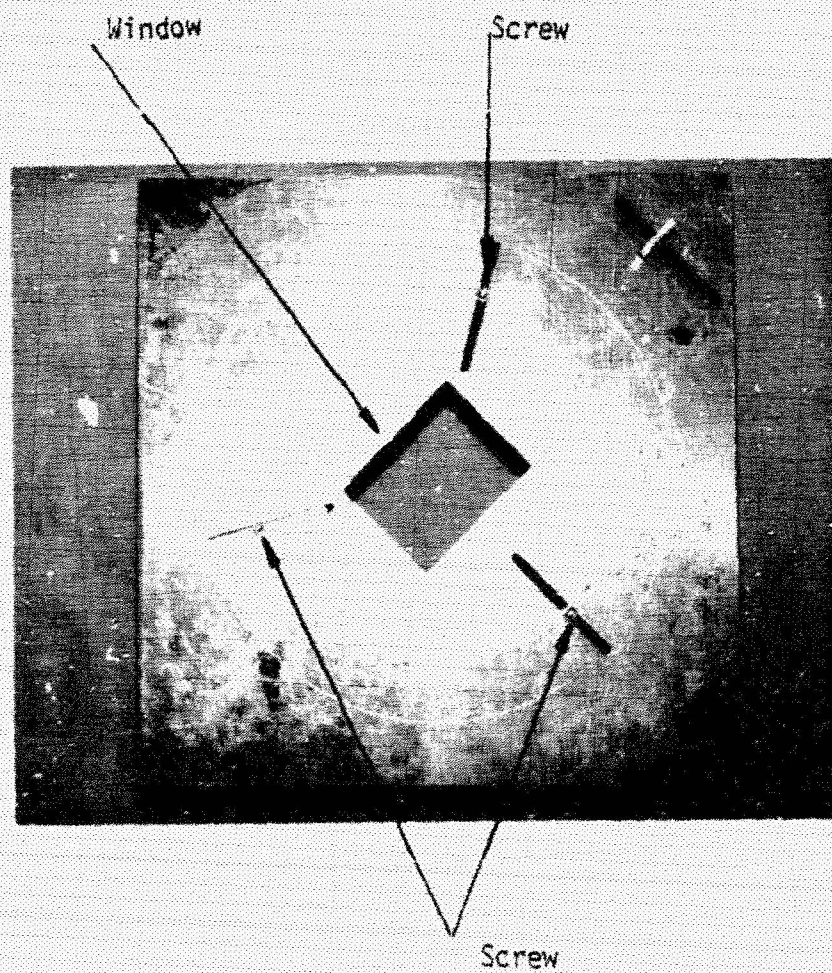
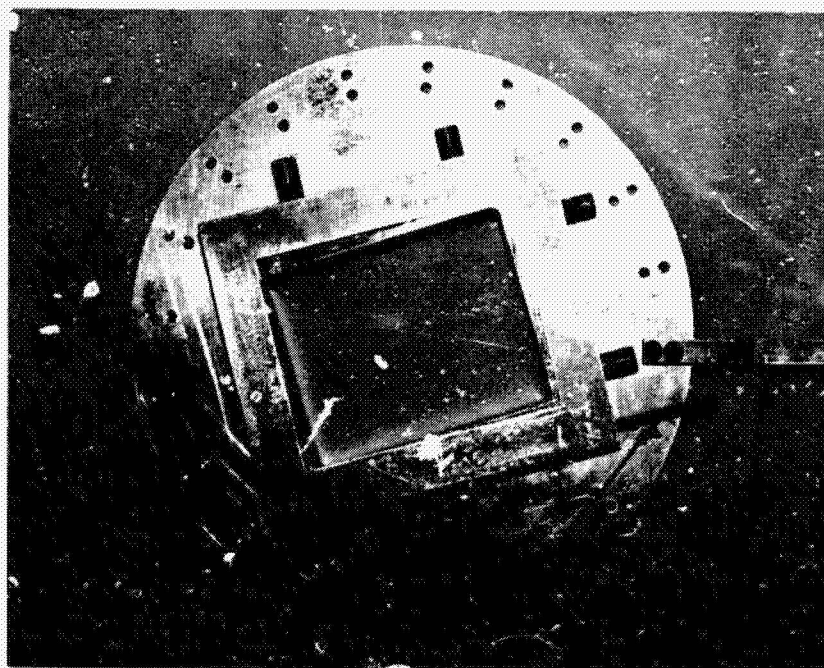


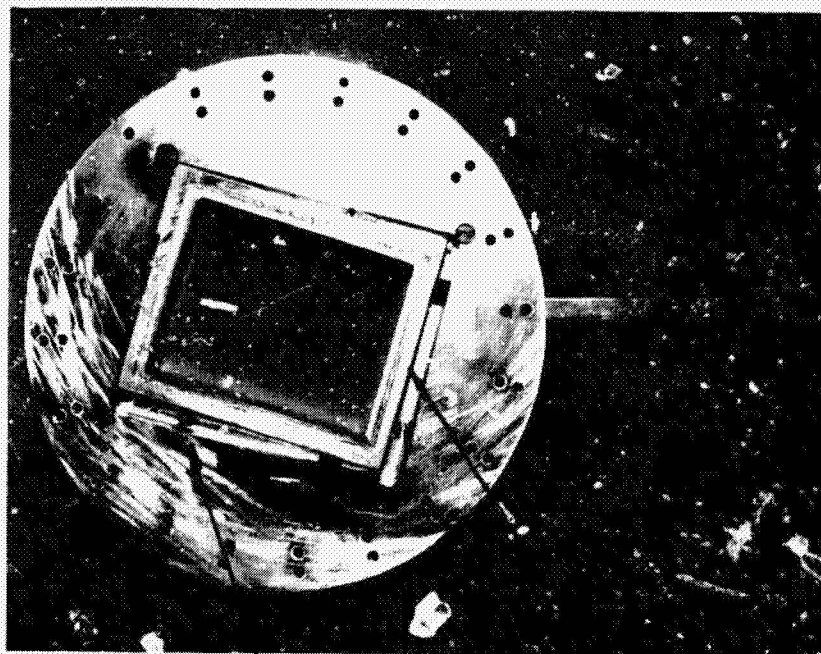
Figure 8
Main Frame of The Positioner



Spring Clips

Handle

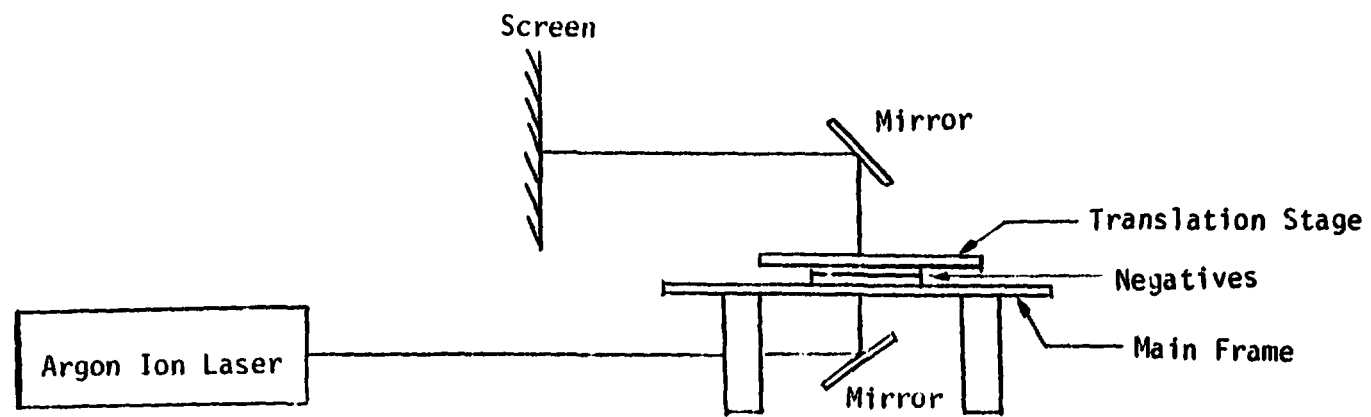
Figure 9A
Translation Stage of The Positioner
Top View



Spring

Window

Figure 9B
Translation Stage of The Positioner
Bottom View



35

Figure 10
Laser and Positioner Setup for Data Recovery

IV. EXPERIMENTAL RESULTS

By means of the method discussed in the last chapter, displacements can be evaluated and strain information calculated for the moving bars. Several of the fringe patterns from the collected data are shown in Figure 11. From the pictures of Figure 11, the fringes are obviously a set of straight lines. This suggests that the weight of the positioner was sufficient to keep contact between the two negative emulsions, which is to say that Δz almost equals zero.

If a Cartesian coordinate is defined on the beam (Figure 11) the original point is a specific point of the model bar, the X-axis is along the center line of the beam being positive away from the center of the disk, and the positive Y-axis is tangent to the disk. The coordinates (in inches) of three points on the bar used as example points are Point 1-(2.125, .0), Point 2-(2.417, .0) and Point 3-(2.75, .0). The magnification factor of the negative was 1.5, so the coordinates of the three points on the negative are Point 1-(3.1875, .0), Point 2-(3.625, .0) and Point 3-(4.125, .0).

To calculate strain at a point, say $(x, .0)$, the following procedures were executed. First, the fringe patterns of two neighborhood points on the negative: Point A $(x+.0625, .0)$ and Point B $(x-.0625, .0)$ were observed at each example point 1, 2, and 3. Next, Δx for these two neighborhood points was calculated according

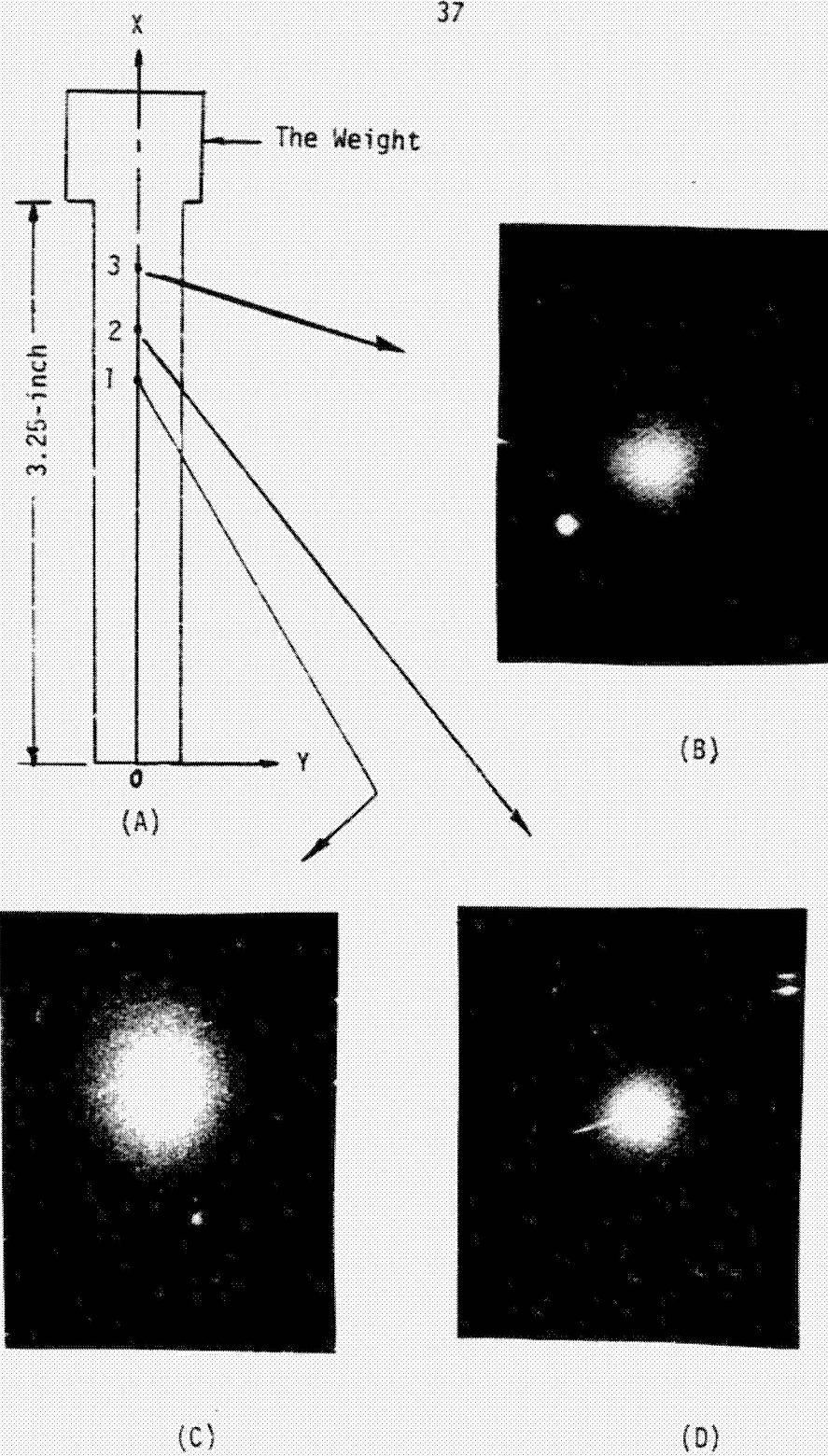


Figure 11

The Typical Fringe Patterns

ORIGINAL PAGE IS
OF POOR QUALITY

to equation (34) in Chapter Two (where $\lambda = 5145 \times 10^{-8}$ cm = 2025.59 $\times 10^{-8}$ inch). Strain at the particular example point was calculated by means of the difference between the Δx 's of Points A and B divided by .125 inch.

Calculations for the information shown in Table 1 were made using this procedure. The calculations of theoretical results are shown in Appendix B.

It should be noted that the Δx 's of Point A and Point B in Table 1 are not the exact displacements of Point A and Point B but are the sum of the exact displacement and the miss-matched movement between two negatives. For each set of data, the miss-matched movement of each point is the same. The experimental displacements get larger when the observation points are closer to the free end of the bar. The Δx 's of set 1 get larger as the observation points are moved toward the free end of the bar. For each point, Δx is greater than the experimental displacement; thus, the miss-matched movement is a positive value. The Δx 's of set 2 and set 3 get smaller as the observation points approach the free end of the bar, and one knows miss-matched movement is a negative value. Because of this mismatch the experimental displacements are not the same as the theoretical displacements; but the experimental strains which are the slopes of the displacement curves should match the theoretical strains.

With a relatively small distance R, one can see from Table 1 that the difference of fringe spacing between any two adjacent points

Table 1
The Theoretical and Experimental Displacement and Strain Data

| | | Fringe Spacing of Pt. A $\times 10^{-1}$ in | Fringe Spacing of Pt. B $\times 10^{-1}$ in | Δx of Pt. A $\times 10^{-3}$ in | Δx of Pt. B $\times 10^{-3}$ in | Experimental Strain $\times 10^{-4}$ in/in | Theoretical Disp. $\times 10^{-3}$ in | Theoretical Strain $\times 10^{-4}$ in/in | Error of Strain % |
|--------------------------------|-------|--|--|---|---|--|---|---|-------------------------|
| Set 1 R = 22.25- inch | Pt. 1 | 2.4609 | 2.5098 | 1.8314 | 1.7958 | 2.8504 | 0.7273 | 2.9511 | 3.41 |
| | Pt. 2 | 2.2656 | 2.3047 | 1.9893 | 1.9555 | 2.6973 | 0.8395 | 2.9251 | 7.79 |
| | Pt. 3 | 2.0703 | 2.1094 | 2.1769 | 2.1366 | 3.2251 | 0.9676 | 2.8769 | 12.10 |
| Set 2 R = 22.25- inch | Pt. 1 | 2.1875 | 2.1484 | 2.0603 | 2.0978 | 2.9968 | 0.7273 | 2.9511 | 1.55 |
| | Pt. 2 | 2.3437 | 2.3047 | 1.9230 | 1.9555 | 2.6074 | 0.8395 | 2.9251 | 10.86 |
| | Pt. 3 | 2.5781 | 2.5293 | 1.7481 | 1.7819 | 2.6998 | 0.9676 | 2.8769 | 6.16 |
| Set 3 R = 87.375 inch | Pt. 1 | 8.5937 | 8.4375 | 2.0595 | 2.0976 | 3.0510 | 0.7273 | 2.9511 | 3.38 |
| | Pt. 2 | 8.8281 | 8.6719 | 2.0048 | 2.0409 | 2.8898 | 0.9251 | 2.9251 | 1.21 |
| | Pt. 3 | 9.0625 | 8.9062 | 1.9529 | 1.9872 | 2.7410 | 0.9676 | 2.8769 | 4.72 |

is very small. This is because the image on the screen is small so the difference of fringe spacing is not easily evaluated.

The data of set 3, $R = 87.375$ inches. The image on the screen is much larger and the difference in the fringe spacing between any two adjacent points is more readily and accurately determined. From Table 1, it can be seen that the experimental strains of set 3 are closer to the theoretical strains. Thus, the distance from negative to screen is an important variable in interpreting the data.

Stress information can be calculated from strain data and Hooke's Law.

V. Conclusion

The theory and technique for the formation of fringes in a sandwich specklegram were developed and extended to the determination of surface stress distribution in any rotating element problem. This technique can cancel rigid body movements of the test specimen so that one can get the deformation of the rotating element. The strains are calculated by differentiating displacement data. Experimental results and theoretical results are in good agreement.

The range of displacement measurement for the conventional speckle photography method is from 200×10^{-6} inches to $20,000 \times 10^{-6}$ inches. When the displacements of the specimen are less than 200×10^{-6} inches, the conventional speckle photography method is useless [9]. The displacement one gets from the sandwich speckle photography method are the sum of the actual displacement of the specimen and the miss-matched movement of the negatives. Therefore if one uses the sandwich speckle photography method, even though the displacements of the specimen are less than 200×10^{-6} inches, one still can get displacement data and strain can then be calculated.

When one uses the sandwich specklegram method to analyze the stress distribution in any rotating element problem, two things should be noted. First, the time delays of the oscilloscopes must

be very accurate to obtain a dynamic speckle photograph. Second, the distance from the positioner to the screen should be examined and optimized for the most accurate analysis of data.

REFERENCES

1. Allen, J. M. and Erickson, L. B., "NASTRAN Analysis of a Turbine Blade and Comparison with Test and Field Data," The Gas Turbine Division of The American Society of Mechanical Engineers for presentation at the Gas Turbine Conference & Products Show, Houston, Texas, March 2-6, 1975.
2. Stetson, K. A., "Optical System for Dynamic Analysis of Rotating Structures - Third Interim Technical Report, Phase III - System Application," United Technologies Research Center Report R 76-992054-300, July 1976.
3. Sikora, J. P. and Mendenhall, F. T. Jr., "Holographic Vibration Study of a Rotating Propeller Blade," Experimental Mechanics, June 1974, pp. 230-232.
4. Stetson, K. A., "The Use of an Image Derotator in Hologram Interferometry and Speckle Photography of Rotating Objects," Experimental Mechanics, February 1978, pp. 67-73.
5. Archbold, E., Burch, J. M., and Ennos, A. E., "Recording of In-Plane Surface Displacement by Double-Exposure Speckle Photography," Optics Acta, Vol. 17, No. 12, 1970, pp. 883-898.
6. Archbold, E. and Ennos, A. E., "Displacement measurement from Double-Exposure Laser Photographs," Optics Acta, Vol. 19, No. 4, 1972, pp. 253-271.
7. Abramson, N., "Sandwich Hologram Interferometry: A New Dimension in Holographic Comparison," Applied Optics, Vol. 13, No. 9, 1974, pp. 2019-2025.
8. Maddux, B. E. and Adams, F. D., "Development of a Dual-Plate Technique for Speckle Photography," 1976 SESA Spring Meeting, Silver Spring, Maryland, May 9-14, 1976.
9. Kinariwala, V. R., Peters, W. H., Ranson, W. F. and Swinson, W.F., "Speckle Patterns for Measuring Displacements Described as Diffraction Gratings," Proceedings of 12th Annual Meeting of Society of Engineering Science held at The University of Texas at Austin, Texas, October 1975, pp. 413-421.
10. Turner, J. L., "A Modulated Pulsed Ruby Laser System for Dynamic Holographic Interferometry," Master's thesis, Department of Mechanical Engineering, Auburn University, Auburn, AL., Dec., 1972.

APPENDICES

APPENDIX A
EQUIPMENT SETTINGS

APPENDIX A
EQUIPMENT SETTINGS

Ruby Laser Bench

aperture: .109" diameter

Ruby Lamp Power Supply

Capacitor voltage: 1.6 kilovolts

Pulse Generator

pulse width: 1.5 microseconds

mode: pulse delay

pulse position: 15 microseconds

output pulse amplitude: maximum

Pockel Cell Power Supply

meter reading: 9.5 microamperes

Oscilloscope I

mode: B intensified by A

delay for A: 7.52 milliseconds

time base A: 5 microseconds/cm

time base B: 1.0 milliseconds/cm

sweep setting: single sweep

coupling B: AC

slope: positive

Oscilloscope II

47

mode: B intensified by A
delay for A: 1.0 milliseconds
time base A: 5 microseconds/cm
time base B: .2 milliseconds/cm
sweep setting: single sweep
coupling B: AC
slope: positive
input: 2 volts/cm

APPENDIX B
THEORETICAL RESULTS

APPENDIX B

THEORETICAL RESULTS

A moving model is driven by a motor with a rotational speed 3540 rpm. The model, a thick disk with two bars threaded into its periphery, is made of steel. The radius of the disk is r . The central part of each bar is L long by b wide by t thick (referring to Figure 3A, Figure 3B, and Figure 11). Both ends of each bar are cylindrical in shape and threaded with a b -inch diameter and L_t in length. One end of each bar is threaded into the periphery of the disk. The two bars are 180 degrees apart on the disk. A threaded weight M is attached to the free end of each bar to increase the dynamic load and to balance the assembly.

If the model and the threaded weight are assumed to be homogeneous and mass distribution is uniform, then the force acting on the bar is

$$F_x = M \left(R + L + \frac{1}{2} L_t \right) \omega^2 + \rho \cdot L_t \left(\frac{\pi b^2}{4} \right) \left(R + L + \frac{1}{2} L_t \right) \omega^2 \\ + b \cdot t \cdot (L - X) \cdot \rho \cdot \left[R + X + \frac{1}{2} (L - X) \right] \omega^2 \quad (A1)$$

$$F_x = \left(M + \frac{1}{4} \pi \rho L_t b^2 \right) \left(R + L + \frac{1}{2} L_t \right) \omega^2$$

$$+ \rho b t (L - X) (R + \frac{1}{2} L + \frac{1}{2} X) W^2 \quad (A2)$$

where

W is the angular velocity of the rotating model

ρ is the density of the model

$$\sigma_x = \frac{F_x}{A} = \frac{F_x}{bt} \quad (A3)$$

where

σ_x is the normal stress of the bar

A is the cross section area of the bar

According to Hooke's Law one can get the strain and displacement by

$$\varepsilon_x = \frac{\sigma_x}{E} \quad (A4)$$

and

$$U_x = \varepsilon_x d x \quad (A5)$$

FINAL REPORT
(PART II)

GENERAL SHEARING SPECKLE INTERFEROMETRY
AND BOUNDARY-INTEGRAL EQUATION TECHNIQUES
IN EXPERIMENTAL MECHANICS

by

W. F. Ranson and F. A. Moslehy

Submitted to

NASA
Lewis Research Center
Cleveland, Ohio

through

School of Engineering
University of South Carolina
Columbia, South Carolina 29208

April 1980

This report is prepared as a subcontract to Auburn University,
Auburn Alabama under contract to NASA/Lewis Research Center Contract
NSG3233.

ABSTRACT

Laser speckle interferometry is used as an experimental technique to measure in-plane surface displacement components of a deformed solid. A general theory of laser speckle interferometry which includes both the contributions of in-plane and out of plane deformations is developed and verified through several experimental examples. The basic information consists of a double exposure photographic record of a sheared wavefront of the image of the surface points of a body in a reference and deformed configurations.

Data analysis in speckle interferometry yields a map of the surface displacement components along a specified closed contour for the region of interest. The experimental displacement values are then used as input data to numerically calculate, with a high degree of resolution, the state of stress at any desired interior point using the boundary-integral equation method. This method is based on the use of an integral constraint equation which relates boundary displacements and corresponding boundary tractions in a well-posed boundary value problem.

Several examples are presented to illustrate the application of the coupled laser speckle interferometry and boundary-integral solution technique to two-dimensional elasticity problems. This coupled technique between laser speckle interferometry and the numerical boundary-integral equation method proved to be an accurate and efficient procedure for solving significant engineering problems.

TABLE OF CONTENTS

| | Page |
|--|------|
| LIST OF ILLUSTRATIONS | vii |
| LIST OF TABLES | ix |
| NOMENCLATURE | x |
| I. INTRODUCTION | 1 |
| II. GENERAL SHEARING SPECKLE INTERFEROMETRY | 5 |
| 2.1 Introduction | 5 |
| 2.2 General Theory of Fringe Formation | 6 |
| 2.3 Experimental Verification of the General Shearing Speckle Interferometry Equations . . . | 14 |
| III. THE BOUNDARY-INTEGRAL EQUATION METHOD FOR ELASTICITY PROBLEMS | 26 |
| 3.1 Brief Introduction | 26 |
| 3.2 Mathematical Formulation of the BIE Method . . . | 27 |
| 3.3 Formulation of the Numerical Solution Technique for Plane Problems | 40 |
| IV. THE EXPERIMENTAL PROGRAM AND DATA ACQUISITION | 54 |
| 4.1 Experimental Equipment | 54 |
| 4.2 Computer-Aided Data Reduction System | 56 |
| 4.3 Example 1 - Flexure of a Cantilever Beam with a Transverse End Load | 60 |
| 4.4 Example 2 - Circular Disk Under Diametral Compression | 66 |
| 4.5 Example 3 - A Plate with a Central Circular Hole Subjected to Uniform Axial Tension | 69 |

| | Page |
|---|------|
| V. RESULTS AND DISCUSSION | 72 |
| 5.1 The Coupling of the BIE and Laser Speckle Techniques | 72 |
| 5.2 The Cantilever Beam Problem | 72 |
| 5.3 The Circular Disk Problem | 77 |
| 5.4 The Stress Concentration Problem | 82 |
| VI. CONCLUSIONS | 85 |
| LIST OF REFERENCES | 87 |

LIST OF ILLUSTRATIONS

| Figure | | Page |
|--------|--|------|
| 2-1 | Shearing Speckle Interferometry | 7 |
| 2-2 | Displacement Vectors | 8 |
| 2-3 | Arrangement for Optical Fourier Transform | 11 |
| 2-4 | Rectangular Plexiglas Beam with a Transverse End Load | 14 |
| 2-5 | Geometrical Configuration for the First Experimental Example | 16 |
| 2-6 | Data Analysis for Point-Wise Filtering in In Plane Measurements | 18 |
| 2-7 | Schematic for Determining the In Plane Displacement Components | 19 |
| 2-8 | Comparison of Theoretical and Experimental Values of Beam Deflection Along the x-Axis | 20 |
| 2-9 | Geometrical Configuration for the Second Experimental Example | 21 |
| 2-10 | Comparison of Theory and Experiment Along the x-Axis for the Second Experimental Example | 24 |
| 3-1 | Development of Somigliana Identity | 31 |
| 3-2 | Limiting Procedure for p Approaching Smooth Boundary | 35 |
| 3-3 | Integration Along Boundary Segment (σ) | 42 |
| 3-4 | Linear Boundary Element | 45 |
| 3-5 | Multiply Connected Body | 52 |
| 4-1 | Experimental Arrangement for Recording a Specklegram | 55 |
| 4-2 | Computer Aided Data Analysis System for Laser Speckle Interferometry | 57 |

| Figure | | Page |
|--------|---|------|
| 4-3 | Typical Speckle Photography Fringe Pattern Used in the Optical Data Analysis System | 58 |
| 4-4 | Bending of Cantilever Beam with a Transverse End Load | 61 |
| 4-5 | Comparison of Theoretical and Experimental Values of the Horizontal Displacement Component Along the Free End | 62 |
| 4-6 | Comparison of Theoretical and Experimental Values of the Vertical Displacement Component Along the Free End | 63 |
| 4-7 | Diametrically Loaded Circular Disk | 67 |
| 4-8 | Displacement Components Along Line $y = d/4$ | 68 |
| 4-9 | A Plate with a Hole under Axial Loading | 70 |
| 5-1 | BIE Model for the Region of Interest of the Cantilever Beam Problem | 73 |
| 5-2 | BIE Model for the Region of Interest of the Circular Disk Problem | 78 |
| 5-3 | Horizontal Displacement Components Along Line $y = 0$ | 80 |
| 5-4 | Vertical Displacement Components Along Line $x = 0$ | 81 |
| 5-5 | Twenty-Seven Segment BIE Model Used for the Stress Concentration Problem | 83 |

LIST OF TABLES

| Table | | Page |
|-------|---|------|
| 4-1 | Experimental Values of the Displacement Components Along Section $x=3$ inches for the Cantilever Beam Example | 65 |
| 4-2 | Measured Displacements Along the x -axis for the Cantilever Beam Example | 65 |
| 4-3 | Measured Displacements Along the Circular Contour of the Region of Interest for Example 3 | 71 |
| 5-1 | Results of the BIE Calculations for the Cantilever Beam Problem | 75 |
| 5-2 | Comparison between Calculated and Measured Values of the Beam Deflection Along the x -axis . . | 76 |
| 5-3 | Comparison of the BIE Calculations and Theoretical Solution Along the Horizontal Diameter for the Circular Disk Problem | 79 |
| 5-4 | Comparison of the BIE Calculations and Theoretical Solution Along the x -axis for the Stress Concentration Problem | 84 |

NOMENCLATURE

| | |
|-----------------------------------|--|
| $a(x,y)$ | Amplitude modulus of light wave |
| $A(\omega_1, \omega_2)$ | Fourier transform of modulus function $a(x,y)$ |
| b_i | Body force components |
| d | Distance between transparency and transform plane |
| $\vec{e}_x, \vec{e}_y, \vec{e}_z$ | Unit vectors in x,y,z directions |
| \vec{e}_i | Unit vector in the x_i direction |
| E | Modulus of Elasticity |
| \bar{E} | Complex amplitude of light wave |
| \bar{E}^* | Complex conjugate of light amplitude |
| $g(x,y)$ | Light amplitude transmission function |
| $G(x,y)$ | Light amplitude in the Fourier transform plane |
| I, I_{TOTAL} | Light intensity |
| $J(\xi)$ | Jacobian |
| l | Length of a rectangular beam |
| l,m,n | Direction cosines |
| M | Number of boundary segments - Camera magnification factor |
| n | Fringe order |
| \vec{n} | Unit normal vector |
| N | Total number of nodes |
| $N^a(\xi)$ | Shape functions |
| P | Load |

ORIGINAL PAGE IS
OF POOR QUALITY

| | |
|--|--|
| \vec{q} | Unit tangential vector |
| r | Distance |
| t_i | Traction vector components |
| t_i^*, u_i^* | Solution to Kelvin's problem (tractions, displacements) |
| T_{ji}, U_{ji} | Fundamental second order tensors components (tractions, displacements) |
| S_{kij}, D_{kij} | Third order tensors components (tractions, displacements) |
| \vec{U} | Displacement vector |
| u, v, w | Displacement components in x,y,z directions |
| u_i | Displacement component in the x_i direction |
| \vec{U}_f | Displacement vector in film plane |
| u_f, v_f | Displacement components in the film plane |
| w_y, w_z | Terminal end loads on a cantilever beam |
| X_i | Body force components |
| $\left. \begin{array}{l} x, y, z \\ x_i \\ \underline{x} \end{array} \right\}$ | Rectangular coordinates |
| x_s, y_s | Coordinates on Fourier transform plane |
| α | Wedge angle |
| δ | Deflection of free end of a cantilever beam |
| $\delta(\omega_1, \omega_2)$ | Delta function |
| Δ_i | Separation on film plane |

| | |
|----------------------|--|
| $\delta x, \delta y$ | Incremental distances |
| $\Delta x, \Delta y$ | Shift in x and y directions |
| $\theta(x,y)$ | Phase of light wave |
| $\Delta\theta$ | Change in phase due to deformation of a body |
| λ | Wavelength of light |
| μ | Shear modulus |
| ν | Poisson's ratio |
| ξ | Intrinsic coordinate |
| σ_{ij} | Stress components |
| $\vec{\omega}$ | Angular spatial-frequency |

I. INTRODUCTION

Recent advances in the area of experimental stress analysis utilizing coherent optics have been through the development of holographic and laser speckle interferometry. These optical techniques have been applied successfully to the measurement of the surface displacements of deformable solids[1,2,3,4,5,6]*. While holographic and speckle interferometry measure surface displacements, speckle shearing interferometry determines directly the derivatives of surface displacements [7,8].

Original applications in holography suggested that the modern techniques in using the laser would possibly change the method of measurement of strains. However, this has not been the case, although many important engineering examples have been demonstrated. Difficulties exist in holography because of the sensitivity of the measurements which require vibration isolation and the ability to separate displacement components from a single hologram. Introduction of the laser speckle effect has provided for a technique of surface displacement measurements without the need of vibration isolation. In addition, this technique is a direct measure of in-plane displacement components, thus the separation of components is accomplished easily. All coherent optical methods are a measure of surface displacement or its derivatives on the boundary of a solid,

* Numbers in brackets refer to the list of references.

thus the need still exists to calculate strain and stress components at any location from the surface displacement data.

The boundary-integral equation (BIE) method is well suited to the analysis of laser speckle surface displacement data. This method derives its foundations from the application of classical potential theory [9], and was used to provide numerical solution for the two dimensional Laplace equation by Jaswon [10] and Symm [11]. The numerical BIE method has been applied to two-dimensional problems of elasticity by Rizzo [12] and subsequently extended to three-dimensional problems by Cruse [13, 14,15]. In addition, boundary-integral methods have been used successfully to solve problems in elastodynamics [16,17], elastic inclusions [18], elastoplasticity [19,20], fracture mechanics [21,22], thermoelasticity [23], anisotropic elasticity [24], time-dependent inelastic deformation [25], axisymmetric problems [26], and plate [27] and shell problems [28]. Also, the possibility of coupling the BIE method with the finite element method has been shown [29].

Basically, the BIE method for elasticity combines a reciprocal work theorem and a suitable singular solution to the governing differential equation to construct a boundary formula which is a relation between boundary displacements and corresponding boundary tractions in a well-posed problem. Since either of these boundary quantities, in principle, determines the other, the formula provides a constraint between them which generates a set of simultaneous integral equations from suitable boundary data. The unknowns in

the equations are boundary tractions or displacements directly. An outstanding conceptual advantage of the boundary formula approach is that it applies to three-dimensions as well as two with similarly defined integral equations arising in each case. The key feature of the boundary integral equation is that it couples boundary data for the given problem. As a result, the problem size is reduced by one dimension (with a corresponding decrease in computer core requirements). Furthermore, since the numerical discretization is performed at the boundary and not throughout the interior, a high resolution for the interior solution may be obtained at any desired location. This is particularly crucial for analysis of problems with significant stress gradients.

In principle, the optically measured surface displacements become input data needed for the BIE to calculate the unknown tractions at specified points on the boundary. In regions of high stress gradients or where loading is unknown, a closed contour (two-dimensional problems) may be defined around the region of interest and the displacement components are then measured experimentally at specified nodal points on that contour. Stresses at any interior point in that region may be obtained accurately by comparatively simple quadrature once all the contour tractions and displacements are determined.

The coupling of these two solution techniques becomes more compatible when the displacement data can be stored in the computer directly without the need of time consuming data analysis. Automated data analysis systems have been developed [5] for use in

laser speckle interferometry which will record and store in memory in a computer the displacement components around a specified closed contour.

The subject of this dissertation is the extension of the use of the numerical boundary integral technique for elasticity problems through the coupling of laser speckle interferometry measurements. A general theory of laser speckle interferometry which includes both the contributions of in-plane and out of plane deformations is developed and discussed in Chapter II. The mathematical formulation of the BIE method for elastostatics and the numerical solution for plane problems are discussed in Chapter III. A computer aided data reduction system is also discussed, and several example problems are presented to illustrate the coupling of the two solution techniques.

II. GENERAL SHEARING SPECKLE INTERFEROMETRY

2.1 Introduction

When a diffuse surface of a structure is illuminated by coherent light, a grainy speckle effect is imaged by the eye or film plane of a camera due to the random interference of light reflected from the surface. This phenomenon is known as the speckle effect. Laser speckle interferometry is a relatively new experimental technique which shows promise of elimination to many of the vibration problems experienced thus far in holographic interferometry. The basic method utilizes high resolution photographs of a surface which is illuminated with coherent light (laser). The method of recording displacement information is to photograph a surface in both a reference and deformed configurations which results in a permanently stored whole field record through interference fringes of a deformed surface. Boundary point in-plane displacement measurements are obtained by speckle interferometry and derivatives of the boundary displacements are obtained through shearing interferometry.

Measurements of in plane displacements and the out of plane derivatives are determined by the data analysis of a double exposed photographic record. Values of displacements and derivatives are determined through point-wise and full field Fourier filtering of the film. Point-wise filtering is a method of analysis in which the laser beam is passed through a point on the film plane. As the beam passes through the film the deformed and undeformed speckles produce a complex diffraction pattern which causes an interference effect on a viewing

screen. A diffraction halo modulated by light and dark bars of light is produced where the distance between the bars is inversely proportional to the distance between the undeformed and deformed speckle on the film plane. A normal to the light and dark bar pattern indicates the direction of displacement of the speckle. Displacements are thus obtained at a point and each point on the film is analyzed. Whole field Fourier filtering is used to obtain the derivatives. In this form of data analysis, an interference fringe is the locus of points of constant values of the derivative. Thus, in general, a photographic record of a double exposed laser speckle interferogram contains both displacement and derivative information. Each method of data analysis will be discussed and illustrated by an engineering example. Also, the results imply the utilization of a computer based data analysis system which will also be discussed in Chapter IV.

2.2 General Theory of Fringe Formation

This section presents the general theory of shearing speckle interferometry. A schematic diagram of the experimental apparatus for shearing speckle interferometry is shown in Figure 2-1. The optical wedge in the system shifts the focused image in the direction of the shear. Thus, a point p is imaged at (x,y) and $(x+\delta x,y+\delta y)$ in the film plane, and a neighboring point p_1 is also imaged at (x,y) in the film plane. In order to obtain fringe data, a double exposure technique is used, where a photograph is taken of the body in some reference configuration. After deformation, another exposure is recorded on the same film.

With the body in the reference configuration, the light

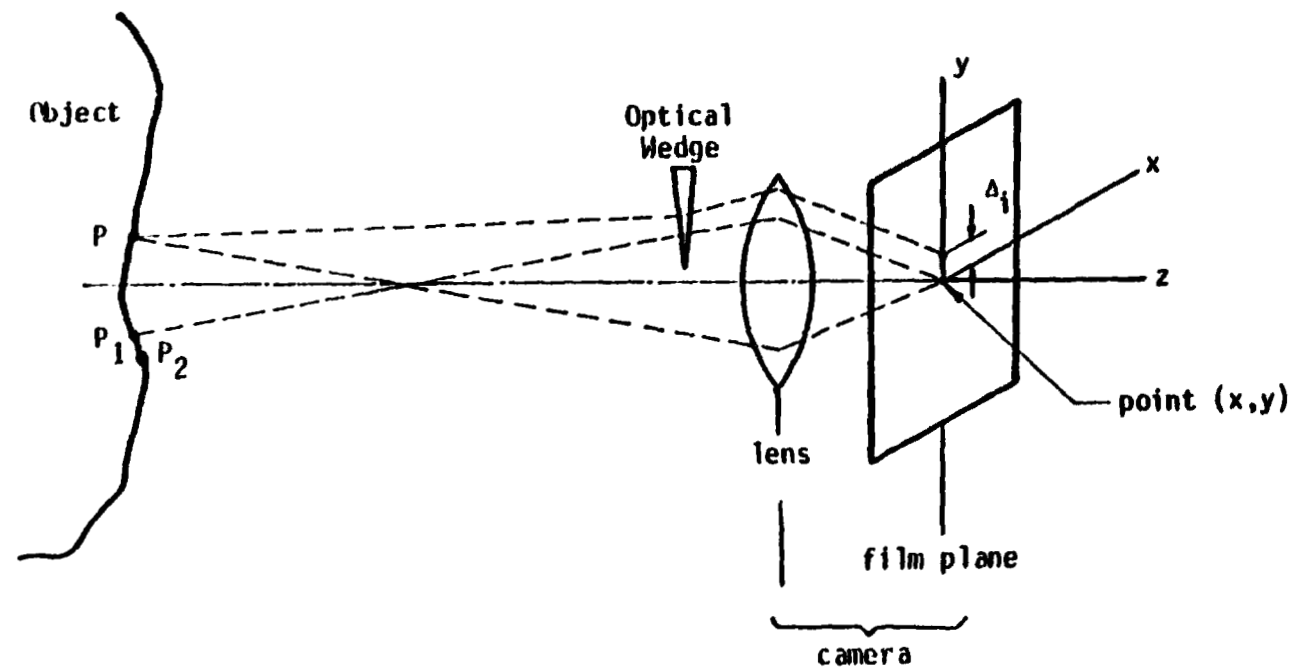


Figure 2-1. Shearing Speckle Interferometry

amplitudes at the film plane for both points p and p_1 can be described in the following manner

$$\begin{aligned} E_p &= \bar{a}_p(x,y) \exp[i\theta_p(x,y)] \\ E_{p_1} &= \bar{a}_{p_1}(x,y) \exp[i\theta_{p_1}(x,y)] \end{aligned} \quad (2-1)$$

where $a(x,y)$ is the amplitude modulus and $\theta(x,y)$ is the phase and both are, in general, functions of the coordinates of the film plane.

The total intensity for the first exposure can be written as

$$I_1 = (E_p + E_{p_1}) \cdot (E_p^* + E_{p_1}^*)$$

where E_p^* and $E_{p_1}^*$ denote the complex conjugate of the light amplitudes, or

$$I_1 = a_p^2(x,y) + a_{p_1}^2(x,y) + 2a_p(x,y) a_{p_1}(x,y) \cos \phi(x,y) \quad (2-2)$$

where

$$\phi(x,y) = \theta_p(x,y) - \theta_{p_1}(x,y)$$

If the body is deformed and the points p and p_1 are displaced to points p' and p'_1 , then the image of point p on the film plane will be shifted to new coordinates x' and y' . The light amplitudes in the deformed configuration can be written in the following form

$$\begin{aligned} E_{p'} &= \bar{a}_{p'}(x',y') \exp[i\{\theta_p(x',y') + \Delta\theta_p\}] \\ E_{p'_2} &= \bar{a}_{p'_2}(x',y') \exp[i\{\theta_{p_2}(x',y') + \Delta\theta_{p_2}\}] \end{aligned} \quad (2-3)$$

$\Delta\theta_p$ and $\Delta\theta_{p_2}$ account for the phase change in each field due to motion of the object relative to the illumination field. The total intensity for the second exposure is

$$I_2 = (E_{p'} + E_{p'_2}) \cdot (E_{p'}^* + E_{p'_2}^*)$$

or

$$I_2 = a_p^2(x', y') + a_{p_2}^2(x', y') + 2 a_p(x', y') a_{p_2}(x', y') \cos[\psi(x', y') + \Delta\phi] \quad (2-4)$$

where

$$\psi(x', y') = \theta_p(x', y') - \theta_{p_2}(x', y')$$

and

$$\Delta\phi = \Delta\theta_p - \Delta\theta_{p_2}$$

So the total intensity expression for both exposures is

$$I_{TOTAL} = I_1 + I_2 = a_p^2(x, y) + a_{p_1}^2(x, y) + 2 a_p(x, y) a_{p_1}(x, y) \cos\phi(x, y) + a_p^2(x', y') + a_{p_2}^2(x', y') + 2 a_p(x', y') a_{p_2}(x', y') \cos[\psi(x', y') + \Delta\phi] \quad (2-5)$$

Let the displacement vector \vec{pp}' be written in the following manner (see Figure 2-2).

$$\vec{pp}' \equiv \vec{U}_p = u_p \vec{e}_x + v_p \vec{e}_y + w_p \vec{e}_z$$

then the displacement vector in the film plane can be written as

$$[\vec{pp}'(x, y)]_{FILM} \equiv \vec{U}_{p_f} = u_{p_f} \vec{e}_x + v_{p_f} \vec{e}_y = M(u_p \vec{e}_x + v_p \vec{e}_y)$$

where M = magnification of camera, typically $M < 1$ and $u_{p_f} = M u_p$,

$$v_{p_f} = M v_p$$

The coordinates at the film plane for the second exposure are $x' = x + u_f$ and $y' = y + v_f$. Now the expression for the total intensity, Equation (2-5), can be written in the following form

$$\begin{aligned}
I_{\text{TOTAL}} = & a_p^2(x,y) + a_{p_1}^2(x,y) + 2a_p(x,y)a_{p_1}(x,y)\cos \phi(x,y) \\
& + a_p^2(x+u_{p_f},y+v_{p_f}) + a_{p_2}^2(x+u_{p_f},y+v_{p_f}) \\
& + 2a_p(x+u_{p_f},y+v_{p_f})a_{p_2}(x+u_{p_f},y+v_{p_f})\cos[\psi(x+u_{p_f},y+v_{p_f}) \\
& + \Delta \phi] \quad (2-6)
\end{aligned}$$

Interference fringes are obtained by taking optically the Fourier transform of the amplitude transmission function of the transparency. This can be done by several methods depending on the data analysis. The amplitude transmission function $g(x,y)$ is linear for the ranges of interest and can be expressed as

$$g(x,y) = a + b I_{\text{TOTAL}} \quad (2-7)$$

where a and b are constants.

Substituting the expression for I_{TOTAL} from Equation (2-6) into Equation (2-7) an expression for the amplitude transmission function is obtained as

$$\begin{aligned}
g(x,y) = & a + b \{ a_p^2(x,y) + a_{p_1}^2(x,y) + 2a_p(x,y)a_{p_1}(x,y)\cos \phi(x,y) \\
& + a_p^2(x+u_{p_f},y+v_{p_f}) + a_{p_2}^2(x+u_{p_f},y+v_{p_f}) \\
& + 2a_p(x+u_{p_f},y+v_{p_f})a_{p_2}(x+u_{p_f},y+v_{p_f})\cos[\psi(x+u_{p_f},y+v_{p_f}) \\
& + \Delta \phi] \} \quad (2-8)
\end{aligned}$$

The procedure developed by [6] is used to express the light amplitude $G(\omega_1, \omega_2)$ in the Fourier transform plane (Figure 2-3) which is proportional to the Fourier transform of $g(x,y)$ times a quadratic phase factor, i.e.

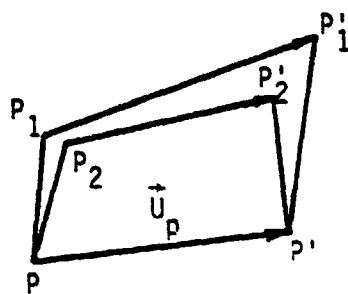


Figure 2-2. Displacement Vectors

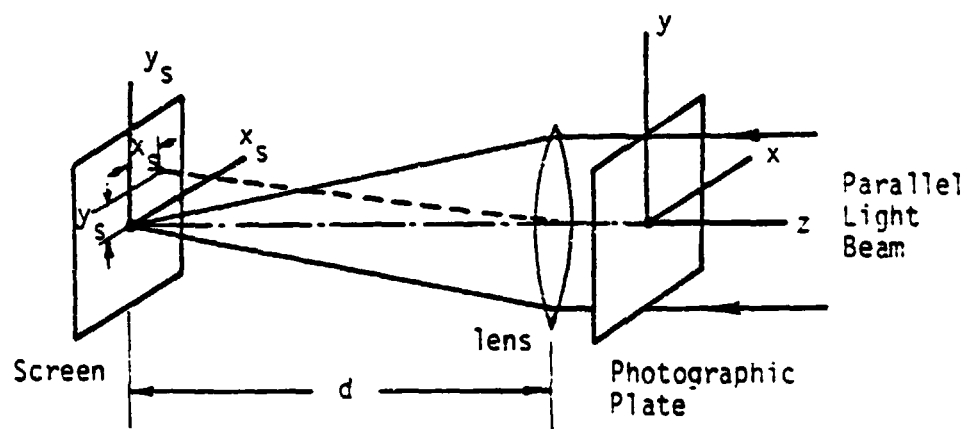


Figure 2-3. Arrangement For Optical Fourier Transform

$$G(\omega_1, \omega_2) = \exp\left[-\frac{id(\omega_1^2 + \omega_2^2)}{2k}\right] F[g(x, y)] \quad (2-9)$$

$F[g(x, y)]$ denotes the Fourier transform of the function $g(x, y)$,

rather

$$F[g(x, y)] = \iint_{-\infty}^{\infty} g(x, y) \exp[-i(\omega_1 x + \omega_2 y)] dx dy$$

and d is the distance between the transparency and the screen. In the transform plane, the vectorial spatial-frequency variable is defined as

$$\vec{\omega} = \omega_1 \vec{e}_{x_s} + \omega_2 \vec{e}_{y_s} ;$$

$$\omega_1 = \frac{kx_s}{d} \quad (2-10)$$

$$\omega_2 = \frac{ky_s}{d}$$

The coordinates in the transform plane are denoted as (x_s, y_s) and the constant $k = \frac{2\pi}{\lambda}$, where λ is the wavelength of the light.

Substituting $g(x, y)$ from Equation (2-7) into Equation (2-9) yields

$$\begin{aligned} G(\omega_1, \omega_2) &= \exp\left[-\frac{id(\omega_1^2 + \omega_2^2)}{2k}\right] F[a + b I_{\text{TOTAL}}] \\ &= \exp\left[-\frac{id(\omega_1^2 + \omega_2^2)}{2k}\right] \{a\delta(\omega_1, \omega_2) + b F[I_{\text{TOTAL}}]\} \end{aligned}$$

where $\delta(\omega_1, \omega_2)$ is the delta function defined as

$$\delta(\omega_1, \omega_2) = \iint_{-\infty}^{\infty} \exp[-i(\omega_1 x + \omega_2 y)] dx dy$$

The delta function represents the (idealized) point focus of the illuminating beam. It contributes to the amplitude $G(\omega_1, \omega_2)$ only at the center ($\omega_1 = \omega_2 = 0$); in practice it is a small area around this point. Outside this small area the intensity $|G(\omega_1, \omega_2)|^2$ in the transform plane is

$$\begin{aligned} I(\omega_1, \omega_2) &= |G(\omega_1, \omega_2)|^2 = G(\omega_1, \omega_2) G^*(\omega_1, \omega_2) \\ &= b^2 |F[I_{\text{TOTAL}}]|^2 \end{aligned} \quad (2-11)$$

Using the identity

$$\cos(\psi + \Delta \phi) = \cos \psi \cos \Delta \phi - \sin \psi \sin \Delta \phi$$

in the expression of I_{TOTAL} , Equation (2-6), the Fourier transform of I_{TOTAL} can be written as

$$\begin{aligned} F[I_{\text{TOTAL}}] &= A_p(\vec{\omega}) * A_p(\vec{\omega}) \{1 + \exp[i(\vec{\omega} \cdot \vec{U}_{p_f})]\} + A_{p_1}(\vec{\omega}) * A_{p_1}(\vec{\omega}) \\ &\quad + A_{p_2}(\vec{\omega}) * A_{p_2}(\vec{\omega}) \exp[i(\vec{\omega} \cdot \vec{U}_{p_f})] + 2A_p(\vec{\omega}) * A_{p_1}(\vec{\omega}) * C(\vec{\omega}) \\ &\quad + 2A_{p_2}(\vec{\omega}) * A_{p_2}(\vec{\omega}) * C(\vec{\omega}) \exp[i(\vec{\omega} \cdot \vec{U}_{p_f})] \cos \Delta \phi \\ &\quad - 2A_p(\vec{\omega}) * A_{p_2}(\vec{\omega}) * S(\vec{\omega}) \exp[i(\vec{\omega} \cdot \vec{U}_{p_f})] \sin \Delta \phi \end{aligned} \quad (2-12)$$

$F[]$ indicates the two-dimensional Fourier transform with respect to the variable $\vec{\omega}$; the capital letters A_p , A_{p_1} and A_{p_2} are the Fourier transforms of the functions a_p , a_{p_1} and a_{p_2} respectively; $*$ denotes the convolution integral (such as)

$$A_p(\vec{\omega}) * A_{p_1}(\vec{\omega}) * C(\vec{\omega}) = F[a_p(x, y) a_{p_1}(x, y) \cos \psi(x, y)]$$

and

$$C(\vec{\omega}) = F[\cos \psi(x, y)]$$

$$S(\vec{\omega}) = F[\sin \psi(x, y)]$$

In writing Equation (2-12), shift theorem has been used (such as)

$$F[a_p^2(x+u_{p_f}, y+v_{p_f})] = \exp[i(\vec{\omega} \cdot \vec{U}_{p_f})] F[a_p^2(x, y)]$$

and the convolution theorem to describe the transform of the various products in Equation (2-6). Also \vec{U}_{p_f} has been assumed to be a slow varying function of x and y .

Several experimental examples will be discussed to illustrate the validity and the data analysis of Equation (2-12).

2.3 Experimental Verification of the General Shearing Speckle

Interferometry Equations

The experimental problem chosen to verify the results of the general theory is the flexure of a rectangular beam by a terminal end load. Let the beam have the end $x = l$ fixed and the end $x = 0$ have a distribution of forces statically equivalent to a single force W_y directed along the negative y -axis as shown in Figure 2-4. Take the x -axis along the center line of the beam, and y -axis as orthogonal

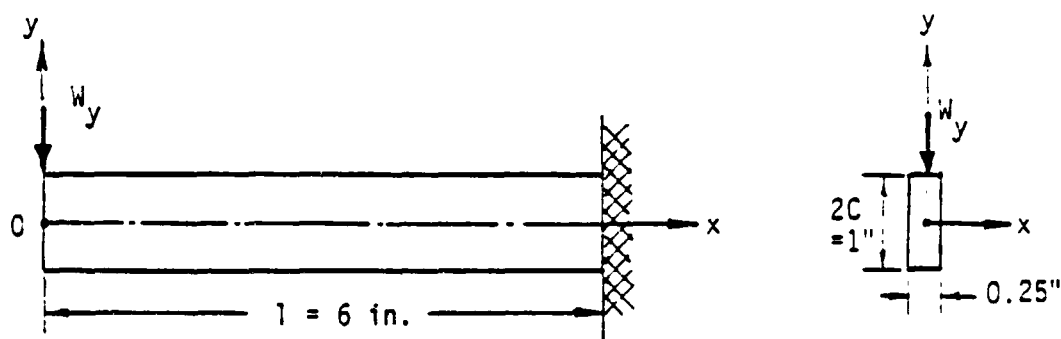


Figure 2-4. Rectangular Plexiglas Beam with a Transverse End Load

intersecting at the centroid of the free end. Material for the beam was plexiglas with $E = 4.56 \times 10^5$ psi and $\nu = 0.37$. The transverse end load was governed by the displacement of the free end δ because of the constraints on the pointwise filtering of the experimental data. For completeness of the discussion the theoretical displacement components from the stress function solution for this problem will be listed here.

$$u = \frac{3\delta}{13} \left[\frac{1}{2}x^2y - \frac{1}{6}(\nu+2)y^3 + (c^2(1+\nu) - \frac{1}{2})y \right] \quad (2-13)$$

$$v = \frac{3\delta}{13} \left[-\frac{\nu}{2}xy^2 - \frac{1}{6}x^3 + \frac{1}{2}x^2y - \frac{1}{3}y^3 \right] \quad (2-14)$$

Example 1 - In-plane Displacement

The geometrical configuration for in-plane measurements is shown in Figure 2-5. A point P on the surface of the beam is illuminated by a laser located at position S. The surface is imaged by a camera located at position D with film plane coordinates parallel to the x,y plane. For this example, the optical wedge is removed, thus, the lateral shear is zero, which yields, $A_{p_1} = A_{p_2} = 0$ in Equation (2-12). Furthermore, since only a small area is illuminated in the film plane (see Figure 2-6), the displacement in the neighborhood is assured constant, the total intensity, Equation (2-11), reduces to the following form

$$I(\omega_1, \omega_2) = 2b^2 |A_p(\vec{\omega}) \star A_p(\vec{\omega})|^2 [1 + \cos(\vec{\omega} \cdot \vec{U}_{p_f})] \quad (2-15)$$

Equation (2-15) agrees with the simple case considered in Reference [5].

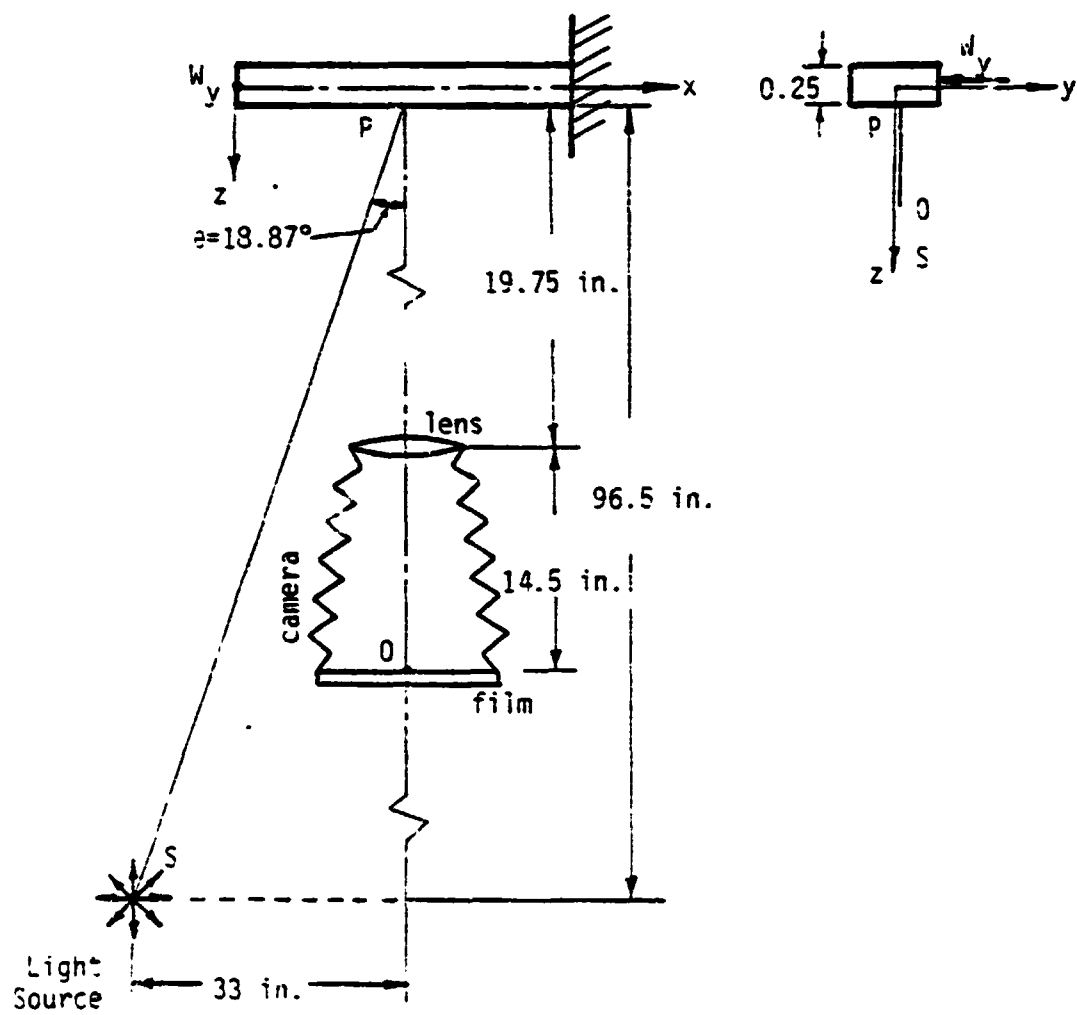


Figure 2-5. Geometrical Configuration For The First Experimental Example

Only terms that relate to the interference effects in Equation (2-15) will be considered in the data analysis. Interference fringes will be defined when $I(\omega_1, \omega_2) = 0$ or $[1 + \cos \vec{\omega} \cdot \vec{U}_{p_f}] = 0$. Fringes are determined by the technique of pointwise filtering as illustrated in Figure 2-6. For the small region of illumination of the transparency in the neighborhood of P, the displacement is assumed constant and fringes are formed when

$$\vec{\omega} \cdot \vec{U}_{p_f} = (2n-1)\pi \quad n = 1, 2, 3, \dots$$

For most problems of interest only the first fringe is observed, therefore,

$$\vec{\omega} \cdot \vec{U}_{p_f} = \pi$$

Displacement components are obtained from the following expression

$$\frac{2\pi}{\lambda} \left(\frac{x_s}{d} \hat{e}_{x_s} + \frac{y_s}{d} \hat{e}_{y_s} \right) \cdot (u_{p_f} \hat{e}_x + v_{p_f} \hat{e}_y) = \pi$$

Usually

$$\hat{e}_{x_s} = \hat{e}_x, \hat{e}_{y_s} = \hat{e}_y,$$

therefore

$$x_s u_{p_f} + y_s v_{p_f} = \frac{\lambda d}{2} \quad (2-16)$$

The schematic for determining the components u_{p_f} and v_{p_f} from Equation (2-16) is illustrated in Figure 2-7 by measuring the distances x_s and y_s between the center and points of intersection of the first fringe with the x and y axes respectively.

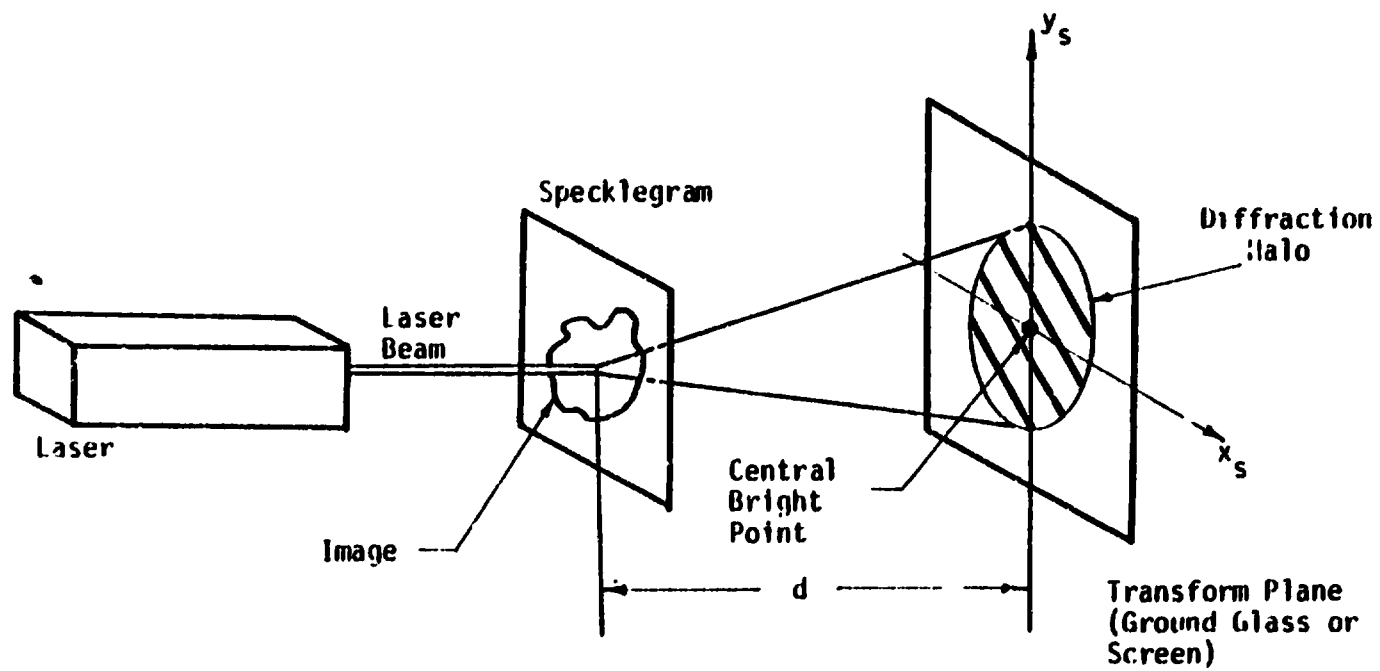


Figure 2-6. Data Analysis for Point-Wise Filtering in In-plane Measurements

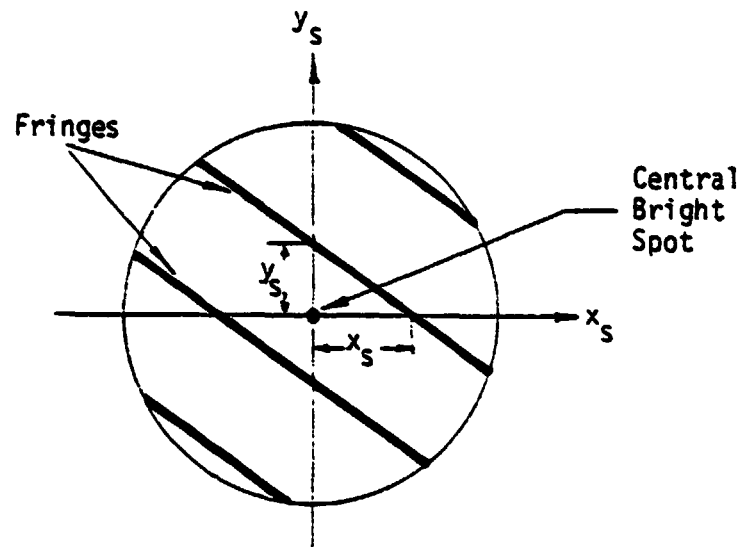


Figure 2-7. Schematic for Determining the In-plane Displacements Components

The displacement components for the film plane are then given by

$$u_{p_f} = \frac{\lambda d}{2x_s}$$

and

$$v_{p_f} = \frac{\lambda d}{2y_s}$$

Figure 2-8 is a graph of the results of in-plane measurements for this experimental example. As can be observed, the experimental results agree very well with the theory. In addition, this method of data analysis is amenable to automated data analysis as will be described later in Chapter IV.

Example 2 - Shearing Speckle Measurements of Displacement Derivatives

The experimental arrangement for the example problem used to illustrate the shearing speckle measurements is shown in Figure 2-9. An optical wedge is placed in front of the camera at 0. Also for

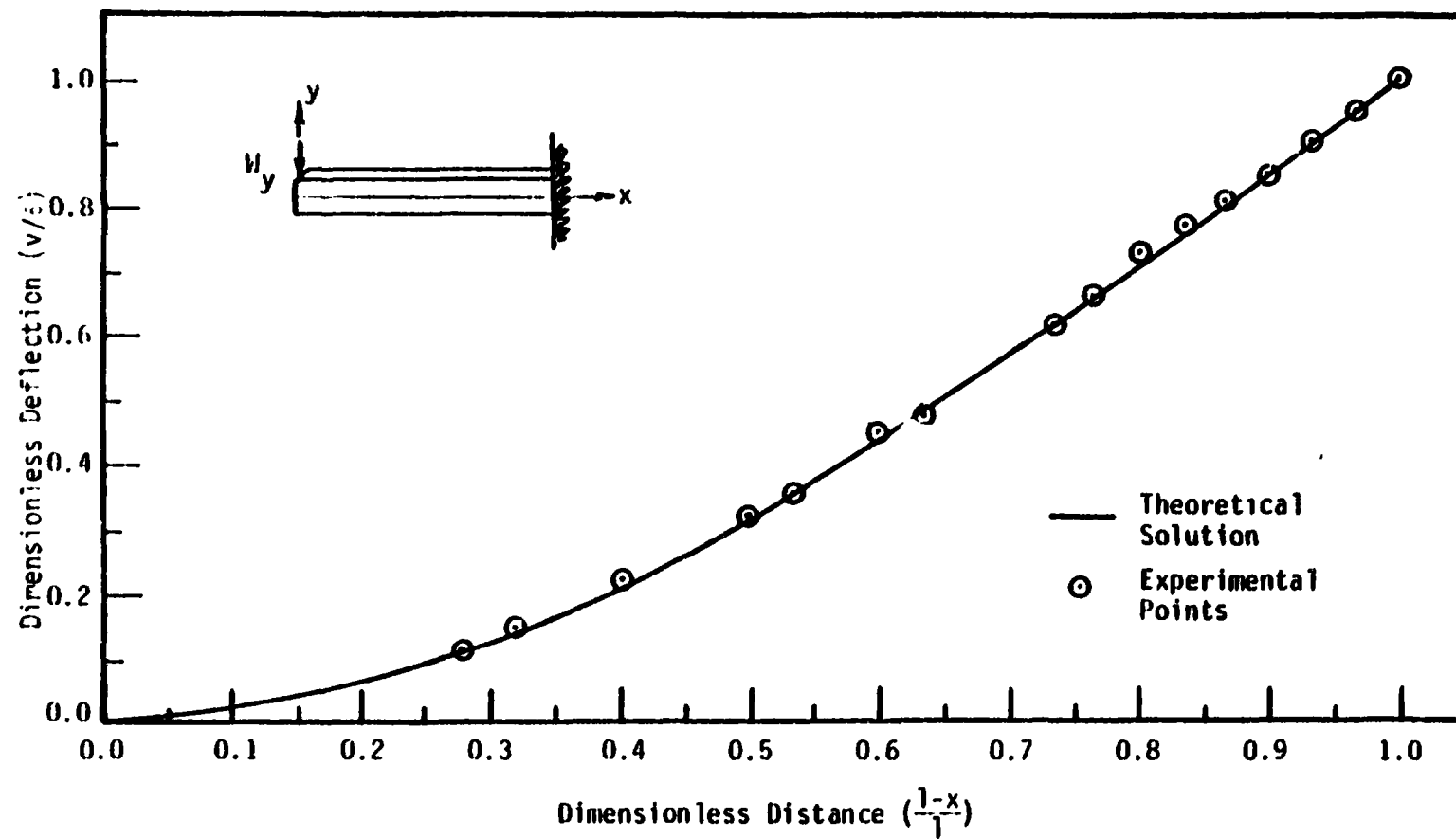


Figure 2-8. Comparison of Theoretical and Experimental Values of Beam Deflection Along the x -axis

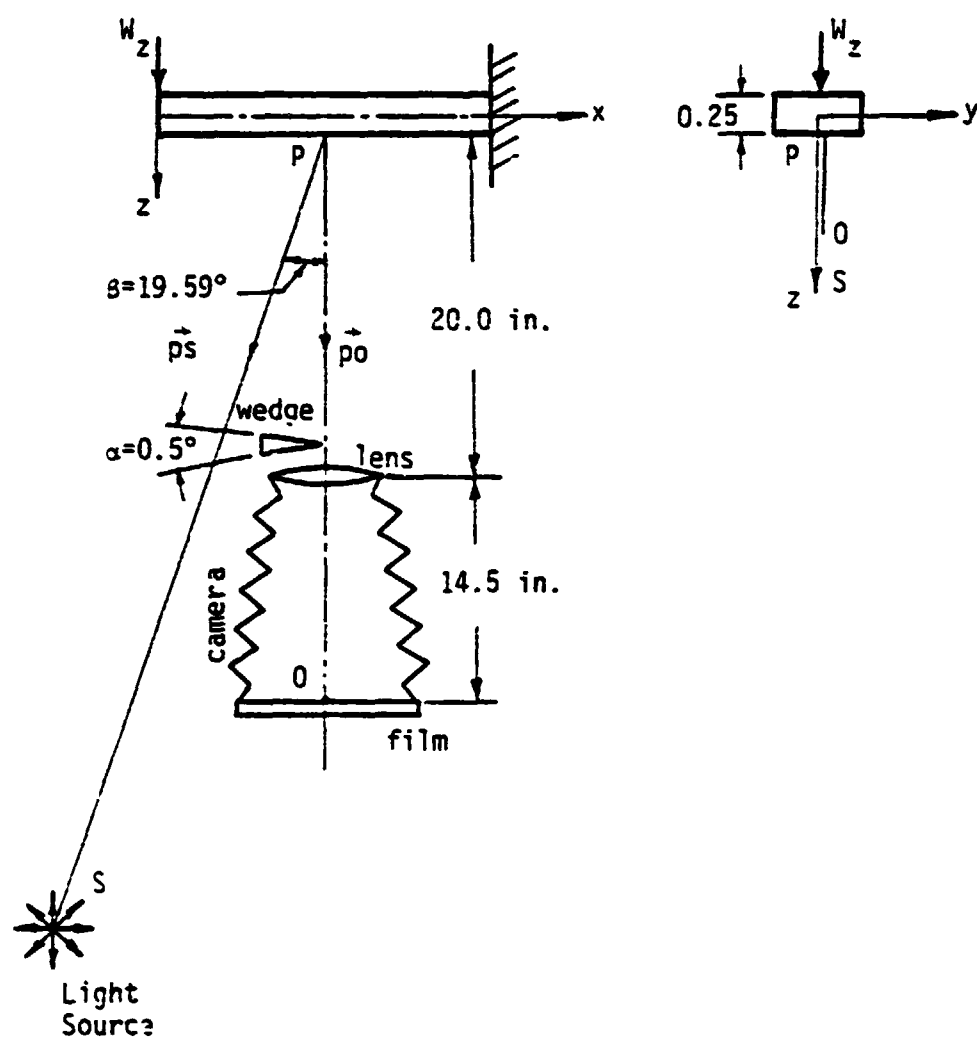


Figure 2-9. Geometrical Configuration For The Second Experimental Example

this example $u_p = v_p = 0$ while $w_p \neq 0$ and $A_p = A_{p_1} = A_{p_2} \equiv A$ since shearing speckle interferometry is a phase phenomenon. Equation (2-12) reduces to

$$F [I_{TOTAL}] = 4 A(\vec{\omega})_* A(\vec{\omega}) + 2A(\vec{\omega})_* A(\vec{\omega})_* C(\vec{\omega}) (1 + \cos \Delta\phi) - 2 A(\vec{\omega})_* A(\vec{\omega})_* S(\vec{\omega}) \sin \Delta\phi \quad (2-17)$$

Again Equation (2-17) agrees with Reference [5].

Derivative information is related to the minimum of $I(\omega_1, \omega_2)$, Equation (2-11), which will be minimum - upon substitution of Equation (2-17)-when $(1 + \cos \Delta\phi)$ and $\sin \Delta\phi$ are both zero. Therefore, $\Delta\phi = (2n-1)\pi$ will define a fringe. The phase change $\Delta\phi$ can be written in the following form [1]

$$\Delta\phi = \frac{2\pi}{\lambda} [\vec{p}s + \vec{p}o] \cdot (\vec{p}_2 \vec{p}_2' - \vec{p} \vec{p}') \quad (2-18)$$

$$\text{where } \vec{p}s = \begin{Bmatrix} 1_s \\ m_s \\ n_s \end{Bmatrix} \quad \text{and} \quad \vec{p}o = \begin{Bmatrix} 1_o \\ m_o \\ n_o \end{Bmatrix} \quad \text{are unit vectors}$$

representing the directions from point P or the object to the light source and camera respectively. Further, as shown in Reference [5], Equation (2-18) can be written in the following form

$$\begin{aligned} \Delta\phi = \frac{2\pi}{\lambda} & \left[(1_s + 1_o) \left(\frac{\partial u}{\partial x} \Delta x + \frac{\partial u}{\partial y} \Delta y + \frac{\partial u}{\partial z} \Delta z \right) \right. \\ & + (m_s + m_o) \left(\frac{\partial v}{\partial x} \Delta x + \frac{\partial v}{\partial y} \Delta y + \frac{\partial v}{\partial z} \Delta z \right) \\ & \left. + (n_s + n_o) \left(\frac{\partial w}{\partial x} \Delta x + \frac{\partial w}{\partial y} \Delta y + \frac{\partial w}{\partial z} \Delta z \right) \right] \quad (2-19) \end{aligned}$$

Fringe order can be determined from the following expression

$$\begin{aligned}
 (n - \frac{1}{2})\lambda = & \left[(l_s + l_o) \left(\frac{\partial u}{\partial x} \Delta x + \frac{\partial u}{\partial y} \Delta y + \frac{\partial u}{\partial z} \Delta z \right) \right. \\
 & + (m_s + m_o) \left(\frac{\partial v}{\partial x} \Delta x + \frac{\partial v}{\partial y} \Delta y + \frac{\partial v}{\partial z} \Delta z \right) \\
 & \left. + (n_s + n_o) \left(\frac{\partial w}{\partial x} \Delta x + \frac{\partial w}{\partial y} \Delta y + \frac{\partial w}{\partial z} \Delta z \right) \right] \quad (2-20)
 \end{aligned}$$

Fringe order data for the shearing speckle is obtained by taking optically the Fourier transform of the double exposed transparency as shown in Figure 2-3. Data for this example is the following

$$l_o = m_o = 0, n_o = 1$$

and

$$l_s = -\sin\beta, m_s = 0, n_s = \cos\beta \text{ where } \beta = 19.59^\circ$$

For a shear of value $\Delta x = 0.0899$ in. in the negative x direction only and assuming that the only non-zero displacement component is w_p , then the fringe order n is expressed as

$$n = \left[-\sin\beta \frac{\partial u}{\partial x} + (1 + \cos\beta) \frac{\partial w}{\partial x} \right] \frac{\Delta x}{\lambda} + 0.5 \quad (2-21)$$

where λ is the wavelength of the laser light used = 6328 Å.

Comparison of the theoretical and experimental results for the case of free end deflection of 0.005 inches are shown in Figure 2-10.

As in the in-plane example the results are in good agreement.

Both experimental examples illustrate the combined effects of displacement measurements in laser speckle interferometry. Also the measurements are not constrained to vibration isolation environments as in holography, therefore, measurements on prototype systems are possible. Possibly one of the most important advantages of the speckle technique is the ability to automate the data analysis by a

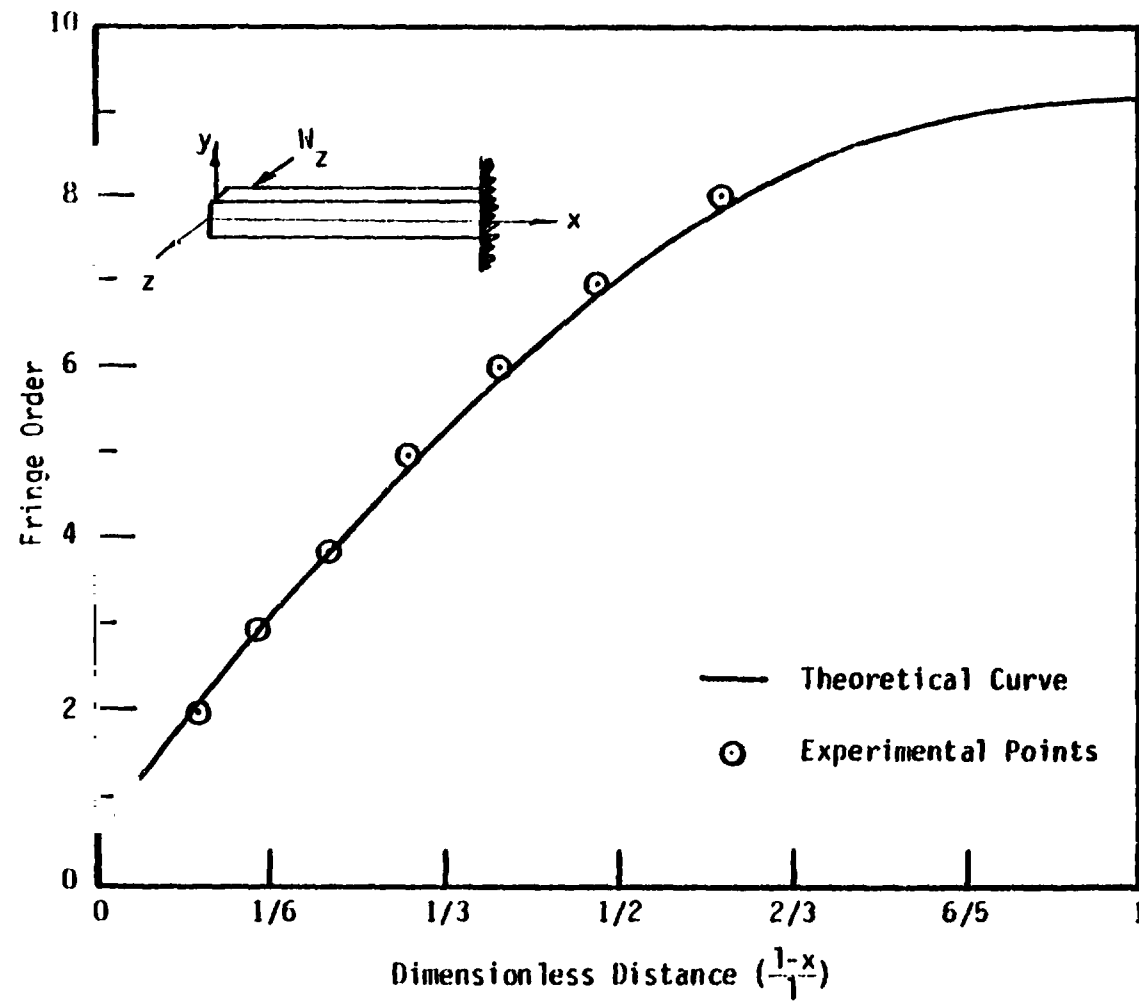


Figure 2-10. Comparison of Theory and Experiment Along the x -axis for the Second Experimental Example

computer based system, in particular, the in-plane measurements.

III. THE BOUNDARY-INTEGRAL EQUATION METHOD FOR ELASTICITY PROBLEMS

3.1 Brief Introduction

The boundary-integral equation (BIE) method, with its origin in classical elasticity, has only in recent years been developed and applied to solve significant problems in solid mechanics. The initial applications of the BIE method to solid mechanics problems have taken place within the past twelve years [12]. Since then the potential of this powerful technique as a basic tool for solving engineering problems has been recognized and the number of problem areas in solid mechanics that have been solved using this numerical technique is large [30].

The BIE technique is based on the use of an integral constraint equation which relates boundary displacements and corresponding boundary tractions. One advantage of this method is that numerical discretization occurs only on the boundary of the body being analyzed, which reduces the dimension of the problem by one. No approximation to the field equations are necessary as all approximations are made at the boundary, hence a high resolution for the interior solution may be obtained at any desired location. This is particularly important for the analysis of problems with significant stress risers. The BIE method is also independent of boundary shape and connectivity of the body.

Following this section is an extensive review and a thorough discussion of the mathematical formulation of the BIE method as

applied to elastostatics. Formulation of the numerical solution technique for plane problems is discussed in Section 3.3.

3.2 Mathematical Formulation of the BIE Method

A comprehensive review of the mathematical basis and formulation of the BIE technique for two and three dimensional elasticity is essential for conscious and better understanding of this powerful technique and will be documented in this thesis for completeness of the discussion.

This discussion is restricted to the analysis of classical elastostatic problems for which the material may be taken as isotropic and homogenous. The notation used is the usual cartesian tensor notation with implied summation on repeated indices and partial differentiation denoted by the comma-index.

Equilibrium equations can be written as,

$$\sigma_{ij,j} + b_i = 0 \quad (i,j = 1,2,3) \quad (3-1)$$

where b_i is the body force. The stress components σ_{ij} and displacement gradients are related by Hooke's Law

$$\sigma_{ij} = \frac{2\mu}{1-2\nu} \delta_{ij} u_{m,m} + \mu(u_{i,j} + u_{j,i}) \quad (3-2)$$

where μ is the shear modulus of the material and ν is Poisson's ratio. Substitution of Equation (3-2) into Equation (3-1) results in the Navier equations of equilibrium in terms of the displacements

$$\frac{1}{1-2\nu} u_{i,ij} + u_{j,ii} + \frac{1}{\mu} b_j = 0 \quad (3-3)$$

The solution of this differential equation must satisfy appropriate boundary conditions. The displacement boundary value problem assumes knowledge of the displacement on the entire surface S

$$u_i(\underline{x}) = \bar{u}_i(\underline{x}) \quad (3-4)$$

where \underline{x} denotes the orthogonal cartesian coordinates x_1, x_2, x_3 . The \bar{u}_i are the prescribed values of surface displacements. The traction boundary value problem is

$$t_i(\underline{x}) = \sigma_{ij}n_j = \bar{t}_i(\underline{x}) \quad (3-5)$$

where the vector function $\bar{t}_i(\underline{x})$ is prescribed for $\underline{x} \in S$. The unit vector n_j is the outward normal vector for the body R .

The surface tractions and displacements associated with any two solutions to the governing equations of elasticity in a region R can be related through Betti's theorem of elastic reciprocity [31]. Betti's second theorem states that for continuous, finite stresses and zero body force

$$\int_S t_i^1 u_i^2 dS = \int_S t_i^2 u_i^1 dS \quad (3-6)$$

where S is the bounding surface of R .

If body forces are included in the stress field Betti's second theorem can easily be shown to be of the form

$$\int_S t_i^1 u_i^2 dS + \int_R X_i^1 u_i^2 dV = \int_S t_i^2 u_i^1 dS + \int_R X_i^2 u_i^1 dV \quad (3-7)$$

for body force fields X_i^1, X_i^2 which are finite and piecewise continuous in R .

The development of the boundary integral approach proceeds by setting one of the stress states u_i^2 and t_i^2 in Equation (3-6) equal to the displacements u_i^* and tractions t_i^* corresponding to the

fundamental solution to Navier's equations. $u_i^1 \equiv u_i$ and $t_i^1 \equiv t_i$ are displacements and tractions for the other stress state. It has been shown in Reference [32] that the fundamental solution to Navier's equations corresponds to Kelvin's problem. By letting the distance between the field point q with coordinates y_1, y_2 and y_3 and load point p with coordinates x_1, x_2 and x_3 be given by

$$r = [(y_i - x_i)(y_i - x_i)]^{1/2} \quad (3-8)$$

the well known solution [31] to Kelvin's problem of the point load of unit magnitude in each of the x_i directions in an infinite body is

$$i^*(p,q) = \frac{1}{16\pi\mu(1-\nu)} \frac{1}{r} [(3-4\nu)\delta_{ij} + r_{,i}r_{,j}]e_j \quad (3-9)$$

where e_j 's are a set of unit vectors in the x_j directions. In Equation (3-9) and in what follows all differentiations are with respect to the field point q , i.e.,

$$r_{,i} = \frac{\partial r}{\partial y_i} = \frac{1}{r}(y_i - x_i) = -\frac{\partial r}{\partial x_i} \quad (3-10)$$

$$\text{and } \frac{\partial r}{\partial n} = \frac{\partial r}{\partial y_i} n_i = \frac{1}{r}(y_i - x_i)n_i \quad (3-11)$$

where the normal is evaluated at q also. The tractions on an arbitrary surface with outward normal n_j around the point p corresponding to the fundamental solution are given by

$$t_i^*(p,q) = \sigma_{ij}n_j = -\frac{(1-2\nu)}{8\pi(1-\nu)} \frac{1}{r^2} \left[\frac{\partial r}{\partial n}(\delta_{ij} + \frac{3}{1-2\nu} r_{,i}r_{,j}) - n_j r_{,i} + n_i r_{,j} \right] e_j \quad (3-12)$$

From Equations (3-9) and (3-12) second-order tensors can be found

$$\begin{aligned} u_i^* (p,q) &= U_{ji}(p,q) e_j, \\ t_i^* (p,q) &= T_{ji}(p,q) e_j \end{aligned} \quad (3-13)$$

where [13]

$$U_{ji}(p,q) = \frac{1}{16\pi\mu(1-\nu)} \frac{1}{r} \left[(3-4\nu) \delta_{ij} + r_{,i} r_{,j} \right] \quad (3-14)$$

and

$$\begin{aligned} T_{ji}(p,q) &= - \frac{(1-2\nu)}{8\pi(1-\nu)} \frac{1}{r^2} \left[\frac{\partial r}{\partial n} (\delta_{ij} + \frac{3}{1-2\nu} r_{,i} r_{,j}) \right. \\ &\quad \left. - n_j r_{,i} + n_i r_{,j} \right] \end{aligned} \quad (3-15)$$

The first index in $U_{ji}(p,q)$ and $T_{ji}(p,q)$ corresponds to the direction of the point load and the second index refers to the component of the respective displacements and tractions.

For the two dimensional isotropic plane strain case the fundamental tensors are [12]

$$U_{ji}(p,q) = \frac{1}{8\pi\mu(1-\nu)} \left[(3-4\nu) \ln \frac{1}{r} \delta_{ij} + r_{,i} r_{,j} \right] \quad (3-16)$$

and

$$\begin{aligned} T_{ji}(p,q) &= - \frac{(1-2\nu)}{4\pi(1-\nu)} \frac{1}{r} \left[\frac{\partial r}{\partial n} (\delta_{ij} + \frac{2}{1-2\nu} r_{,i} r_{,j}) \right. \\ &\quad \left. - n_j r_{,i} + n_i r_{,j} \right] \end{aligned} \quad (3-17)$$

The case of plane stress can be handled through the use of an effective Poisson's ratio given by $[\nu/(1+\nu)]$.

Due to the singular nature of Kelvin's problem at the point $p(x)$ a small spherical region (circular region for the two-

dimensional case) of radius ϵ denoted R_ϵ surrounding the point p with surface S_ϵ has been deleted (see Figure 3-1). A limit will be taken by diminishing the radius ϵ indefinitely. The external boundary of the region will be taken to be the surface S of the body.

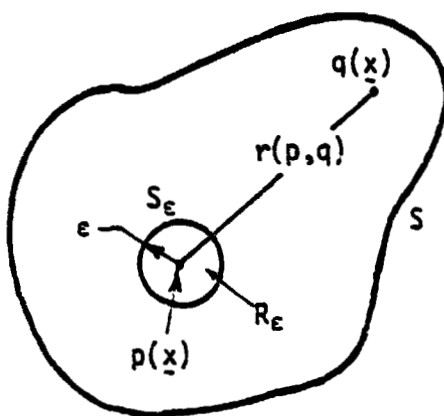


Figure 3-1. Development of Somigliana Identity

Now Equation (3-6) as applied to the region $R - R_\epsilon$ can be rewritten as

$$\int_{S + S_\epsilon} t_i u_i^* dS = \int_{S + S_\epsilon} u_i t_i^* dS \quad (3-18)$$

Noting that on the surface S_ϵ , $\frac{d}{dn} = -\frac{d}{dr}$; also for the deleted region $\epsilon \equiv r$; it is easily verified that the limit

$$\lim_{\epsilon \rightarrow 0} \int_{S_\epsilon} t_i u_i^* dS = 0 \quad (3-19)$$

The second integral in Equation (3-18) over S_ϵ may be written as

$$\begin{aligned} \int_{S_\epsilon} u_i t_i^* dS &= \int_{S_\epsilon} [u_i(Q) - u_i(p)] t_i^*(p, Q) dS(Q) \\ &+ u_i(p) \int_{S_\epsilon} t_i^*(p, Q) dS(Q) \end{aligned} \quad (3-20)$$

where point Q is on the surface S_ϵ and point $p(x)$ is held fixed in the integration. Since the displacements are continuous at $p(x)$ the second integral in Equation (3-20) has zero limit as $\epsilon \rightarrow 0$. And

$$\begin{aligned} \lim_{\epsilon \rightarrow 0} \int_{S_\epsilon} u_i t_i^* dS &= \lim_{\epsilon \rightarrow 0} \{u_i(p) \int_{S_\epsilon} t_i^* dS\} \\ &= u_i(p) \delta_{ij} e_j = u_j(p) e_j \end{aligned} \quad (3-21)$$

Substitution of the above results into Equation (3-18) and taking the limits as $\epsilon \rightarrow 0$

$$\int_S t_i u_i^* dS = u_j(p) e_j + \int_S u_i t_i^* dS \quad (3-22)$$

Making the substitution that $u_i^* = U_{ji} e_j$, $t_i^* = T_{ji} e_j$ and taking each of the e_j terms as independent the following vector equation is obtained

$$u_j(p) = \int_S t_i(Q) U_{ji}(p, Q) dS(Q) - \int_S u_i(Q) T_{ji}(p, Q) dS(Q) \quad (3-23)$$

where $u_j(p)$ is the displacement vector at an arbitrary internal point p , and the vectors $u_i(Q)$ and $t_i(Q)$ are the displacement and traction vectors at a surface point Q . Equation (3-23) is the well known Somigliana identity for the interior displacement field generated by a full set of known boundary displacements and

boundary tractions (cf. Reference 31, p. 245).

The interior stress state may be generated by differentiation of Equation (3-23) with respect to the load point $p(x)$ and using the constitutive equation, Equation (3-2), and is given by

$$\sigma_{ij}(p) = \int_S t_k(Q) D_{kij}(p, Q) dS(Q) - \int_S u_k(Q) S_{kij}(p, Q) dS(Q) \quad (3-24)$$

The third order tensor kernels D_{kij} and S_{kij} are given by [32]

$$D_{kij}(p, Q) = \frac{1}{4\alpha\pi(1-\nu)} \left(\frac{1}{r^\alpha}\right) \left[(1-2\nu)(\delta_{ki}r_{,j} + \delta_{kj}r_{,i} - \delta_{ij}r_{,k}) + \beta r_{,i}r_{,j}r_{,k} \right] \quad (3-25)$$

$$S_{kij}(p, Q) = \frac{\nu}{2\alpha\pi(1-\nu)} \left(\frac{1}{r^\beta}\right) \left\{ \beta \frac{dr}{dn} \left[(1-2\nu) \delta_{ij}r_{,k} + \nu(\delta_{ik}r_{,j} + \delta_{jk}r_{,i}) - \gamma r_{,i}r_{,j}r_{,k} \right] + \beta \nu(n_i r_{,j}r_{,k} + n_j r_{,i}r_{,k}) + (1-2\nu)(\beta n_k r_{,i}r_{,j} + n_j \delta_{ik} + n_i \delta_{jk}) - (1-4\nu)n_k \delta_{ij} \right\} \quad (3-26)$$

In the above two equations $\alpha=1,2$; $\beta=2,3$; $\gamma=4,5$ for two and three dimension problems respectively. The comma-differentiation is to be taken with respect to the coordinates of the point of integration, and since the stresses are found by taking derivatives of Equation (3-23) with respect to the solution point $p(x)$, a change of sign arises from the identity $(\frac{\partial r}{\partial x_i} = -\frac{\partial r}{\partial y_i})$. The normal is evaluated at $Q(x)$.

While Equation (3-23) represents the interior solution, its use

requires the simultaneous specification of all components of both the displacement vector and traction vector for all the boundary points. These six boundary conditions are twice as many as required by the uniqueness theorem.

The essence of the boundary-integral equation technique is to allow the internal point $p(\underline{x})$ to pass to an arbitrary surface point $P(\underline{x})$, yielding a set of integral equations which can be solved for the unknown boundary tractions and displacements in a well-posed boundary value problem. It should be noted that the kernels of the integrals in Equation (3-23) exhibit singularities as $p(\underline{x})$ approaches the surface S , so that the resulting set of integral equations will be singular.

The limiting procedure for $p(\underline{x})$ approaching a point $P(\underline{x})$ on a smooth contour (two-dimensional case) is illustrated schematically in Figure 3-2a. This smooth contour permits the construction of a short, straight line centered at $P(\underline{x})$ with length 2ϵ . The internal point $p(\underline{x})$ is placed at the boundary and the boundary is augmented as shown in Figure 3-2b. Point $p(\underline{x})$ is assumed to be at the center of the circle and afterwards the radius ϵ is reduced to zero. The point will then become a boundary point. The results of this limit for the individual terms of Equation (3-23) are as follows

$$\begin{aligned} \lim_{p(\underline{x}) \rightarrow P(\underline{x})} u_j(p) &= u_j(P) \\ \lim_{p(\underline{x}) \rightarrow P(\underline{x})} \int_S u_i(Q) T_{ji}(p, Q) dS(Q) &= \end{aligned} \quad (3-27)$$

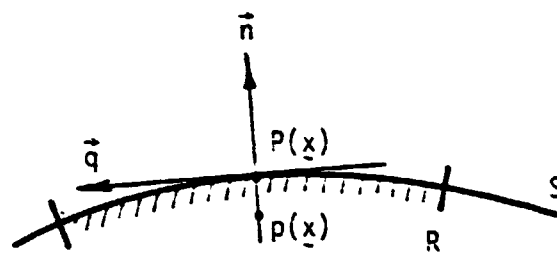


Figure 3-2a

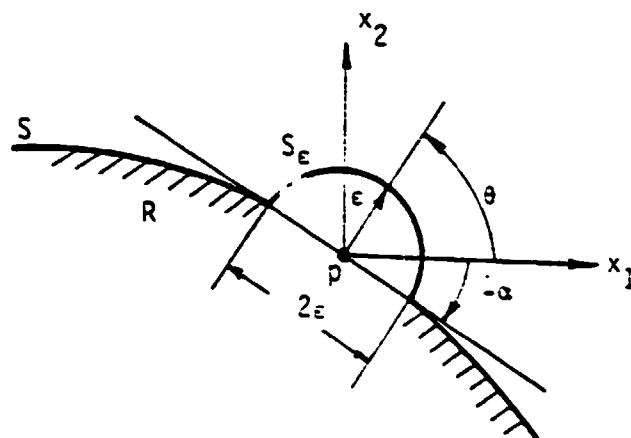


Figure 3-2b

Figure 3-2. Limiting Procedure for p
Approaching Smooth Boundary

$$\lim_{\epsilon \rightarrow 0} \int_{S-S_\epsilon} u_i T_{ji} dS + \lim_{\epsilon \rightarrow 0} \int_{S_\epsilon} u_i T_{ji} dS$$

For simplicity the second limit on the right hand side will be called I;

$$I = \lim_{\epsilon \rightarrow 0} \int_{S_\epsilon} u_i T_{ji} dS = \lim_{\epsilon \rightarrow 0} \left\{ - \int_{S_\epsilon} u_i \left[\frac{dr}{dn} \{ (1-2\nu) \delta_{ij} + 2 \frac{\partial r}{\partial x_i} \frac{\partial r}{\partial x_j} \} \right. \right. \\ \left. \left. + (1-2\nu) \left\{ \frac{\partial r}{\partial x_i} n_j - \frac{\partial r}{\partial x_j} n_i \right\} \right] \frac{1}{4\pi(1-\nu)r} dS \right\}$$

knowing that $\epsilon \equiv r$ and using a polar system of coordinates for simplicity, the second term in the above limit will disappear as,

$$\frac{\partial r}{\partial x_i} n_j - \frac{\partial r}{\partial x_j} n_i = - \frac{\partial r}{\partial x_i} \frac{\partial r}{\partial x_j} + \frac{\partial r}{\partial x_j} \frac{\partial r}{\partial x_i} \equiv 0$$

Since $\frac{\partial r}{\partial n} = 1$ and $dS = r d\theta$ where the range on θ is $-\alpha \leq \theta \leq \pi - \alpha$ then,

$$I = \lim_{\epsilon \rightarrow 0} \left\{ - \int_{S_\epsilon} u_i \left[(1-2\nu) \delta_{ij} + 2 \frac{\partial r}{\partial x_i} \frac{\partial r}{\partial x_j} \right] \frac{d\theta}{4\pi(1-\nu)} \right\}$$

This can be expanded and expressed in terms of θ only, for instance when $j = 1$

$$I = \lim_{\epsilon \rightarrow 0} \left\{ - \int_{\theta=-\alpha}^{\pi-\alpha} [u_1(1-2\nu) + 2u_1 \cos^2 \theta + 2u_2 \sin \theta \cos \theta] \frac{d\theta}{4\pi(1-\nu)} \right\} \\ = \lim_{\epsilon \rightarrow 0} \left\{ - \frac{1}{2} u_1(p) \right\} = - \frac{1}{2} u_1(p)$$

The same thing can be shown to apply for $j = 2$ The limit is then

$$\begin{aligned}
\lim_{p(\underline{x}) \rightarrow P(\underline{x})} \int_S u_i(Q) T_{ji}(p, Q) dS(Q) \\
= -\frac{1}{2} u_j(P) + \int_S u_i(Q) T_{ji}(P, Q) dS(Q)
\end{aligned} \tag{3-28}$$

where the Cauchy Principal Value of the above integral is taken.

The limit

$$\begin{aligned}
\lim_{p(\underline{x}) \rightarrow P(\underline{x})} \int_S t_i(Q) U_{ji}(p, Q) dS(Q) \\
= \lim_{\epsilon \rightarrow 0} \int_{S-S_\epsilon} t_i U_{ji} dS + \lim_{\epsilon \rightarrow 0} \int_{S_\epsilon} t_i U_{ji} dS
\end{aligned}$$

The second limit on the right hand side can easily be shown to be zero, hence

$$\begin{aligned}
\lim_{p(\underline{x}) \rightarrow P(\underline{x})} \int_S t_i(Q) U_{ji}(p, Q) dS(Q) \\
= \int_S t_i(Q) U_{ji}(P, Q) dS(Q)
\end{aligned} \tag{3-29}$$

Substituting these limits, Equations (3-27), (3-28) and (3-29), yields the boundary constraint equation for the case of smooth boundary

$$\begin{aligned}
\frac{1}{2} u_j(P) + \int_S u_i(Q) T_{ji}(P, Q) dS(Q) \\
= \int_S t_i(Q) U_{ji}(P, Q) dS(Q)
\end{aligned} \tag{3-30}$$

The BIE for the three-dimensional case essentially has the same form

as Equation (3-30) and its derivation may be found in reference [33].

For the case of the non smooth boundaries, the BIE, Equation (3-30), takes the form [34].

$$\begin{aligned} c_{ji}(P)u_i(P) + \int_S u_i(Q)T_{ji}(P,Q)dS(Q) \\ = \int_S t_i(Q)U_{ji}(P,Q)dS(Q) \end{aligned} \quad (3-31)$$

In Equation (3-31) c_{ij} is a matrix of numbers and depends only upon local geometry of the boundary at $P(\underline{x})$. In practice, c_{ij} is most expediently calculated by noting that an arbitrary rigid body translation of R is a solution of Equation (3-31) [15]. If the body force, b_i , is considered, Equation (3-31) takes the form [23].

$$\begin{aligned} c_{ji}(P)u_i(P) + \int_S u_i(Q)T_{ji}(P,Q)dS(Q) \\ = \int_S t_i(Q)U_{ji}(P,Q)dS(Q) + \int_R b_i(q)U_{ji}(P,q)dV(q) \end{aligned} \quad (3-32)$$

Equation (3-31) can be viewed as the constraint equation relating surface tractions to surface displacements. In physical problems the tractions and displacements are not known concurrently over the entire surface. Thus the mechanism of solution is to regard Equation (3-31) as a set of coupled integral equations of varying types according as data appropriate to the traction, displacement or mixed boundary value problems are prescribed.

Exact solutions to Equation (3-31) are, in general, not obtainable and Equation (3-31) must be solved numerically for the unknown boundary data. Once this is done, the solution for displacement or

stress at any interior point $p(\underline{x})$ of R may be obtained, in terms of the surface pair u_i, t_i , by comparatively simple quadrature using Equations (3-23) and (3-24) respectively.

A closing discussion of this section is the treatment of Equation (3-32) where body force is included. The presence of body force $b_i(q)$ in this equation removes the problem from 'boundary only' category, assuming that the volume integral cannot be analytically performed. However, it has been shown in Reference [35] that it is possible to convert this volume integral to a surface integral when the body force, real or thermal equivalent, is derivable from a scalar potential whose Laplacian is at most a constant. Now if there exists a scalar ψ such that

$$b_i = -\psi_{,i} \text{ with } \psi_{,ii} = k_0 \quad (k_0 = \text{constant})$$

The volume integral in Equation (3-32) is convertible to an S integral and the BIE for this case may be written as [23]

$$\begin{aligned} c_{ji}(P)u_i(P) + \int_S [u_i(Q)T_{ji}(P,Q) - \{c_i(Q) - \psi(Q)n_i(Q)\} \\ u_{ji}(P,Q)]dS(Q) \\ = \mu_0 \int_S [\psi(Q) \frac{\partial r_{,j}}{\partial n}(P,Q) - \{\frac{\partial}{\partial n} \psi(Q)\} r_{,j}(P,Q) \\ + k_0 n_j(Q)r(P,Q)]dS(Q) \end{aligned} \quad (3-33)$$

where $\mu_0 \equiv (1-2\nu)/16\pi\mu(1-\nu)$

Equation (3-33) is now amenable to a systematic 'boundary only' numerical treatment.

3.3 Formulation of the Numerical Solution Technique for Plane Problems

As stated in the previous section, analytical solution to the BIE, Equation (3-31), are not generally available. A general scheme for obtaining numerical solutions for the case of plane elasticity is discussed in this section. This scheme is to replace the continuous definition of the boundary data in Equation (3-31) by some discrete variation that will reduce it to a set of linear algebraic equations. The boundary is approximated by a set of boundary segments over which u_j , t_j vary in some specific manner.

The approach followed here is the use of isoparametric shape functions for the representation of both geometry and boundary data [36]. The basis of the isoparametric method is the mapping of a planar curve to a standard interval by means of a fixed set of shape functions. The boundary is discretized into a total number M of boundary segments; each is defined by n nodes. The cartesian co-ordinates x_i^α of each node are specified, and the cartesian co-ordinates of a non-nodal point of a segment are assumed to be given by* (cf. Reference 36).

$$x_i(\xi) = \sum_{\alpha=1}^n N^\alpha(\xi) x_i^\alpha \quad (3-34)$$

in which $N^\alpha(\xi)$ are the shape functions of intrinsic coordinate ξ ($-1 \leq \xi \leq 1$) of the boundary element.

* Generally for the isoparametric representation of geometry not higher than quadratic shape function are used [36].

Boundary data can be modeled using a similar isoparametric representation as used for the geometry, Equation (3-34). The displacement vector of a point $Q(\underline{x})$ on segment (σ) is given by

$$\begin{Bmatrix} u_1(Q) \\ u_2(Q) \end{Bmatrix}_{\sigma} = \underline{N} \underline{u}_{\sigma} \quad (3-35)$$

$$\text{where } \underline{N} \equiv \begin{bmatrix} N^1(\xi)N^2(\xi)N^3(\xi) & \cdots & 0 & 0 & 0 & \cdots \\ 0 & 0 & 0 & \cdots & N^1(\xi)N^2(\xi)N^3(\xi) & \cdots \end{bmatrix}$$

and \underline{u}_{σ} is a vector contains the displacements of the nodal points of the segment; namely

$$\underline{u}_{\sigma}^T \equiv \{u_1^1 u_1^2 u_1^3 \quad \cdots \quad u_2^1 u_2^2 u_2^3 \quad \cdots\}_{\text{seg. } \sigma}$$

with similar expression for $\begin{Bmatrix} t_1(Q) \\ t_2(Q) \end{Bmatrix}_{\sigma}$.

Writing Equation (3-31) for a nodal point P_n (see Figure 3-3)

$$\begin{aligned} c_{ji}(P_n)u_i(P_n) + \sum_{\sigma=1}^M \int_{S_{\sigma}} u_i(Q)T_{ji}(P_n, Q)dS(Q) \\ = \sum_{\sigma=1}^M \int_{S_{\sigma}} t_i(Q)u_{ji}(P_n, Q)dS(Q) \end{aligned} \quad (3-36)$$

where the integrals of Equation (3-31) are now divided into the sum of M integrals along the surfaces S_{σ} of the boundary segments.

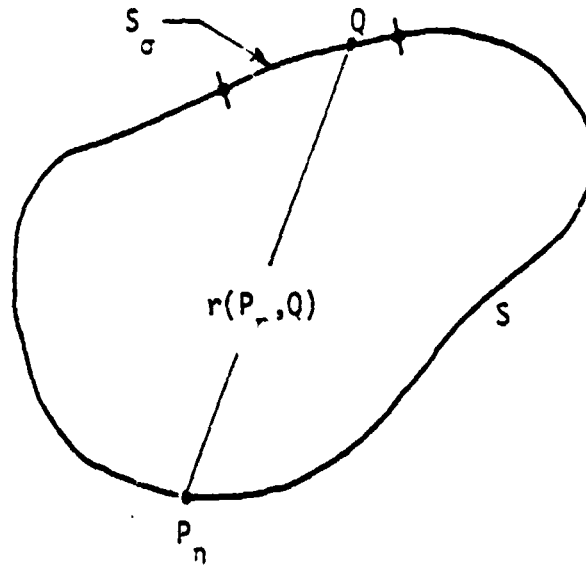


Figure 3-3. Integration Along Boundary Segment (σ)

Based on the discretizing assumptions, the parametric functional representations for $u_i(Q)$ and $t_i(Q)$, Equation (3-34) are substituted into Equation (3-36) to obtain for a particular nodal point P_n

$$\begin{aligned}
 c_{ji}(P_n)u_i(P_n) + \sum_{\sigma=1}^M \sum_{\alpha=1}^n u_i^{(\sigma,\alpha)} \int_{S_\sigma} T_{ji}(P_n, Q(\xi)) N^\alpha(\xi) J(\xi) d\xi \\
 = \sum_{\sigma=1}^M \sum_{\alpha=1}^n t_i^{(\sigma,\alpha)} \int_{S_\sigma} U_{ji}(P_n, Q(\xi)) N^\alpha(\xi) J(\xi) d\xi
 \end{aligned} \quad (3-37)$$

where $u_i^{(\sigma,\alpha)}$ and $t_i^{(\sigma,\alpha)}$ are the displacements and tractions at local node α on the boundary segment σ . Summation is implied on the repeated indices i and j . The range of the indices i and j is now $\{1,2\}$. $J(\xi)$ is the Jacobian $\frac{dS(Q)}{d\xi}$ which more explicitly is

$$|J(\xi)| = \frac{dS(Q)}{d\xi} = \left\{ \left(\frac{dx_1}{d\xi} \right)^2 + \left(\frac{dx_2}{d\xi} \right)^2 \right\}^{1/2} \quad (3-38)$$

Writing Equation (3-37) for every node and performing the integrations over each segment on S , including that segment which contains P_n itself, a system of $2N$ algebraic equations will result where N is the total number of nodes.

Introducing the short notation

$$[\Delta T_{ji}]_{n\sigma}^\alpha \equiv \int_{S_\sigma} T_{ji}(P_n, Q(\xi)) N^2(\xi) J(\xi) d\xi \quad (3-39)$$

$$[\Delta U_{ji}]_{n\sigma}^\alpha \equiv \int_{S_\sigma} U_{ji}(P_n, Q(\xi)) N^2(\xi) J(\xi) d\xi$$

Equation (3-37) can be written in the following form

$$c_{ji}^n u_i^n + \sum_{\sigma=1}^M \sum_{\alpha=1}^n u_i^{(\sigma, \alpha)} [\Delta T_{ji}]_{n\sigma}^\alpha = \sum_{\sigma=1}^M \sum_{\alpha=1}^n t_i^{(\sigma, \alpha)} [\Delta U_{ji}]_{n\sigma}^\alpha \quad (n = 1, 2, \dots, N) \quad (3-40)$$

The integrals in Equation (3-39) have the meaning that integration of the kernel function over the segment σ for the nodal point n .

Introducing a global numbering for the nodes along the boundary S , this leads to viewing the system of equations (3-40) in the following global matrix form

$$\underline{c} \underline{U} + \underline{h} \underline{U} = \underline{G} \underline{I} \quad (3-41)$$

or

$$\underline{H} \underline{U} = \underline{G} \underline{I} \quad (3-42)$$

In Equation (3-42), the column matrices \underline{U} and \underline{I} are of dimension $2N$

and contain the elements u_i^β , t_i^β , $\beta = 1, 2, \dots, N$, which are, respectively, the displacement and traction components at global node number β . The square matrices $\underline{H} \equiv \underline{c} + \underline{h}$ and \underline{G} are $2N \times 2N$ elements in size and contain the integral coefficients of \underline{U} and \underline{T} as indicated in Equation (3-40). These coefficients are sums of integrals of kernel-shape function products, and generally evaluated using Gaussian quadrature formulae. \underline{c} is a diagonal matrix, which does not need to be determined explicitly.

For the case when $n=s$, there is no need to evaluate separately the Cauchy Principal Value of the integral $[\Delta T_{ji}]_{n\sigma}^\alpha$, Equation (3-40), and the coefficients c_{ij}^n of the free term; so the coefficients in the \underline{H} matrix can be calculated using the fact that the stress field corresponding to a rigid body translation is zero. Assuming unit rigid body translations (in the x_1 and x_2 directions), Equation (3-42) yields

$$\underline{H} \underline{I} = \underline{0} \quad (3-43)$$

where \underline{I} is a unit vector. Thus the sum of all the elements of \underline{H} in any row ought to be zero, and the value of the coefficient on the diagonal is simply equal to the sum of all the off-diagonal terms with sign changed.

The numerical procedure for solving the BIE for plane elasticity problems discussed thus far will now be applied to the case of assuming linear variation of the boundary functions. The linear boundary element scheme is simple and direct and offers a greater flexibility in solving general problems in solid mechanics. It is

quite adequate for practical applications when the BIE method is used in conjunction with the experimental techniques for measuring in-plane displacement components. For these applications the region of interest is enclosed by a closed contour on which the displacement components at the nodal points are measured experimentally. Normally the region of interest is relatively a small area and, therefore, its contour may be approximated by a sequence of short straight line segments. A computer program based on the linear functional variations along the boundary was used for the BIE calculations for the example problems conducted in this dissertation. Good degree of accuracy has been achieved from using this procedure as will be shown in Chapter V.

For linear elements (Figures 3-4), the variation of the functions $u_i(Q)$ and $t_i(Q)$ between nodes is assumed to be linear. The nodes are considered to be at the intersection between two straight line elements and marked as extreme nodes. There are two shape functions

$$N^1 \equiv N^1(\xi) = -\frac{1}{2}(\xi-1)$$

$$\text{and } N^2 \equiv N^2(\xi) = \frac{1}{2}(\xi+1)$$

and the Jacobian is simply $J(\xi) = \frac{l_\sigma}{2}$, where l_σ is the element length.

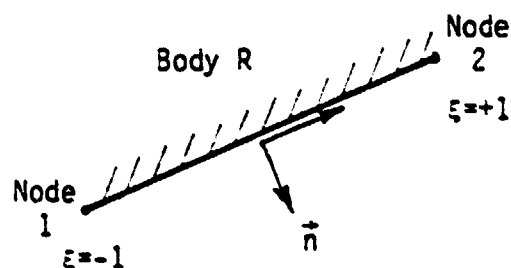


Figure 3-4. Linear Boundary Element

The assembled equation for node n , Equation (3-37), may be written in a matrix form for the case at hand as

$$\underline{c}^n \underline{u}^n + [\underline{a}_{n\sigma}] \{\underline{u}_\sigma\} = [\underline{B}_{n\sigma}] \{\underline{t}_\sigma\} \quad (3-44)$$

$(\sigma = 1, 2, \dots, M)$

In Equation (3-44) $\underline{a}_{n\sigma}$ is a (2×4) submatrix defined by

$$\underline{a}_{n\sigma} = \frac{l_\sigma}{2} \begin{bmatrix} \int_{S_\sigma} N^1 T_{11} d\xi & \int_{S_\sigma} N^2 T_{11} d\xi & \int_{S_\sigma} N^1 T_{12} d\xi & \int_{S_\sigma} N^2 T_{12} d\xi \\ \int_{S_\sigma} N^1 T_{21} d\xi & \int_{S_\sigma} N^2 T_{21} d\xi & \int_{S_\sigma} N^1 T_{22} d\xi & \int_{S_\sigma} N^2 T_{22} d\xi \end{bmatrix}$$

with a similar definition for $\underline{B}_{n\sigma}$. The elements of the submatrix $\underline{a}_{n\sigma}$ are integrals along the element σ corresponding to node n .

Note that N^1 and N^2 are functions of ξ and $T_{ij} \equiv T_{ij}(P_n, Q(\xi))$;

$\frac{l_\sigma}{2} =$ the Jacobian $J(\xi)$ and l_σ is the length of segment.

It is more convenient to rewrite Equation (3-44) in terms of the nodal displacement and traction vectors in the following forms

$$\underline{c}^n \underline{u}^n + [\hat{\underline{A}}_{n\rho}] \{\underline{u}^\rho\} = [\underline{B}_{n\rho}] \{\underline{t}^\rho\} \quad (3-45)$$

$(\rho = 1, 2, \dots, N)$

where N is the total number of nodes = the total number of segments,

and the vector \underline{u}^ρ is the displacement vector at node (ρ) ; namely

$$\underline{u}^\rho = \begin{Bmatrix} u_1 \\ u_2 \end{Bmatrix}_{\text{node } \rho} = \begin{Bmatrix} u_1^\rho \\ u_2^\rho \end{Bmatrix}$$

with a similar definition for \underline{t}^ρ . The coefficient $\hat{\underline{A}}_{n\rho}$ in Equation

(3-45) is now a (2×2) submatrix given by

$$\hat{A}_{np} = \frac{1_p}{2} \left[\begin{array}{c|c} \int_{S_p} N^1 T_{11} d\xi & \int_{S_p} N^1 T_{12} d\xi \\ \hline \int_{S_p} N^1 T_{21} d\xi & \int_{S_p} N^1 T_{22} d\xi \end{array} \right] + \frac{1_{p-1}}{2} \left[\begin{array}{c|c} \int_{S_{p-1}} N^2 T_{11} d\xi & \int_{S_{p-1}} N^2 T_{12} d\xi \\ \hline \int_{S_{p-1}} N^2 T_{21} d\xi & \int_{S_{p-1}} N^2 T_{22} d\xi \end{array} \right]$$

which contains integral over the two adjacent segments meeting at node p . When $p=1$, N is used instead of $(p-1)$ in the above expression.

At any node there will be a single unique vector for the nodal displacement; the same thing is not always true for the traction vector at the common nodal point. To properly account for discontinuities of nodal tractions a zero-length segment is to be introduced at that nodal point. Riccardella [37] has shown for the case of linear functional variations that zero-length segments can be added at any point where a step change in boundary conditions occurs, and zero values can be assigned to the integrals associated with these zero-length segments.

Writing Equation (3-45) for every node, a system of algebraic equations will result,

$$\{c^n \underline{u}^n\} + [\hat{A}_{np}] \{\underline{u}^p\} = [B_{np}] \{\underline{t}^p\} \quad (3-46)$$

or

$$[A_{np}] \{\underline{u}^p\} = [B_{np}] \{\underline{t}^p\} \quad (3-47)$$

where

$$\begin{aligned} A_{np} &= \hat{A}_{np} & \text{when } n \neq p \\ A_{np} &= \hat{A}_{np} + c^n & \text{when } n = p \end{aligned} \quad (3-48)$$

The integrals for $[A_{np}]$ and $[B_{np}]$ may be evaluated in closed form. Again there is no need to calculate separately the diagonal coefficients of the matrix $[A_{np}]$ as discussed earlier in this section. Assuming a unit rigid body translation in both x_1 and x_2 direction, i.e., $\{u^p\} \equiv \underline{1}$, the corresponding boundary traction is $\{t^p\} \equiv \underline{0}$, then from Equation (3-47) the value of the diagonal coefficients is

$$A_{nn} = - \sum_{\substack{p=1 \\ p \neq n}}^N A_{np} \quad (3-49)$$

Any well-posed boundary value problem will have $2N$ knowns and $2N$ unknowns. Once the knowns of the boundary data have been specified, the system of equations, Equation (3-42), can be re-ordered in such a way that all the unknowns are on the left side, i.e.,

$$\underline{K}\underline{X} = \underline{Y} \quad (3-50)$$

The vector \underline{X} will contain $2N$ unknown nodal values of traction or displacement. The vector \underline{Y} contains the product of the calculated integrals and the corresponding known boundary data. The system of equations (3-50) is to be formed directly, and thus the storage of matrices \underline{H} and \underline{G} has been avoided. Only the matrix of coefficients of the unknowns at the nodes need be formed and stored in a square array (matrix \underline{K}). The elements of the other matrix of coefficients to be multiplied by known quantities may be immediately multiplied by such quantities as they are generated and stored in a column vector and not as a separate square array.

The order of magnitude of the terms in matrix \underline{H} is approximately (μ) times that of the terms in matrix \underline{G} (where μ is the shear modulus).

Thus during the formation of matrix \underline{K} , the coefficients of the unknown nodal tractions have been scaled using the shear modulus to maintain the same order of magnitude for the unknowns. The system of Equations (3-50) is numerically stable and is now directly solvable by standard reduction scheme (Gaussian elimination).

While one of the major potential numerical advantages of integral equation methods is reduced problem dimension by solving boundary equations, another major feature is the internal solution capability. Once the system of Equations (3-50) is solved, the now completely known discretized boundary data may be used to evaluate the displacements and stress tensor at any interior point $p(\underline{x})$ by direct integration of the identities (3-23) and (3-24) with the boundary-integrals discretized in the same manner as Equation (3-37):

$$\begin{aligned} u_j(p) = & \sum_{\sigma=1}^M \sum_{\alpha=1}^n t_i^{(\sigma,\alpha)} \int_{S_\sigma} U_{ji}(p, Q(\xi)) N^\alpha(\xi) J(\xi) d\xi \\ & - \sum_{\sigma=1}^M \sum_{\alpha=1}^n u_i^{(\sigma,\alpha)} \int_{S_\sigma} T_{ji}(p, Q(\xi)) N^\alpha(\xi) J(\xi) d\xi \end{aligned} \quad (3-51)$$

and

$$\begin{aligned} \sigma_{ij}(p) = & \sum_{\sigma=1}^M \sum_{\alpha=1}^n t_k^{(\sigma,\alpha)} \int_{S_\sigma} D_{kij}(p, Q(\xi)) N^\alpha(\xi) J(\xi) d\xi \\ & - \sum_{\sigma=1}^M \sum_{\alpha=1}^n u_k^{(\sigma,\alpha)} \int_{S_\sigma} S_{kij}(p, Q(\xi)) N^\alpha(\xi) J(\xi) d\xi \end{aligned} \quad (3-52)$$

where summation is implied on repeated i or k indices. Again the indicated integrations may be evaluated numerically (using Gaussian quadrature formula) and $u_j(p)$ and $\sigma_{ij}(p)$ are found for any interior

point. By keeping the discretization on the boundary very high numerical resolution may be obtained, from Equations (3-51) and (3-52), a feature quite unlike finite difference and finite element analyses. When high resolution is required or only a limited number of internal point solutions are desired the integral equation method is significantly faster than finite element solutions.

It should be mentioned here that the calculated values of the stress tensor at interior points very near to the boundary are not very accurate, since the boundary is defined only by the coordinates of the nodes, and traction and displacement data are available only at the nodes. It has been found that an interior point can be within a distance equal to the length of the nearest boundary segment and still maintain ordinary accuracy, i.e., accuracy comparable to that available for the other interior points at distance from the boundary more than the length of nearest segment.

Not being able to take $p(x)$ arbitrarily close to the boundary is not a limitation, however, since stresses right on the boundary may be obtained with no reference to the interior field. The boundary stress field may be obtained directly from knowledge of both tractions and boundary displacements. Since at this stage u_i on S is known at the nodes such that $\frac{du_i}{ds}\bigg|_p$ can be obtained numerically (and sometimes experimentally). Noting further that

$$\frac{du_i}{ds}\bigg|_p = u_{i,j}q_j = u_{i,2}n_1 - u_{i,1}n_2 \quad (3-53)$$

where \vec{q} is the unit tangent to S at P , and the tangential derivative $\frac{du_i}{ds}$ is assumed keeping the material on the left while moving in a

direction of positive S . Equation (3-53) together with Hooke's law, Equation (3-2), and the boundary traction $t_i = \sigma_{ij}n_j$ on S constitute sufficient information to determine the state of stress, σ_{ij} , at each node. The above relation can be casted in the following matrix form [18]

$$\underline{B}\underline{J} = \underline{M} \quad (3-54)$$

in which

$$\underline{J} = \left\{ \begin{array}{c} \sigma_{11} \\ \sigma_{22} \\ \sigma_{12} \\ u_{1,1} \\ u_{2,1} \\ u_{1,2} \\ u_{2,2} \end{array} \right\}_P \quad \text{and} \quad \underline{M} = \left\{ \begin{array}{c} 0 \\ t_1 \\ t_2 \\ 0 \\ u_{1,s} \\ 0 \\ u_{2,s} \end{array} \right\}_P$$

The square matrix \underline{B} contains the elastic constants and the components of n_i and q_i . After obtaining numerically (or sometimes experimentally) the components $u_{1,s}$ and $u_{2,s}$ at a given node point P , the system of Equations (3-54) becomes ready for convenient computation. The derivatives $u_{i,s}$ plus t_i at P complete the column \underline{M} such that the stress components σ_{ij} on S are obtained as the solution of Equation (3-54) for each node. Along with the stresses, the displacement gradients $u_{i,j}$ are also obtained, although the later are not normally of interest.

The BIE solution method can easily be used to study problems with more than one surface, such as the case of a body with holes illustrated in Figure 3-5. In order to define an external or

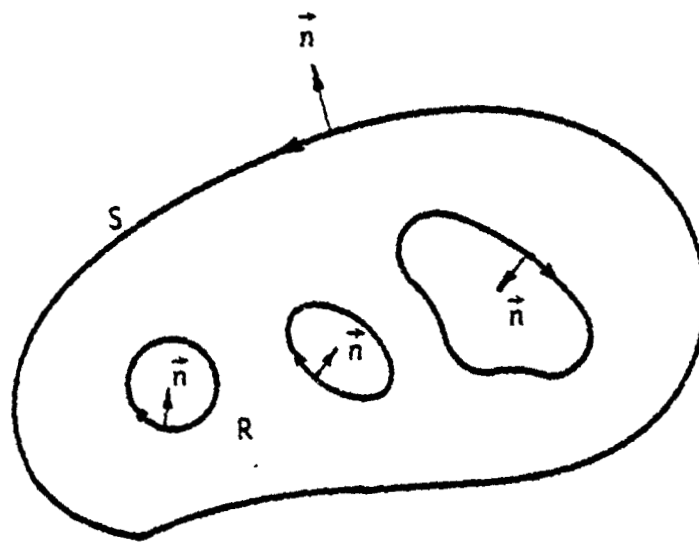


Figure 3-5. Multiply Connected Body

internal boundary, direction of the normal needs to be identified. This can be done for two dimensional problems by defining a numbering scheme as the boundary is traversed in the counterclockwise direction keeping the body material to the left.

Finally, a basic conceptual advantage of the BIE method is that it applies to three dimensions as well as two with similarly defined integral equations arising in each case [13]. The procedure for three dimensional problems is similar, except the number of equations and unknowns is now larger, and evaluation of the coefficients involves surface integrals over the surface segments rather than line integrals over line segments.

IV. THE EXPERIMENTAL PROGRAM AND DATA ACQUISITION

4.1 Experimental Equipment

The experimental arrangement for making a double exposure specklegram is shown in Figure 4-1. It is, in fact, a simple camera configuration. Monochromatic and coherent laser light is used to illuminate the specimen which provides for a speckle appearance on a diffuse surface. Light reflected from the object is imaged onto high resolution photographic film. Thin emulsion holographic films such as Agfa-Gevaert holotest 10E56 are commonly used. For the point-by-point data analysis, a set up similar to the one shown in Figure 2-6 may be used. A helium-neon laser with one to fifteen milli-watts of output will provide adequate illumination. To obtain good resolution of changes in displacement with respect to location, a small diameter input beam is preferred. The diffraction halo with fringes is observed on a screen. The procedure for determining the in-plane displacement components at a point was discussed in Section 2.3 of Chapter II.

A computer aided data reduction system was developed primarily for application in speckle interferometry data analysis [5]. This system can be used as a mean for the displacement data acquisition for the example problems discussed in this dissertation. The basic idea of the operation of this system is discussed in the next section.

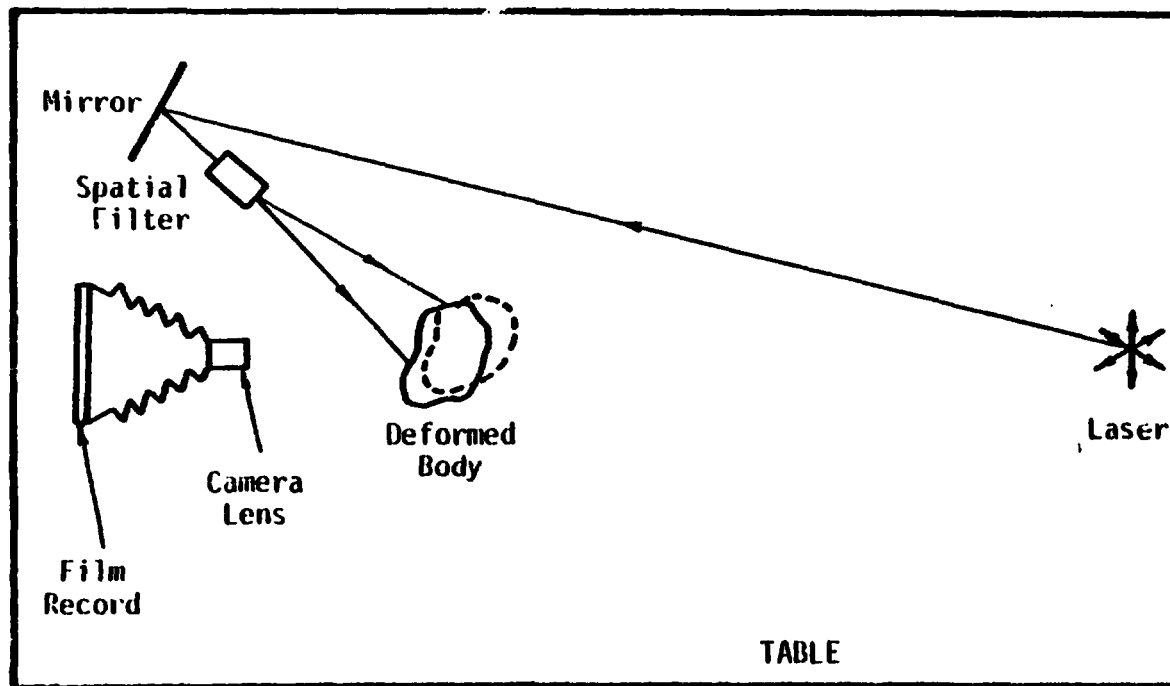


Figure 4-1. Experimental Arrangement for Recording a Specklegram

4.2 Computer-Aided Data Reduction System

The basic system consists of two parts which are an optical recording system and the computer hardware used in the numerical analysis as shown in Figure 4-2.

A typical fringe pattern used for analysis is shown in Figure 4-3. This type of fringe pattern is produced when a laser beam is passed through a photographic transparency as discussed earlier. Interference fringes are a measure of surface deformation of a body. Because only a small area is illuminated by the laser, the information in the data analysis yields the displacement at a point. Therefore, to obtain a complete map of the surface, each point on the film will have to be illuminated. This is accomplished by an x-y translation stage in which the transparency has been mounted. The stage has the capacity to translate 6 inches in each direction in 0.001 inch increments with a .0001 inch repositioning accuracy. Synchronous stepping motors provide the control for the translation directions. A photographic plate is mounted in the window of the translation stage and a He-Ne laser beam passes through a point on the film and the film is translated relative to the stationary laser beam.

Location of a point in the window is controlled by the stepping motors which are in turn controlled by the computer. Thus, the computer can control the translation distance with a minimum interval of 0.001 inch.

Light that is passed through the film then forms a diffraction

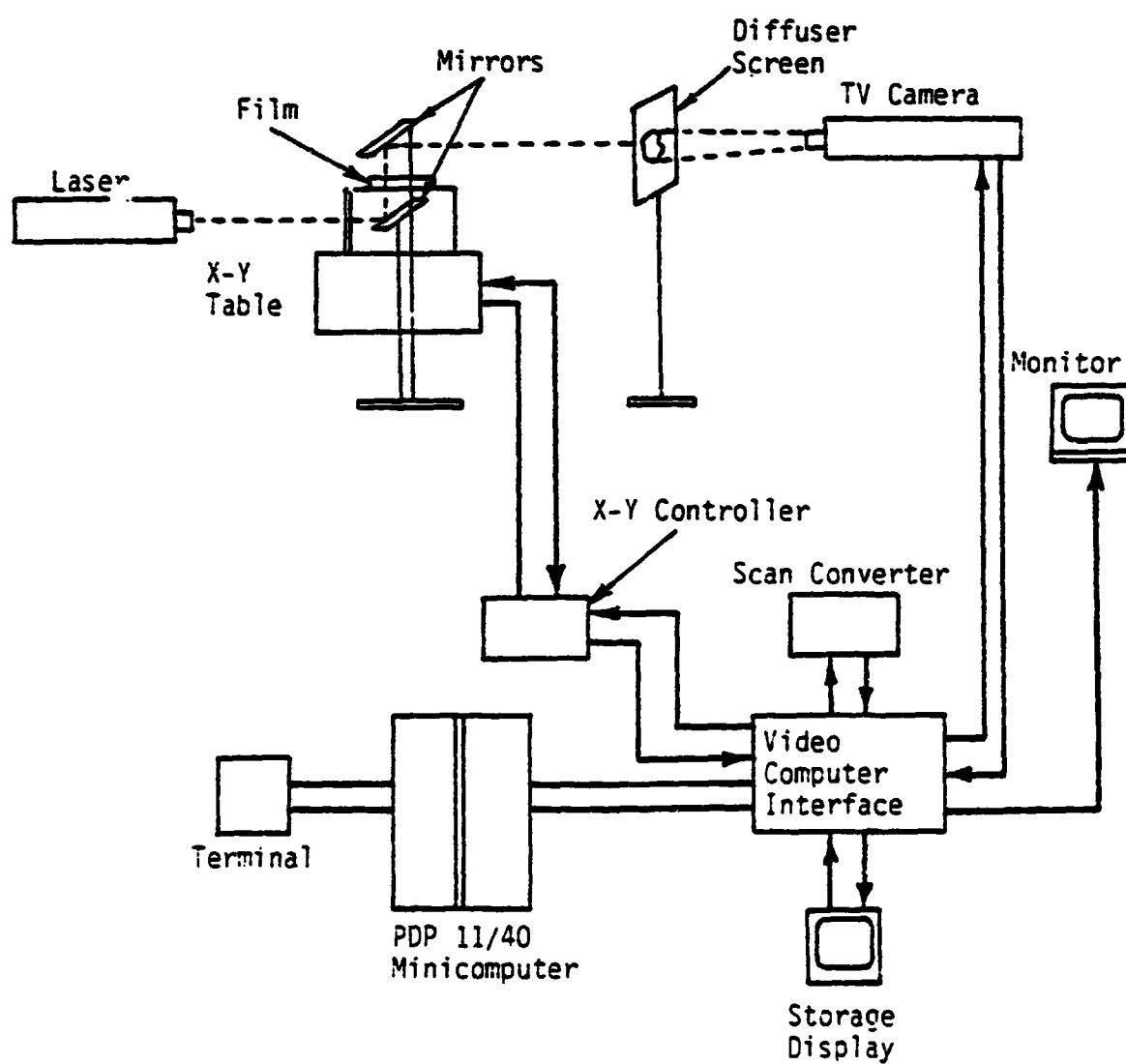


Figure 4-2. Computer Aided Data Analysis System for Las Speckle Interferometry

ORIGINAL PAGE IS
OF POOR QUALITY

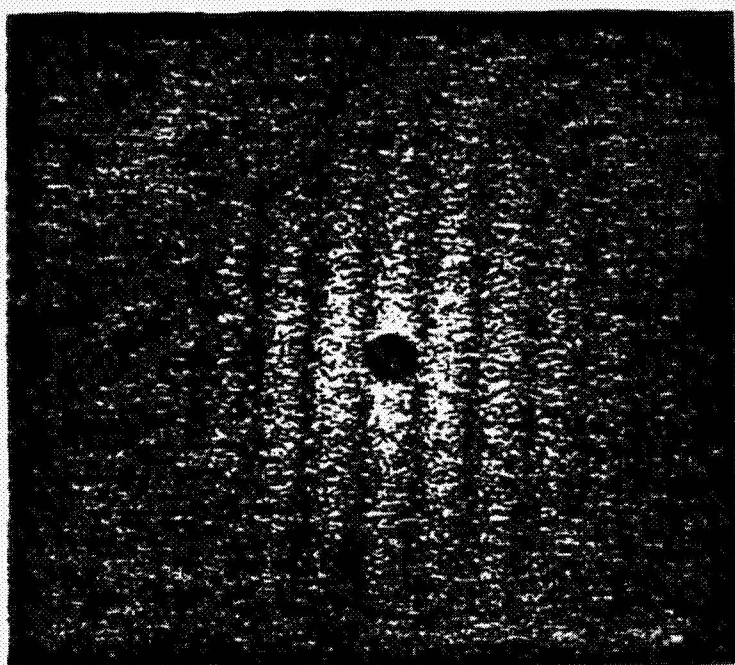


Figure 4-3. Typical Speckle Photography Fringe Pattern Used in the Optical Data Analysis System

pattern which is imaged by a vidicon camera. The image on the camera can then be viewed on a TV monitor or stored in memory in the computer.

A PDP 11/40 minicomputer is used to control the motion of the translation table and process the video signal. Operation of the system begins with a command from the computer to move the table to a specified coordinate position in the table window. With the table in a specified position, the computer sends a command through the video interface to store the vidicon imager in the scan conversion memory. A command from the computer then converts the information stored in the scan conversion memory into digital form. The complete image is not processed but only selected lines of video information are processed because of the requirements in the data analysis. This process completes the data acquisition at a point on the film and the computer then locates a new coordinate position and the process is repeated.

Data analysis consists of determining the locus of points of minimum intensity which is referred to as fringe. However, this analysis is complicated by the fact that the film transparency is illuminated by a coherent light source which produces laser speckle. The presence of this speckle is to superimpose a noise-like signal on the spatial information which degrades the image. A speckle averaging technique is used which reduces the effect of noise in locating points of minimum intensity. Fringe separation is determined by first locating the point of maximum intensity from the

scan average. Then the first minimum point is located to each side of this maximum and the difference in location determines the fringe spacing.

Several examples will now be considered and values of the measured displacements will be presented. The measured values of displacements are used as data input to numerically calculate stresses and displacements through the BIE method as will be discussed later in Chapter V.

4.3 Example 1 - Flexure of a Cantilever Beam With a Transverse End Load

A beam with the end $x = 5.0$ inches fixed and the end $x = 0$ has an end load W_y directed along the negative y -axis was considered and shown in Figure 4-4. Material for the beam was 1/4 inch plexiglas with $E = 4.56 \times 10^5$ psi and $\nu = 0.37$. Fixed end conditions for the beam were obtained by bonding one end of the plexiglas beam to an aluminum block. The transverse end load was governed by the deflection of the free end (because of the constraints on the point-wise filtering of the experimental data). The end load was applied with a micrometer screw and the deflection was recorded with a dial indicator. Free end deflection was $\delta = 0.005$ inches which corresponds to an end load $W_y = 1.14$ lb.

Displacements along the free end were measured experimentally, using the laser speckle technique, and compared with the theoretical values predicted by the stress function solution. The comparison as depicted in Figures 4-5 and 4-6 shows a favorable agreement. Also experimental and theoretical values of the displacement along

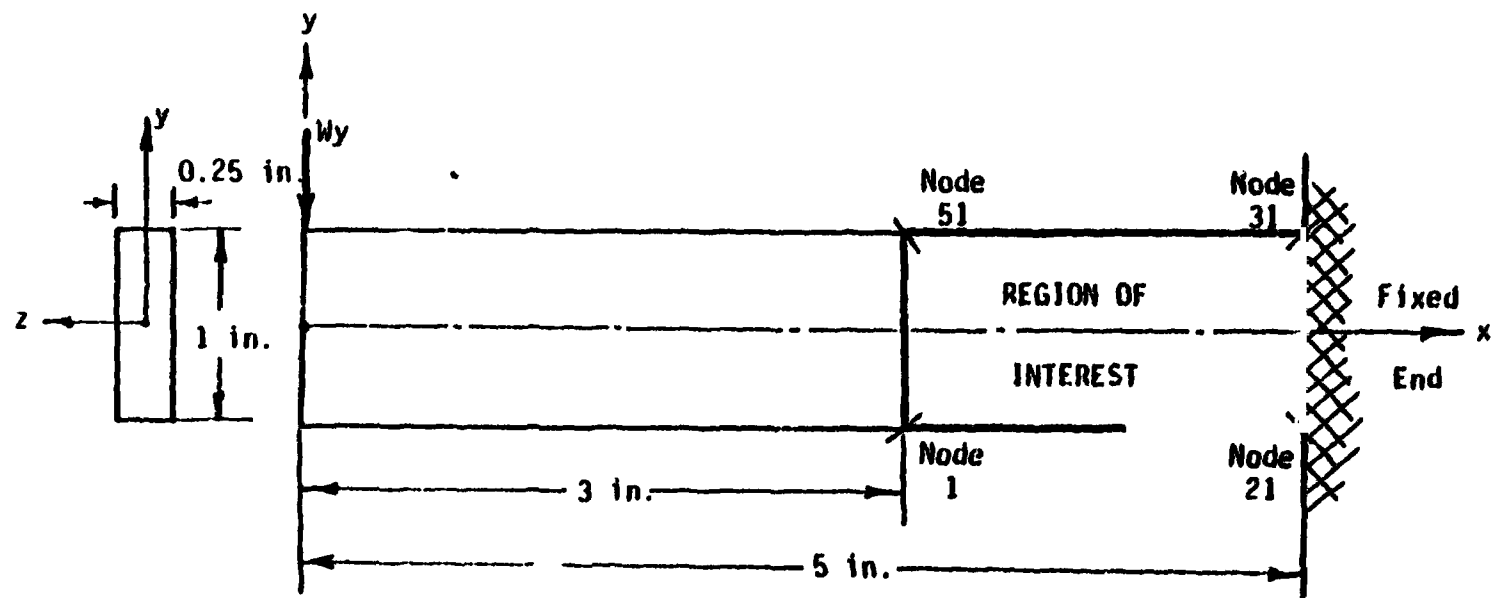


Figure 4-4. Bending of Cantilever Beam with a Transverse End Load

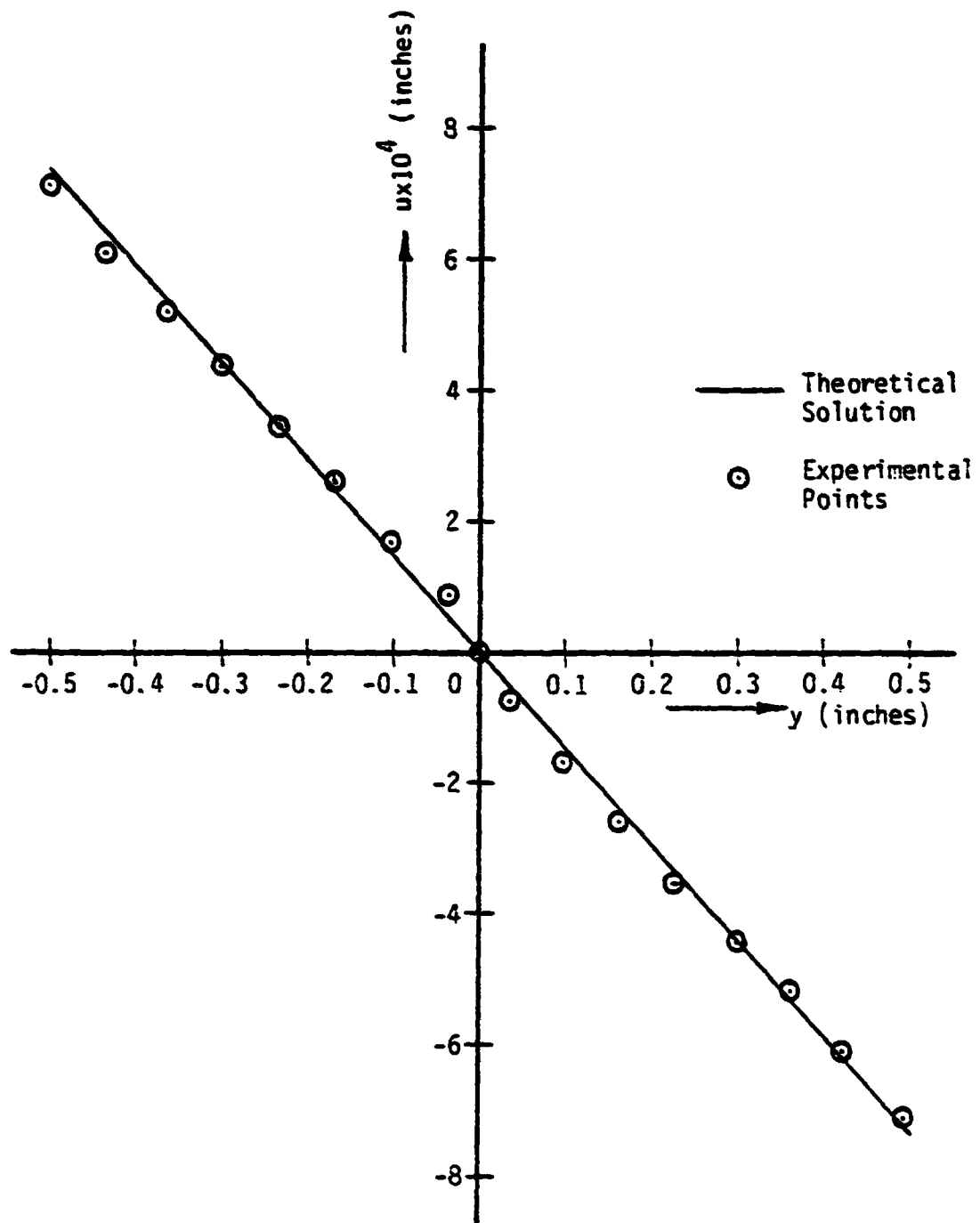


Figure 4-5. Comparison of Theoretical and Experimental Values of the Horizontal Displacement Component Along the Free End

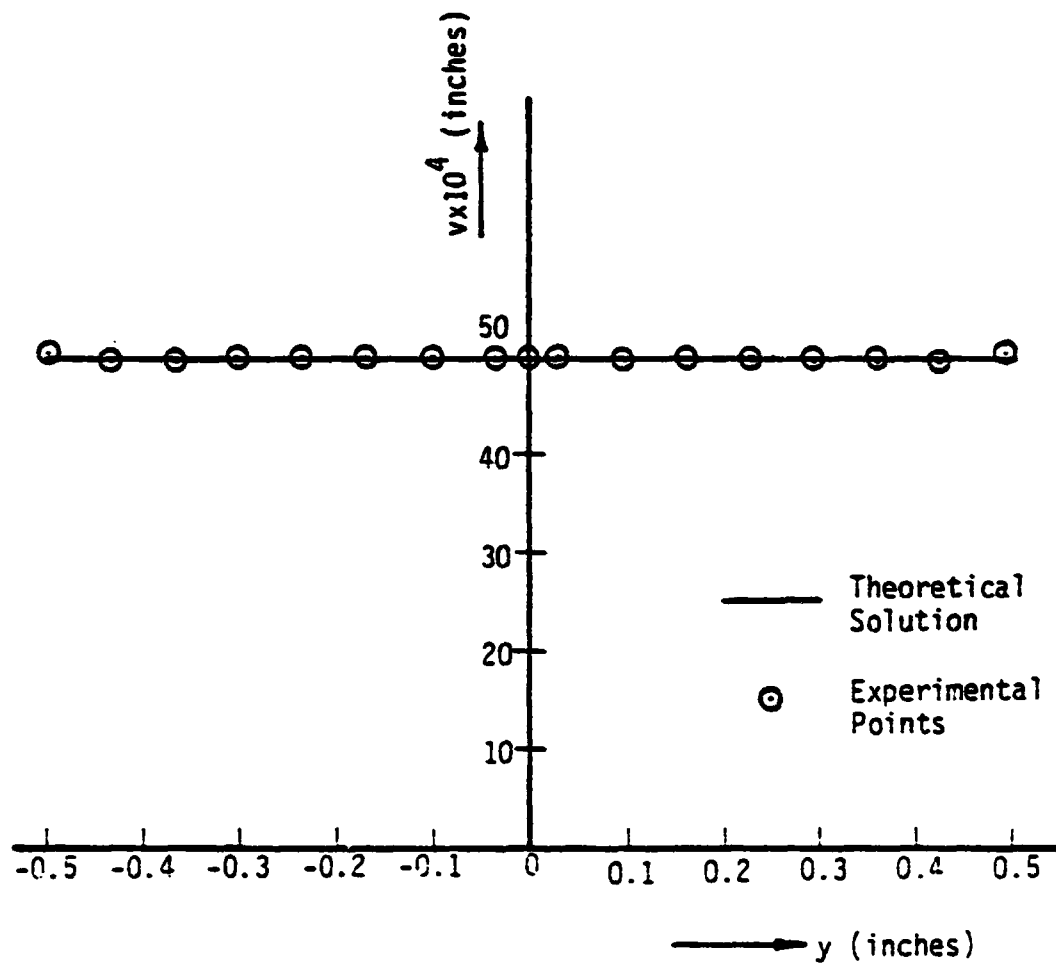


Figure 4-6. Comparison of Theoretical and Experimental Values of the Vertical Displacement Component Along the Free End

the neutral axis of the beam were in a very good agreement as shown previously in Figure 2-8. These favorable comparisons between experiments and theory, at the free end and along the neutral axis of the beam, encourage the use of such experimental technique for measuring the in-plane displacement components along any specified contour.

For the region of interest shown in Figure 4-4, displacement components were measured along the fixed end ($x = 5.0$ inches) which are zero and along the section $x = 3.0$ inches. Data analysis for this line yielded the experimental values of displacement components shown in Table 4-1. This completes the displacement data needed for the BIE solution for this region.

Also the displacement components at some chosen points inside the region of interest along the x-axis were measured and shown in Table 4-2. These values will be used later for the comparison with the BIE calculations as will be discussed in the next chapter. It should be mentioned here that for points at distances greater than 3.6 inches from the free end fringes could not be observed because of the smallness of the displacements at these points.

TABLE 4-1. EXPERIMENTAL VALUES OF THE DISPLACEMENT COMPONENTS ALONG SECTION $x = 3.0$ INCHES FOR THE CANTILEVER BEAM EXAMPLE

| y (inches) | $ux10^4$ (inches) | $vx10^4$ (inches) |
|-----------------|----------------------|----------------------|
| -0.5 | -4.633 | -10.916 |
| -0.4 | -3.531 | -10.868 |
| -0.3 | -2.715 | -10.890 |
| -0.2 | -1.666 | -10.522 |
| -0.1 | -0.913 | -10.435 |
| 0.0 | 0.000 | -10.475 |
| 0.1 | 1.095 | -10.418 |
| 0.2 | 1.788 | -10.688 |
| 0.3 | 2.437 | -10.559 |
| 0.4 | 3.500 | -11.100 |
| 0.5 | 4.633 | -10.916 |

TABLE 4-2. MEASURED DISPLACEMENTS ALONG THE X-AXIS FOR THE CANTILEVER BEAM EXAMPLE

| x (inches) | u | $vx10^4$ (inches) |
|-----------------|-----|----------------------|
| 3.2 | 0.0 | -8.469 |
| 3.4 | 0.0 | -6.686 |
| 3.6 | 0.0 | -5.326 |

4.4 Example 2 - Circular Disk Under Diametral Compression

For this second example problem a circular disk of 3 inches diameter made of 1/4 inch plexiglas was loaded in compression by two diametrically opposing nearly concentrated forces located on the top and bottom of the disk as shown in Figure 4-7. Displacement components at the nodal points along the contour of the region of interest, shown in Figure 4-7, were measured experimentally. The vertical components of the displacement along the horizontal diameter were constant. A zero value was assigned to these components because of the symmetry of the problem about the horizontal diameter. The horizontal components of the displacement along the vertical diameter were measured and are zero. Data analysis for line $y=d/4$ yielded the experimental values of displacement components along that line which are plotted in dimensionless form in Figure 4-8. The horizontal displacement component at node 11 and the vertical displacement component at node 26 were measured to be $u_{11} = 19.7 \times 10^{-5}$ and $v_{26} = -36.9 \times 10^{-5}$ inches respectively. Data input for the BIE solution on prescribed nodes along line $y=d/4$ were taken from the best curve fit of the experimental data shown in Figure 4-8.

Both the horizontal displacement components along the horizontal diameter and the vertical displacement components along the vertical diameter were also measured and will be compared with the BIE calculations as will be shown later in Chapter V.

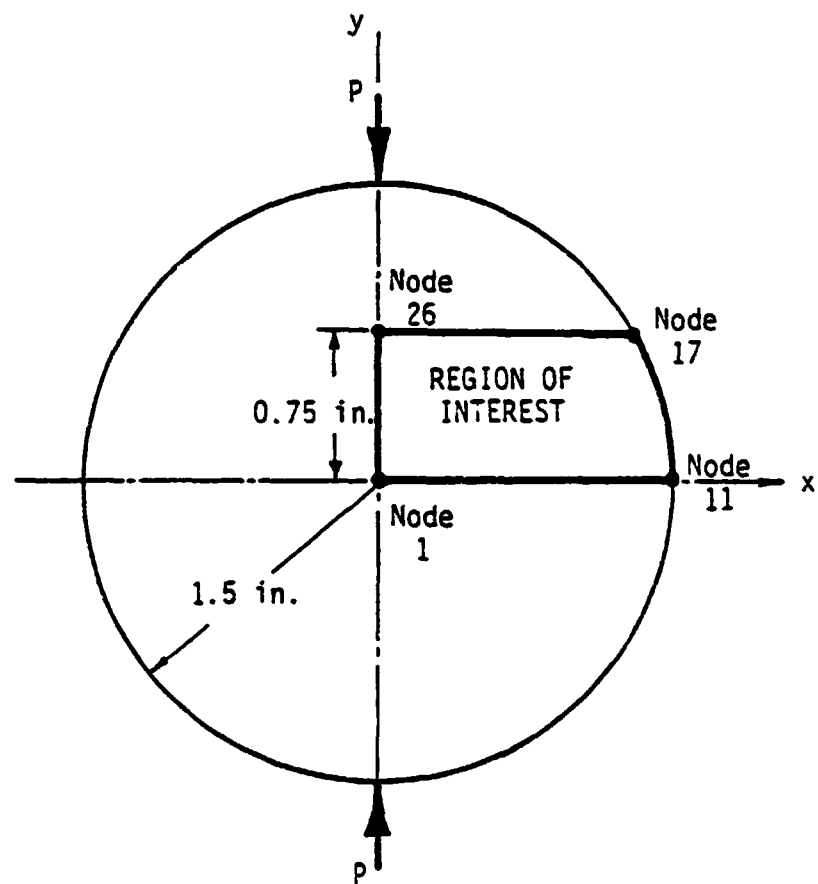


Figure 4-7. Diametrically Loaded Circular Disk

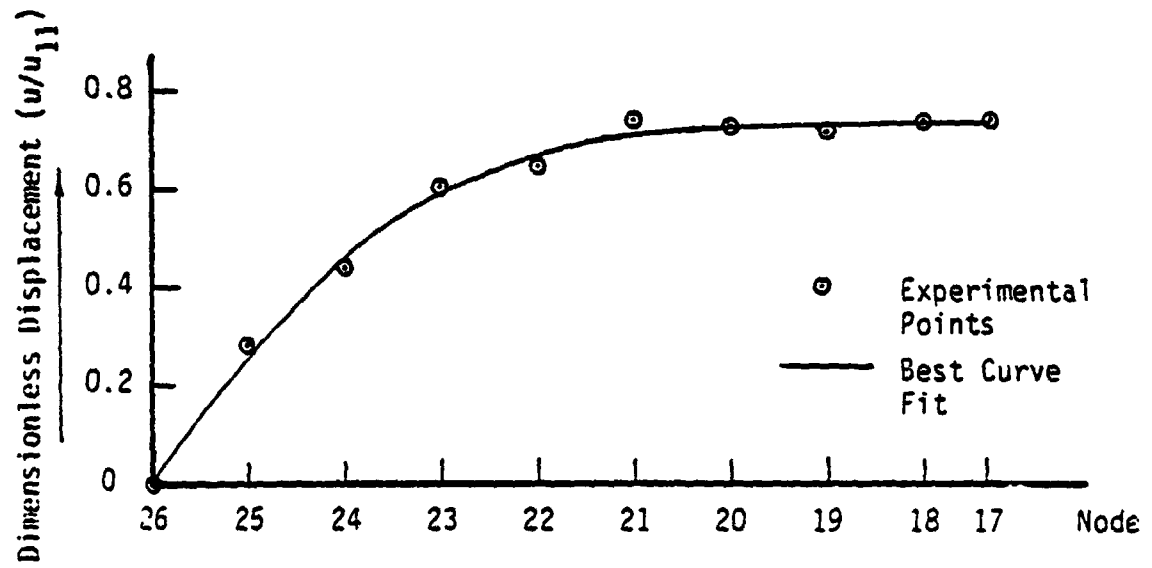


Figure 4-8a. Horizontal Displacement Components
Along Line $y = d/4$

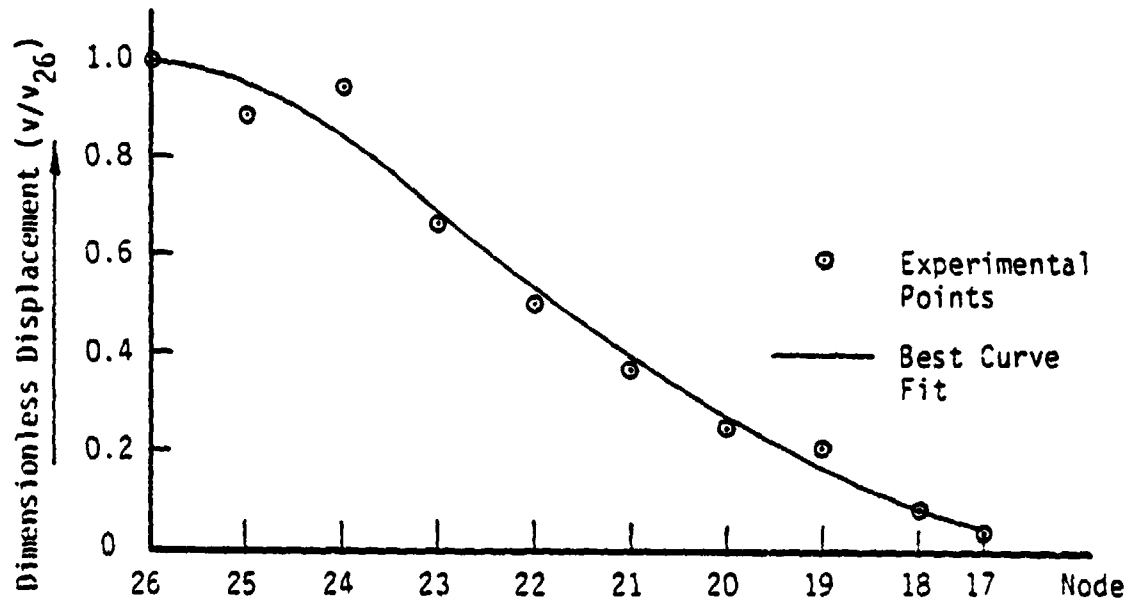


Figure 4-8b. Vertical Displacement Components
Along Line $y = d/4$

4.5 Example 3 - A Plate with a Central Circular Hole Subjected to Uniform Axial Tension

The geometry of the 0.228 inch thickness plexiglas plate used to study this classic stress concentration problem is shown in Figure 4-1. The ratio of hole diameter to plate width is $1/9$. A load P of magnitude 140 pounds was applied in the y direction through 13 equally spaced small holes to assure uniform tension at sections of the plate far from the loading ends.

The region of interest selected for the stress analysis using the BIE method is the portion of the plate within a concentric circle of a diameter four times the hole diameter. Due to symmetry of the problem, only one quadrant of this region is considered. Displacement components at 19 points, of equal angular intervals, along the circular contour of the region of interest (nodes 11-29) were measured experimentally. Table 4-3 is a display of these measured values in dimensionless form. Again, a zero value was assigned to the measured constant value of the vertical displacement components along the x -axis, which is used as a reference for measurement of the vertical displacement components.

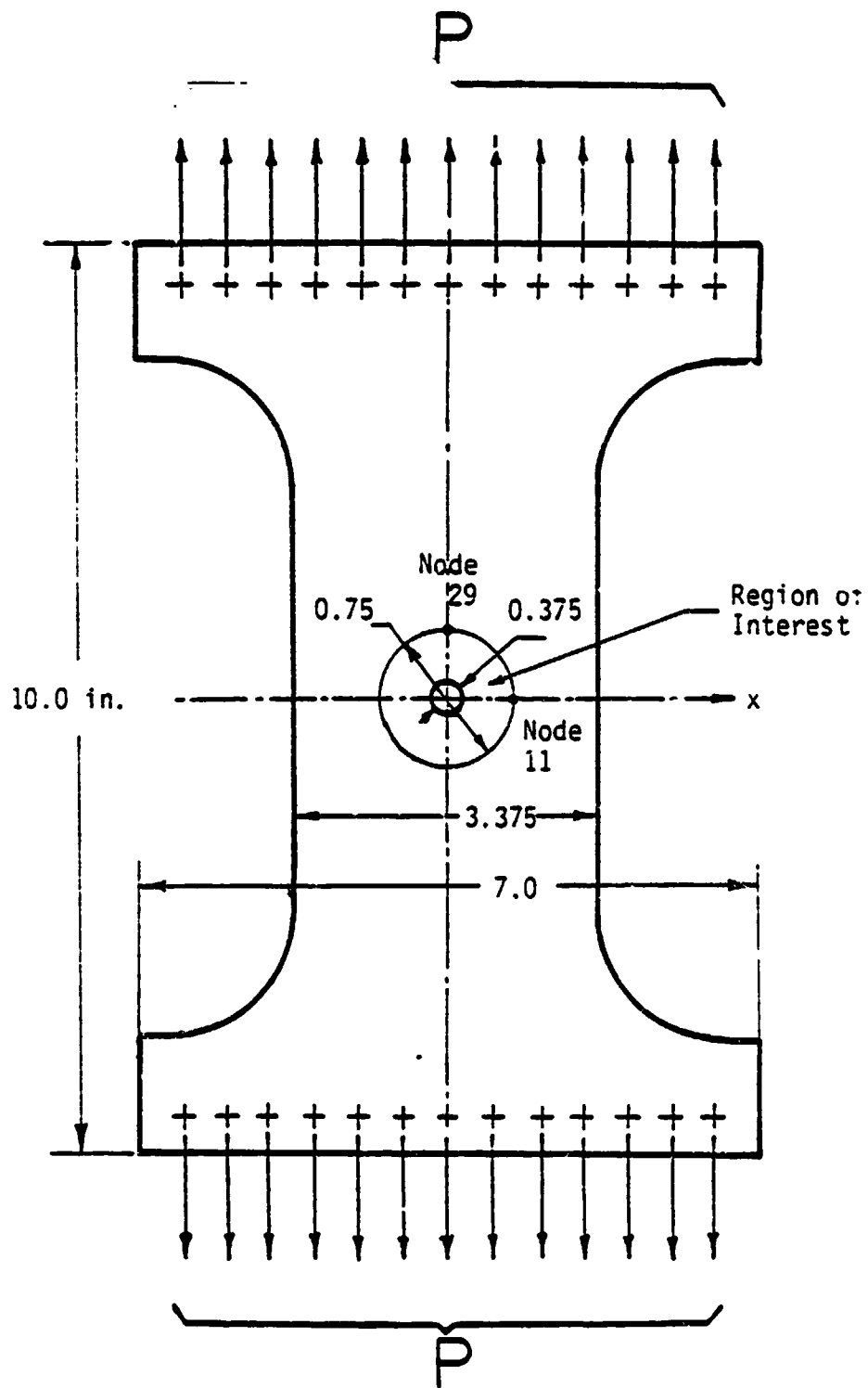


Figure 4-9. A Plate with a Hole under Axial Loading

TABLE 4-3. MEASURED DISPLACEMENTS ALONG
THE CIRCULAR CONTOUR OF THE
REGION OF INTEREST FOR EXAMPLE 3

| Node | u/u_{11} | v/v_{29} |
|------|------------|------------|
| 11 | 1.000 | 0.000 |
| 12 | 0.992 | 0.075 |
| 13 | 0.975 | 0.150 |
| 14 | 0.941 | 0.224 |
| 15 | 0.899 | 0.299 |
| 16 | 0.846 | 0.373 |
| 17 | 0.787 | 0.446 |
| 18 | 0.719 | 0.518 |
| 19 | 0.652 | 0.589 |
| 20 | 0.579 | 0.656 |
| 21 | 0.506 | 0.720 |
| 22 | 0.433 | 0.781 |
| 23 | 0.362 | 0.834 |
| 24 | 0.298 | 0.882 |
| 25 | 0.233 | 0.924 |
| 26 | 0.171 | 0.956 |
| 27 | 0.112 | 0.980 |
| 28 | 0.056 | 0.994 |
| 29 | 0.000 | 1.000 |

Measured values of $u_{11} = -14.2 \times 10^{-5}$ inches

and

$v_{29} = 35.7 \times 10^{-5}$ inches

V. RESULTS AND DISCUSSION

5.1 The Coupling of the BIE and Laser Speckle Techniques

Experimental displacement measurements coupled with the BIE method represent a useful solution procedure which extends the capabilities of coherent optics measurements in calculation of stresses or strains in engineering problems. Data analysis in speckle interferometry yields a map of surface displacements along the contour of a region of interest. These experimental values are used as data input to numerically calculate, with a high degree of resolution, strains and stresses at any desired location inside the region of interest through the BIE method.

In order to demonstrate the coupling of the two solution techniques as applies to linear elasticity problems, several examples are presented in the following sections. The numerical results are obtained through the use of a BIE computer program based on linear functional variations along the boundary segments. Displacement data input to the computer program are the experimental values of the example problems discussed previously in Chapter IV.

5.2 The Cantilever Beam Problem

The cantilever beam problem was analyzed using the BIE model for the region of interest shown in Figure 5-1. Sixty straight line segments of equal length were used. Nodal points 1-21 are specified to be traction free, points 21-31 were measured displacements which are zero. Points 31-51 are traction free and points 51-1 are measured displacements utilizing the laser speckle

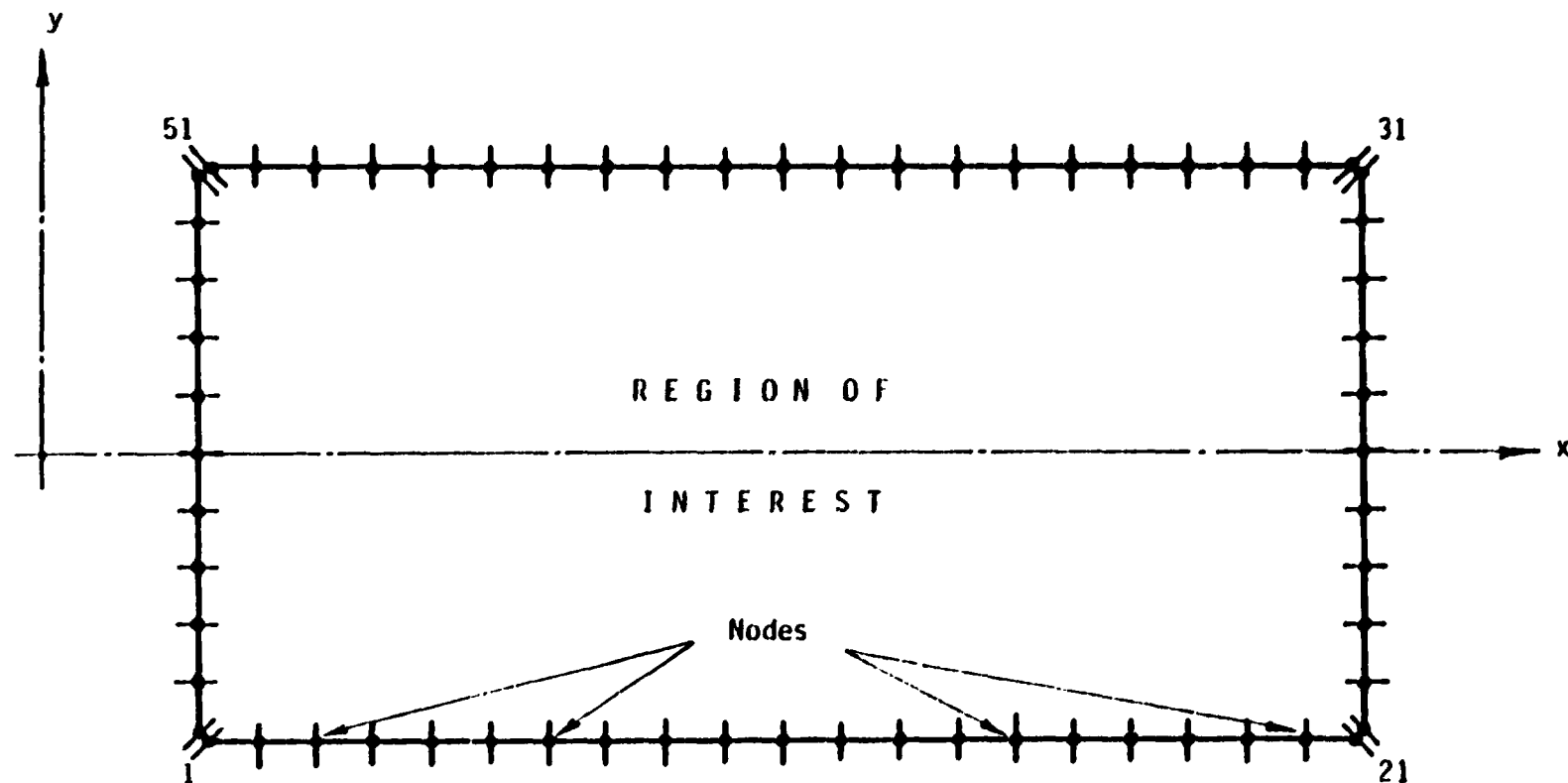


Figure 5-1. BIE Model for the Region of Interest of the Cantilever Beam Problem

technique of pointwise filtering. These measured values were listed previously in Table 4-1. Especial attention was given in the numerical procedure to the traction discontinuities at the corner points as discussed previously in Chapter III.

Table 5-1 is a display of the calculated BIE results for the stress components at sections $x=3.0$ and 5.0 inches. The results at section $x=3$ inches were compared to the stress function solution and to the bending moment for a load $W_y = 1.14$ lbf. Integration of the stress components over this section yielded a bending moment deviation of -0.58% . The same results were compared at the fixed end ($x=5$ inches). At this section the bending moment and shear force deviated from the static values by 6.49% and 7.6% respectively. As anticipated, the stress distribution at the fixed end section is different from the stress function solution. Since exact boundary conditions were specified for the BIE solution, it is logical to theorize that the results obtained from the combined laser speckle displacement measurements and BIE solution for this problem are more reliable than the stress function solution.

Internal displacements at three points along the neutral axis of the beam were also computed and compared to the measured values. The comparison is shown in Table 5-2.

The results of the combined laser speckle displacement measurements and BIE solution procedure compared favorably with the theoretical and the experimental results and static equivalent check. These results are particularly good in view of the small

TABLE 5-1. RESULTS OF THE BIE CALCULATIONS
FOR THE CANTILEVER BEAM PROBLEM

| y (inches) | σ_x (psi) at x=3.0 inches | | σ_x (psi) at x=5.0 inches | | τ_{xy} (psi) at x = 5.0 in. |
|---------------|-------------------------------------|-------------|-------------------------------------|-------------|--|
| | BIE | Theoretical | BIE | Theoretical | |
| 0.45 | 76.04 | 73.87 | 127.03 | 123.12 | 14.61 |
| 0.35 | 57.75 | 57.46 | 83.31 | 85.76 | 15.15 |
| 0.25 | 41.34 | 41.04 | 57.80 | 68.40 | -0.39 |
| 0.15 | 24.60 | 24.62 | 34.48 | 41.04 | -3.27 |
| 0.05 | 8.09 | 8.21 | 11.44 | 13.68 | -5.04 |
| -0.05 | -8.09 | -8.21 | -11.44 | -13.68 | -5.04 |
| -0.15 | -24.60 | -24.62 | -34.48 | -41.01 | -3.27 |
| -0.25 | -41.34 | -41.04 | -57.80 | -68.40 | -0.39 |
| -0.35 | -57.75 | -57.46 | -83.31 | -85.76 | 15.15 |
| -0.45 | -76.04 | -73.87 | -127.03 | -123.12 | 14.61 |

applied transverse load W_y .

Table 5-2. COMPARISON BETWEEN CALCULATED AND MEASURED VALUES OF THE BEAM DEFLECTION ALONG THE X-AXIS

| x (inches) | $v \times 10^4$ (inches) | |
|---------------|--------------------------|----------|
| | BIE | Measured |
| 3.2 | -8.57 | -8.47 |
| 3.4 | -6.89 | -6.69 |
| 3.6 | -5.37 | -5.33 |

The ability to partition a section of a geometry has an additional advantage in experimental data displacement measurements. For example, in this sample problem, the free end load was governed by the displacement measurements of the free end. The ability to partition the geometry will allow displacements within ~~regions to exceed the measurable data~~ if only information is obtained in regions of high stress gradients.

5.3 The Circular Disk Problem

This problem was studied using the BIE model illustrated in Figure 5-2. The boundary of the region of interest is represented by thirty straight line segments. Due to the symmetric nature of the problem, boundary conditions for nodal points 1-11 are specified as zero traction in the x-direction and zero displacement in the y-direction. Furthermore, nodal points 26-1 are specified as traction free in the y-direction and zero displacement in the x-direction. Points 11-17 are traction free and points 17-26 are specified displacements. Displacement input data for the BiE solution were obtained from the best curve fit of the experimental data previously shown in Figure 4-8.

The numerical results for the normalized stress distribution along the horizontal diameter of the disk were compared to the theoretical results of Reference [38]. The comparison is very good as depicted in Table 5-3. Also, the results of the calculated displacements along the horizontal and vertical diameters compare favorably with the experimental results as shown in Figures 5-3 and 5-4 respectively.

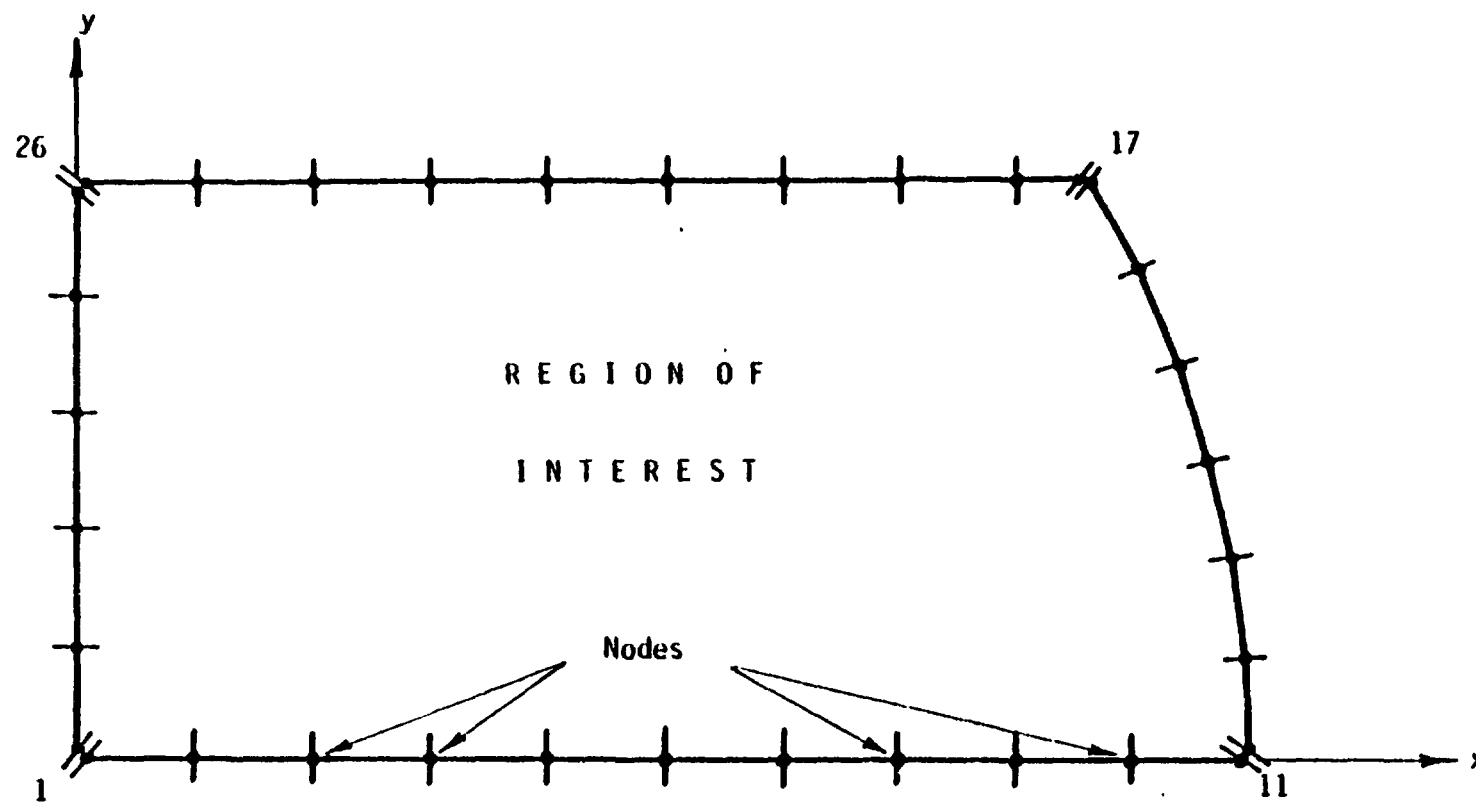


Figure 5-2. BIE Model for the Region of Interest of the Circular Disk Problem

TABLE 5-3. COMPARISON OF THE BIE CALCULATIONS AND THEORETICAL SOLUTION ALONG THE HORIZONTAL DIAMETER FOR THE CIRCULAR DISK PROBLEM

| Dimensionless Distance $\frac{x}{d/2}$ | Dimensionless Stress $\frac{\sigma_y}{P/d}$ | |
|---|---|-------------|
| | BIE | Theoretical |
| 0.0 | -1.941 | -1.911 |
| 0.1 | -1.890 | -1.860 |
| 0.2 | -1.743 | -1.719 |
| 0.3 | -1.524 | -1.506 |
| 0.4 | -1.266 | -1.257 |
| 0.5 | -0.996 | -0.993 |
| 0.6 | -0.738 | -0.740 |
| 0.7 | -0.501 | -0.510 |
| 0.8 | -0.299 | -0.309 |
| 0.9 | -0.126 | -0.141 |

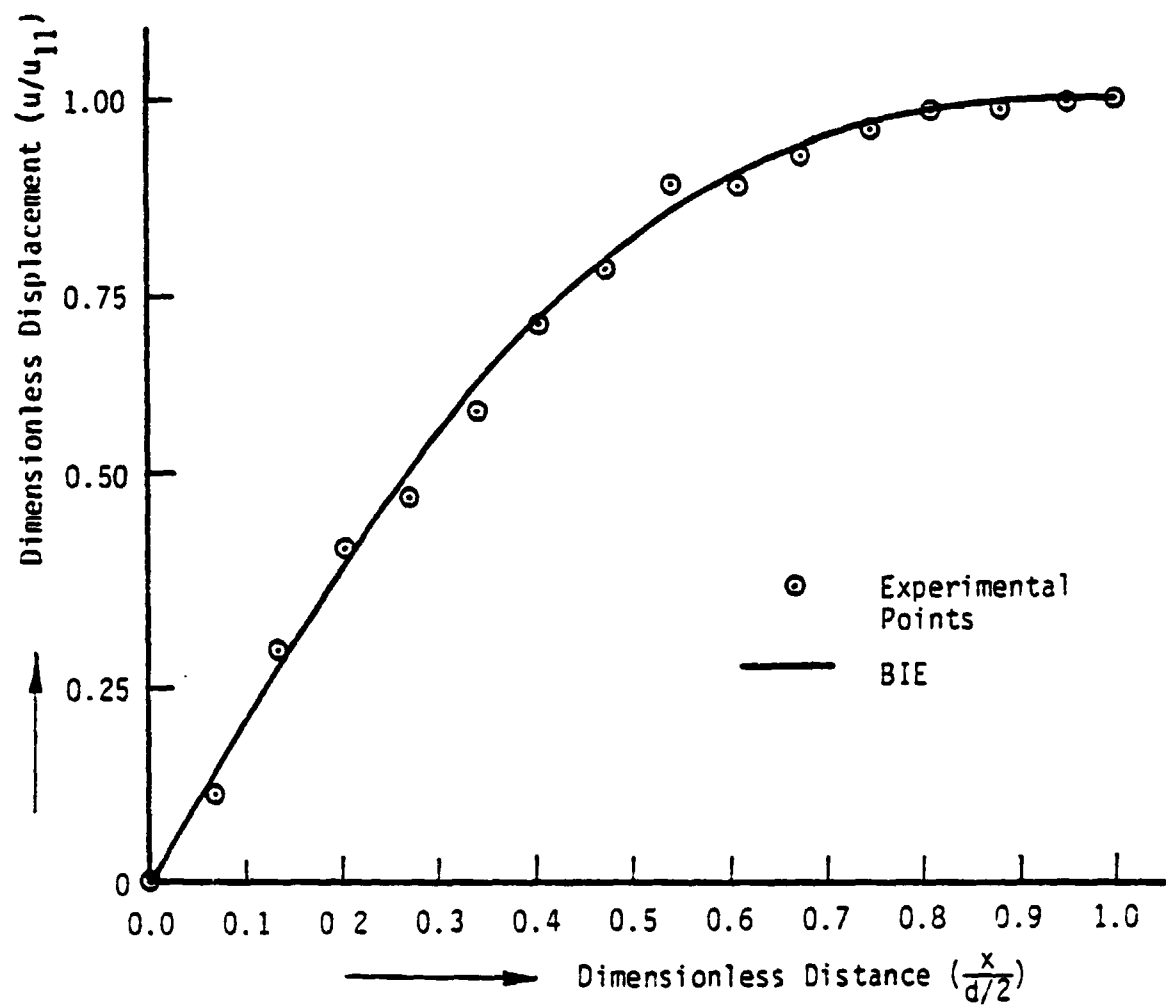


Figure 5-3. Horizontal Displacement Components
Along Line $y = 0$

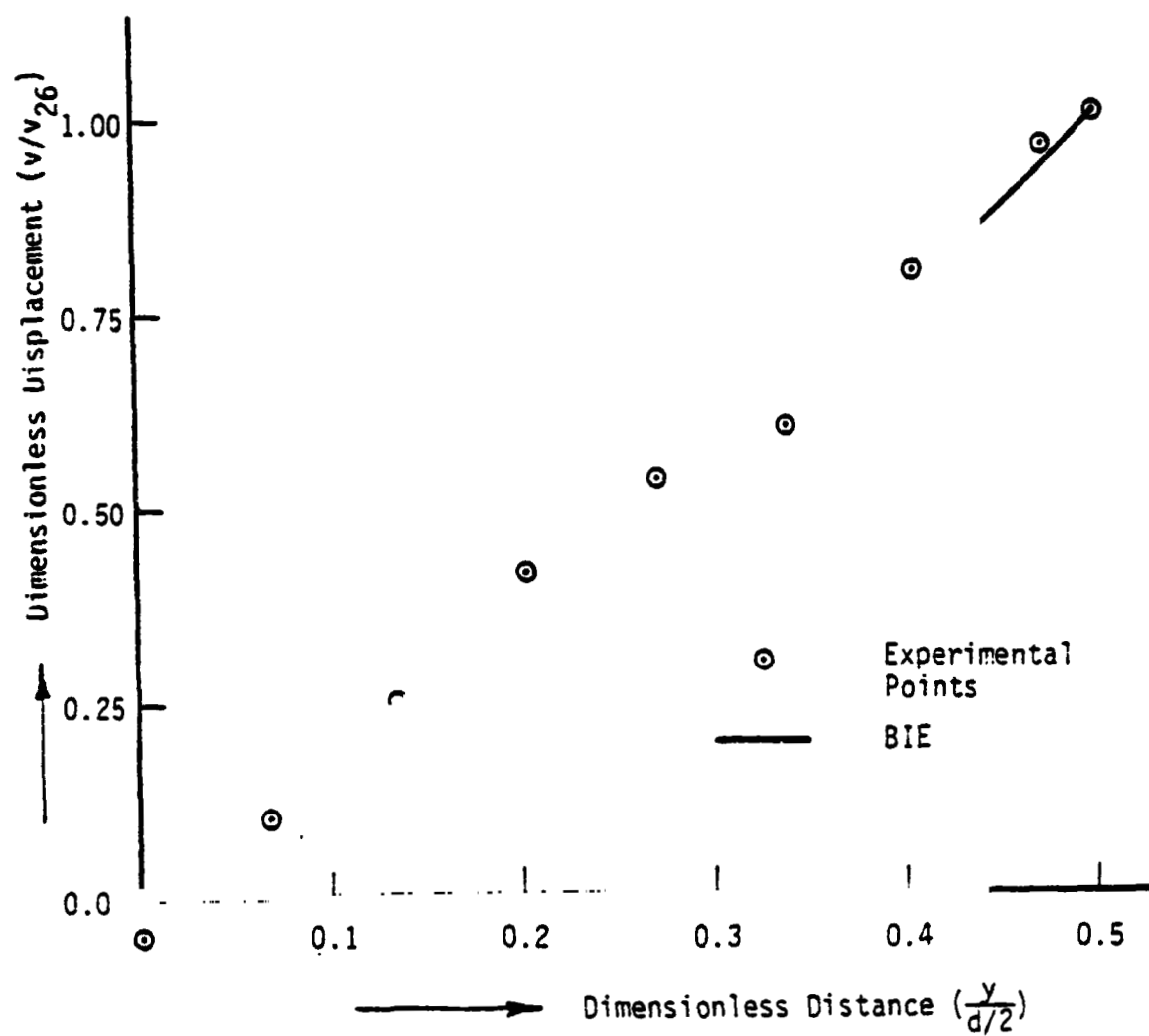


Figure 5-4. Vertical Displacement Components
Along Line $x = 0$

5.4 The Stress Concentration Problem

The example problem of the plate with a circular hole under uniform tension was selected to demonstrate the application of the coupled technique of laser speckle interferometry and BIE to solve a typical stress concentration problem.

Figure 5-5 illustrates the BIE idealization for the symmetric portion of the region of interest used for the stress analysis of the problem. Twenty-seven straight line segments with twenty-nine nodes were used. Nodes 1-10, along the hole surface, are specified to be traction free. Displacement components of nodes 11-29 are measured values as listed previously in Table 4-3.

Internal stresses were computed at a series of points along the x-axis. The numerical results, normalized by the resultant applied load divided by the net cross-sectional area, were compared to the available closed form solution for a similar problem of an infinite plate [39] as shown in Table 5-4. It is of most interest to notice that the stress values predicted by the numerical solution are larger than the corresponding values predicted by the closed form solution. However, this is expected since the numerical results are for a plate with finite width. The boundary stress at node 10 was also calculated and the computed elastic stress concentration factor, maximum calculated stress divided by the nominal stress, σ_{NOM} , was 2.66 as compared to 2.67 given in Reference [39] for the plate with finite width.

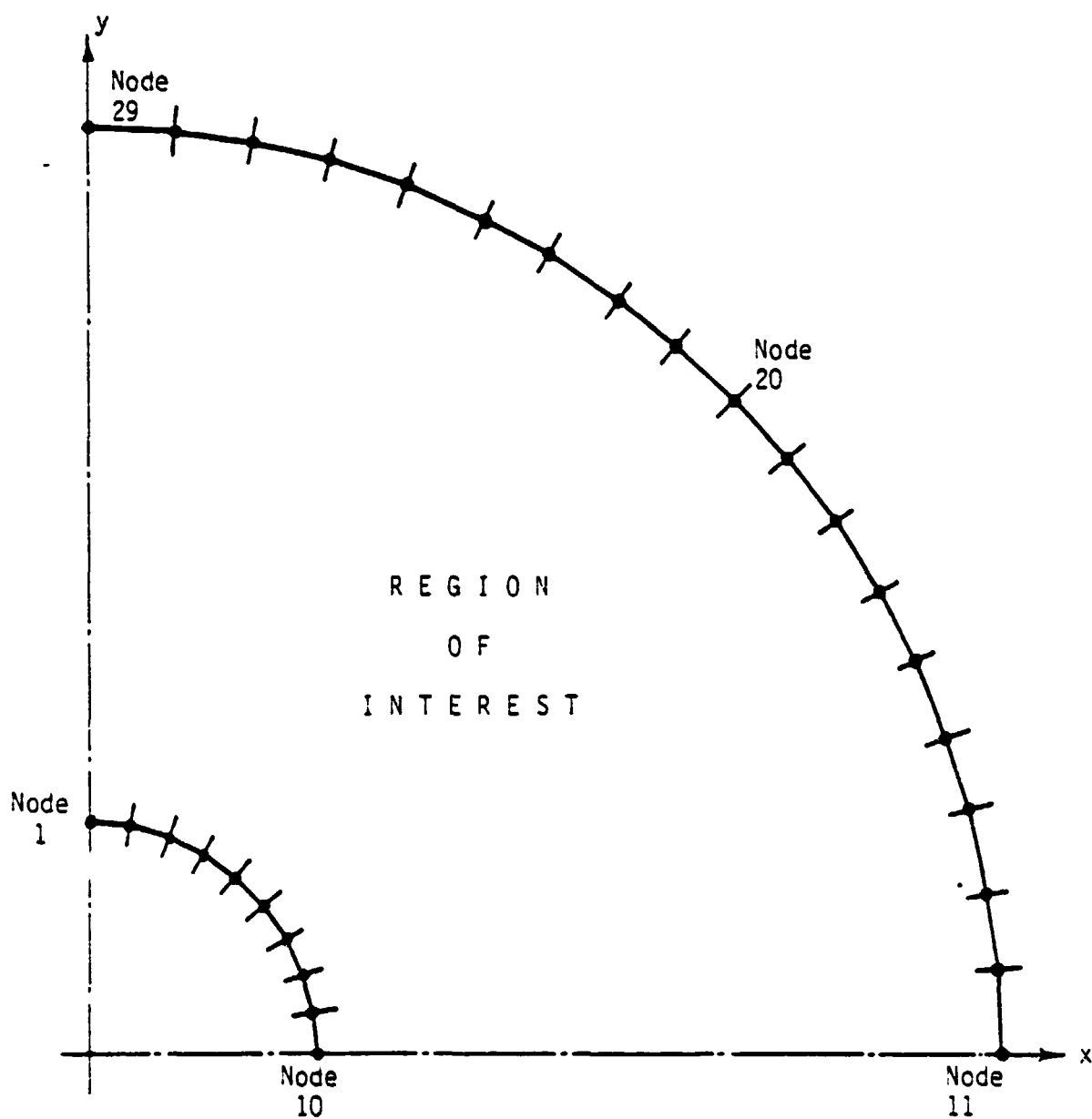


Figure 5-5. Twenty-Seven Segment BIE Model
Used for the Stress Concentration
Problem

TABLE 5-4. COMPARISON OF THE BIE CALCULATIONS AND THEORETICAL SOLUTION ALONG THE X-AXIS FOR THE STRESS CONCENTRATION PROBLEM

| Dimensionless Distance $\frac{x-R}{R}$ | Stress Concentration σ_y/σ_{NOM} | |
|---|--|-------------|
| | BIE | Theoretical |
| 0.02 | 2.63 | 2.55 |
| 0.03 | 2.55 | 2.49 |
| 0.04 | 2.49 | 2.44 |
| 0.05 | 2.43 | 2.39 |
| 0.08 | 2.23 | 2.25 |
| 0.10 | 2.20 | 2.17 |
| 0.20 | 1.87 | 1.84 |
| 0.40 | 1.49 | 1.46 |
| 0.60 | 1.29 | 1.27 |
| 0.80 | 1.17 | 1.15 |
| 1.00 | 1.10 | 1.08 |
| 1.50 | 1.01 | 0.99 |

R is the radius of the hole
Nominal Stress $\sigma_{NOM} = 204.8$ psi

VI. CONCLUSIONS

The general theory for laser speckle shearing interferometry which includes both the contributions of in-plane and out of plane deformations was developed. Laser speckle interferometry provides a technique to directly measure in-plane displacement components without the need for vibration isolation. This experimental technique was coupled with a numerical boundary-integral solution technique to calculate stresses and strains at any point for a deformed solid utilizing the measured boundary displacement data.

The analytical formulation of the boundary-integral equation method for two and three dimensional elasticity was reviewed in detail. The linear boundary element scheme used in the numerical formulation for plane problems is simple and offers a great flexibility and ease in solving many important solid mechanics problems.

The numerical results of the sample problems presented illustrate the successful coupling of laser speckle interferometry and boundary-integral equation techniques as applied to elasticity problems. High accuracy was attainable by using a relatively coarse level of boundary discretization. The ability to partition a section of a geometry has an additional advantage in experimental displacement measurements. It may allow displacements within regions rather than the particular region of interest to exceed the measurable data. The coupling of laser speckle interferometry and the numerical boundary-integral technique becomes more compatible

when the displacement data can be stored in the computer directly without the need of time consuming data analysis. The coupled technique may be applied to axially symmetric and fracture mechanics problems. In particular, fracture mechanics applications appear to be a well posed problem using this coupled technique. A closed contour surrounding the crack will form the measured boundary displacements and the boundary-integral solution technique used to calculate internal values. Thus the fracture mechanics problems form the basis for future research work.

LIST OF REFERENCES

1. Ranson, W.F., "Use of Holographic Interferometry to Determine the Surface Displacement Components of a Deformed Body," Ph.D. Thesis, Dept. of Theoretical and Applied Mechanics, University of Illinois, Urbana, Ill., 1971.
2. Holloway, D.C., Ranson, W.F. and Taylor, C.E., "A Neoteric Interferometry for Use in Holographic Photoelasticity," *Experimental Mechanics*, Vol. 11, No. 10, 1972.
3. Erf, R.K., Ed., "Holographic Nondestructive Testing," Academic, New York (1974).
4. Erf, R.K., Ed., "Speckle Metrology," Academic, New York (1978).
5. Schaeffel, J.A., Ranson, W.F., Mullinax, B.R. and Swinson, W.F., "Computer Aided Optical Nondestructive Detection System for Composite Materials," U.S. Army Missile Research and Development Command T.R., T-78-5, 1977.
6. Burch, J.M. and Tokarski, J.M.J., "Production of Multiple Beam Fringes from Photographic Scatterers," *Optica Acta*, Vol. 15, pp. 101-111, 1968.
7. Hung, Y.Y., Rowlands, R.E. and Daniel, I.M., "Speckle-Shearing Interferometric Technique: A Full-Field Strain Gauge," *Appl. Optics*, 14(3), pp. 618-622, 1975.
8. Hung, Y.Y. and Liang, C.Y., "Image-Shearing Camera for Direct Measurement of Surface Strains," *Applied Optics*, 18(7), pp. 1046-1051, 1979.
9. Kellogg, O.D., "Foundations of Potential Theory," Dover, New York (1929).
10. Jaswon, M.A., "Integral Equation Methods in Potential Theory I," *Proc. Roy. Soc.*, Vol. 275A, pp. 23-32, 1963.
11. Symm, G.T., "Integral Equation Methods in Potential Theory II," *Proc. Roy. Soc.*, Vol. 275A, pp. 33-46, 1963.
12. Rizzo, F.J., "An Integral Equation Approach to Boundary Value Problems of Classical Elastostatics," *Q. Appl. Math.*, Vol. XXV, No. 1, pp. 83-95, 1967.
13. Cruse, T.A., "Numerical Solutions in Three Dimensional Elastostatics," *Int. J. Solids Struct.*, 5, pp. 1259-1274, 1969.

14. Cruse, T.A., "Application of the Boundary-Integral Method to Three Dimensional Stress Analysis," *Computers & Structures*, 3, pp. 509-527, 1973.
15. Cruse, T.A., "An Improved Boundary-Integral Method for Three Dimensional Elastic Stress Analysis," *Computers & Structures*, 4, pp. 741-754, 1974.
16. Cruse, T.A. and Rizzo, F.J., "A Direct Formulation and Numerical Solution of the General Transient Elastodynamic Problem I," *J. of Math. Analysis and Appl.*, 22, pp. 244-259, 1968.
17. Cruse, T.A., "A Direct Formulation and Numerical Solution of the General Transient Elastodynamic Problem II," *J. of Math. Analysis and Appl.*, 22, pp. 341-355, 1968.
18. Rizzo, F.J. and Shippy, D.J., "A Formulation and Solution Procedure for the General Non-Homogeneous Elastic Inclusion Problem," *Int. J. Solids Struct.*, 4, pp. 1161-1179, 1968.
19. Swedlow, J.L. and Cruse, T.A., "Formulation of Boundary Integral Equations for Three-Dimensional Elasto-Plastic Flow," *Int. J. Solids Struct.*, 7, pp. 1673-1683, 1971.
20. Mendelson, A., "Boundary-Integral Methods in Elasticity and Plasticity," NASA TN D-7418, 1973.
21. Cruse, T.A. and Van Buren, W., "Three-Dimensional Elastic Stress Analysis of a Fracture Specimen with An Edge Crack," *Int. J. of Fracture Mechanics*, Vol. 7, No. 1, pp. 1-15, 1971.
22. Cruse, T.A. and Wilson, R.B., "Advanced Applications of Boundary-Integral Equation Methods," *Nuc. Engng and Design*, 46, pp. 223-234, 1978.
23. Rizzo, F.J. and Shippy, D.J., "An Advanced Boundary-Integral Equation Method for Three-Dimensional Thermoelasticity," *Int. J. for Num. Meth. in Engng*, 11, pp. 1753-1768, 1977.
24. Rizzo, F.J. and Shippy, D.J., "A Method for Stress Determination in Plane Anisotropic Elastic Bodies," *J. Composite Materials*, 4, pp. 36-61, 1970.
25. Mukherjee, S. and Kumar, V., "Numerical Analysis of Time-Dependent Inelastic Deformation in Metallic Media Using the Boundary-Integral Equation Method," *J. of Appl. Mech.*, 45, pp. 785-790, 1978.

26. Cruse, T.A., Snow, D.W. and Wilson, R.B., "Numerical Solutions in Axisymmetric Elasticity," *Comput. & Struct.*, 7, pp. 445-451, 1977.
27. Stern, M., "A General Boundary Integral Formulation for the Numerical Solution of Plate Bending Problems," *Int. J. Solids Struct.*, 15, pp. 769-782, 1979.
28. Hadid, H.A. and Tottenham, H., "Variational and Integral Methods for the Analysis of Hyper Shell," *Proc. of an Int. Conf. on Variational Methods in Engng*, Southampton Univ., England, pp. 9/76-9/88, 1972.
29. Zienkiewicz, O.C., Kelly, D.W. and Bettles, P., "The Coupling of the Finite Element Method and Boundary Solution Procedures," *Int. J. for Num. Meth. in Engng*, 11, pp. 355-375, 1977.
30. Cruse, T.A. and Rizzo, F.J. (Ed.), "Boundary-Integral Equation Method: Computational Applications in Applied Mechanics," *ASME Proc. AMD-Vol. 11* (1975).
31. Love, A.E.H., "A Treatise on the Mathematical Theory of Elasticity," 4th ed., Dover, New York (1944).
32. Cruse, T.A., "Mathematical Foundations of the Boundary-Integral Equation Method in Solid Mechanics," *AFOSR-TR-77-1002*, 1977.
33. Brebbia, C.A., "The Boundary Element Method for Engineers," John Wiley, New York (1978).
34. Lachat, J.C. and Watson, J.O., "Effective Numerical Treatment of Boundary Integral Equations: A Formulation for Three-Dimensional Elastostatics," *Int. J. for Num. Meth. in Engng*, 10, pp. 991-1005, 1976.
35. Stippes, M. and Rizzo, F.J., "A Note on the Body Force Integral of Classical Elastostatics," *ZAMP*, 28, pp. 339-341, 1977.
36. Lachat, J.C., "A Further Development of the Boundary Integral Technique for Elastostatics," *Dissertation, Univ. of Southampton, England*, 1975.
37. Riccardella, P.C., "An Implementation of the Boundary-Integral Technique for Planar Problems in Elasticity and Elasto-Plasticity," *Report SM-73-10, Mech. Engng Dept., Carnegie-Mellon Univ., Pittsburgh, Pa.*, 1973.

38. Timoshenko, S.P. and Goodier, J.N., "Theory of Elasticity," Third Edition, McGraw-Hill (1970).
39. Peterson, R.E., "Stress Concentration Factors, Charts and Relations Useful in Making Strength Calculations for Machine Parts and Structural Elements," John Wiley, New York (1974).